A QUASI–GEOSTROPHIC CIRCULATION MODEL OF THE NORTHEAST PACIFIC OCEAN

by

PATRICK F. CUMMINS

B.Eng., Concordia University, 1980

M.Sc., University of British Columbia, 1983

A THESIS SUBMITTED IN PARTIAL FULFILMENT OF

THE REQUIREMENTS FOR THE DEGREE OF

DOCTOR OF PHILOSOPHY

in

THE FACULTY OF GRADUATE STUDIES

Department of Oceanography

We accept this thesis as conforming

to the required standard

THE UNIVERSITY OF BRITISH COLUMBIA

August 1989

67

Department of Oceanography

The University of British Columbia

2075 Wesbrook Mall

Vancouver, Canada

Date: August 30, 1989

Abstract

A limited–area quasi–geostrophic numerical model with mesoscale resolution is developed to study the circulation in the Northeast Pacific Ocean. The model domain extends from the British Columbia/Alaska coast out to 170°W and down to 45°N, and incorporates the coastline geometry and bottom topography of the region.

In a benchmark experiment, the circulation is driven with a steady, climatological wind stress curl field. Statistical properties of the solution are determined from a long–term integration and compared with observations from the Gulf of Alaska. The cyclonic circulation of the model basin contains the analogue of a meandering Alaska Current. At the head of the Gulf, this current flows into an intense boundary current corresponding to the Alaskan Stream. Within the model Alaska Current, anticyclonic closed streamline features are occasionally generated which are representative of the Sitka Eddy. In the upstream region, the model Alaskan Stream displays large amplitude aperiodic meanders, while, in the downstream region, the boundary current separates and is subject to smaller amplitude lateral meandering due to topographic waves. The occurrence of perturbations with similar characteristics in the Alaskan Stream has recently been verified in satellite AVHRR imagery.

The model is also used to examine the effects of bottom topography and seasonal wind forcing on the circulation of the subpolar gyre. The characteristics of the Alaskan Stream are shown to depend crucially on the presence of the Aleutian Trench. In an experiment with a flat bottom and steady forcing, the most energetic signal is due to mesoscale eddies with a 100 day period associated with barotropic wave propagation along the Aleutian arc. Bottom topography eliminates this signal by inhibiting the nonlinear transfer of energy between the first baroclinic and the barotropic mode, thereby stabilizing the model Alaskan Stream to baroclinic instability. Experiments with a climatological seasonal cycle in the wind field show that

the bottom topography has an important influence in moderating the intensity of the seasonal response. This result is used to explain the discrepancy between observations of seasonal variability in the volume transport of the Alaskan Gyre and the transport obtained in previous numerical modelling studies.

Table of Contents

List of Tables

List of Figures

Acknowledgements

I am grateful to my supervisor, Dr. L.A. Mysak, for his support and encouragement throughout the course of this work. I also thank the members of my supervisory committee, Drs. A.F. Bennett, G. Holloway, W. Hsieh, and S. Pond, for their helpful comments and criticisms. Dr. W.R. Holland of NCAR provided several stimulating discussions on quasi–geostrophic numerical modelling. Dr. T. Royer of the University of Alaska supplied the satellite image of the Alaskan Stream. The text was carefully proofread by Diane Masson. Andrew Weaver and Rodolfo Bermejo–Bermejo generously provided me with the use of their apartments in Vancouver.

The research for this thesis was supported, in part, by NSERC Operating and Strategic grants awarded to Drs. L.A. Mysak and W. Hsieh, and by a U.S. Office of Naval Research grant awarded to Dr. L.A. Mysak.

This thesis is dedicated to the memory of my parents.

1. Introduction

The circulation of the Northeast (NE) Pacific Ocean has been the subject of intensive research in recent years, with much of this effort has focussed on the California Current System. The Alaskan Gyre, which is one of the most salient features of this ocean basin, has received less attention. As a consequence, the present state of knowledge concerning this gyre is fairly rudimentary. It has become clear, however, that there are several potential benefits to be derived from the study of this oceanic region. For example, a knowledge of the circulation is essential in predicting the dispersal of anthropogenic pollutants, such as the crude oil released in the massive oilspill of March 24, 1989, in Prince William Sound, Alaska. The NE Pacific circulation may also be significant to fisheries activities. The Gulf of Alaska is a major habitat for many species of commercially harvested fish (e.g., pink and sockeye salmon) and evidence is accruing that variability of oceanic conditions may be an important factor in the year–to year changes in stock recruitment and return migration routes of these fish (Hamilton 1985; Hamilton and Mysak 1986; Mysak 1986). The NE Pacific circulation may also be important from a global perspective. For example, in the effort to understand global climate change, it has been suggested that low frequency variability in the NE Pacific may be linked to ENSO (El Niño–Southern Oscillation) events in the tropical Pacific (Emery and Hamilton 1985, Mysak 1986). Thus a greater understanding of the Alaskan Gyre could contribute to unravelling the energy pathways of global climatic events.

The oceanic data that have been collected from the Gulf of Alaska are still relatively sparsely spaced, both in space and in time. Previous observational programs in the Gulf have revealed some of the fundamental characteristics of the flow field (e.g., Warren and Owens 1988; Royer and Emery 1987; Reed 1984). The goal of these studies was to determine mean baroclinic transports, the water property distributions and particle velocities. Other research has examined the variability associated with the mesoscale eddy field (Tabata 1982) and the seasonal cycle (Royer 1981).

There have been only a few theoretical or numerical studies to synthesize these measurements and to provide a dynamical framework for their interpretation. This thesis is an attempt to ameliorate this situation by studying, for the first time, the circulation of the Gulf of Alaska through the use of an eddy–resolving quasi–geostrophic numerical model. The most fundamental problem addressed here is to determine to which extent the model is able to simulate the flow statistics of the region. In a benchmark experiment the mean flow and its variability are compared to the available observations to establish whether the model is able to reproduce at least the gross features of the flow field. The numerical solution should then provide a basis for the interpretation of the existing observational data and possibly act as a guide for future field experiments. In addition, the model is also used to examine the flow dynamics and the influence of specific environmental parameters on the circulation. Of special interest is the determination of the role of bottom topography in the maintainance of the vertical structure of the mean flow and in the horizontal structure of the western boundary current. The importance of seasonal forcing is also assessed.

Previous numerical models of this region have, for the most part, been restricted to coarse resolution with primitive equation physics. Hsieh (1987) used the primitive equation Bryan–Cox model with $1° \times 1°$ resolution to examine the response of the ocean to seasonal variations in the wind stress and surface heat flux. The NE Pacific was also included as a subregion in the North Pacific circulation model of Huang (1978, 1979). However, the resolution of his model ($2.5° \times 2.5°$) was insufficient to resolve the Alaskan Gyre. In fact, the Aleutian Island Chain, a lateral boundary of importance in establishing the gyre, is absent in his model.

A major deficiency of these numerical modelling efforts is that the solutions obtained are dominated by lateral viscosity. A large value of the eddy viscosity is required because of the relative coarseness of the grid resolution, leading to solutions that are unrealistic in several respects (e.g., the width of the western boundary current is far too large). In contrast to this, the fine resolution of the model developed here allows the use of a comparatively low value for the eddy viscosity coefficient. As a consequence, spontaneous transient motions arise from instabilities of mean currents. The structure of the solution obtained is generally much more realistic than those of the coarse resolution studies.

The experimental results presented here will also complement and extend the previous analytical studies. Thomson (1972) developed a linear frictional model of the Alaskan Stream and considered the vorticity balances along the westward path of the current. Mysak (1982) applied a barotropic instability model of flow along a trench to explain wavelike fluctuations in the Alaskan Stream off Kodiak Island. The present model allows a calculation of more realistic vorticity balances for a model Alaskan Stream when bottom topography and nonlinearity are included. The model solution also displays the propagation of topographic waves along the Aleutian trench and thus invites comparison with Mysak's analysis. The appearance of mesoscale eddies, such as the Sitka Eddy, in the Alaska Current has been analytically modelled by Willmott and Mysak (1980) who proposed that this eddy is generated by multiply–reflected planetary waves driven by interannual wind stress fluctuations. Although this hypothesis will not be directly tested with the numerical model, the results suggest other possible mechanisms for the generation of eddies in the Alaska Current.

The numerical model used in this study is a limited–area, eddy–resolving, quasi–geostrophic one and it may be considered to be an extension of Holland's (1978) two–layer, rectangular basin ocean model. The most significant changes over Holland's model are an irregular coastline geometry and an arbitrary number of vertical layers. Two important idealizations are included in the present model. The first involves the assumption of quasi–geostrophy. This implies the use of a set of equations which retain only a simplified physics with respect to the more complete primitive equations. The second idealization concerns the treatment of the Alaskan Gyre as an isolated system. The model domain has artificial closed boundaries to the south and west so that the interaction of the Alaskan Gyre with the surrounding ocean is ignored. The advantages and limitations of this approach are discussed at greater length below.

Numerical modelling necessarily involves making choices and compromises based on the types of physical processes one wishes to include, the resolution required in both the horizontal and vertical directions, the size of the ocean domain under consideration and the length of the integration time. In most cases, the primary limiting factor is the computational requirements for core memory and CPU time. For the modelling of mesoscale variability in an ocean gyre one requires fine horizontal resolution, with a grid interval no larger than about 25 km, and moderate vertical resolution (a few layers are usually sufficient). In addition, long integration times of the order of ten years or more are needed to compute equilibrium statistics. These are substantial computational demands and hence, rather than to integrate a full primitive equation (PE) model, a quasi-geostrophic framework is adopted. The principal advantages offered by the QG models are a greater computational efficiency and a more easily interpreted model response. These advantages are obtained at the expense of excluding certain processes and retaining only a simplified physics (compared to PE models). In particular, QG models are based on the assumptions of small Rossby number, small interfacial displacements and topographic relief and a constant static stability. This effectively excludes high frequency motions such as inertio–gravity waves along with long time scale thermohaline processes. Despite these limitations, there are, nevertheless, good reasons to be confident that such models can reasonably simulate the wind–driven circulation. For the Gulf Stream and Kuroshio Extension regions, Schmitz and Holland (1982, 1986) have shown that a

QG model is capable of accurately simulating the spatial distribution of second–order statistical properties of the flow field. In addition, the series of QG limited–area calculations reported by Holland (1986) apparently reproduce the major features of the large–scale circulation in a variety of geographic locations. The NE Pacific may well be particularly well suited to the application of a QG model, since it is known that the thermohaline and convective processes, which are known to lead to meridional overturning motions in certain regions of the world ocean (e.g., the North Atlantic), are not active in this region (Warren, 1983). Thus, it is anticipated that the essential physics of the wind–driven circulation of the NE Pacific are retained within the QG formulation.

In recent years there has been a rapid development of regional eddy–resolving ocean circulation models, and several of these have been very successful in obtaining realistic simulations of localized current systems (e.g. Hurlburt and Thompson 1985, Holland 1986). These models are constructed with artificial boundaries which do not correspond to true lateral boundaries of the ocean. Two approaches are commonly taken to handle these artificial boundaries. One is to allow open boundaries and thus specify an inflow/outflow of fluid into or out of the domain. Local forcing is usually not included in this approach. The other is to close the domain, thus allowing no flow across the boundaries, and to retain the local forcing. Special regions of enhanced friction are inserted near the artificial boundaries in order to isolate an interior region of interest within the model domain. This latter approach assumes that the oceanic region to be modelled may be considered in isolation from the surrounding regions. Some justification for treating the subpolar gyre in the NE Pacific in this way is found from the maps of potential vorticity on isopycnal surfaces, given by Talley (1988). She shows that, on upper ocean isopycnal surfaces, a very large mean gradient of potential vorticity exists between the subtropical and subpolar gyres of the North Pacific. Since fluid motion across mean potential vorticity contours is inhibited, the presence of the large gradient suggests that the two gyres systems are dynamically well separated.

The two approaches to regional modelling were considered for the NE Pacific, and both were attempted. The closed domain approach was the more successful one for two reasons: the inclusion of local forcing was found to be essential, and boundary conditions required for the inflow/outflow approach are too poorly known. The discussion in this thesis will be confined to results with a closed domain. An alternative approach involving nested grids, appropriate for the study of gyre–scale interannual variability, is suggested in the concluding section.

The following chapter presents a review of the circulation of the NE Pacific. This gives a description of the characteristics of the flow field which will be compared with the numerical solution. In chapter 3 the details of the numerical model are presented as well as a discussion of two diagnostic tools which are used to draw inferences on energy transfers and vorticity budgets from the numerical solution. Chapter 4 discusses the results from a benchmark experiment in which the model is configured with a realistic bottom topography and driven by the steady climatological winds. The solution is examined in detail and used to quantify several aspects of the flow in the Gulf of Alaska and to compare, when possible, with oceanic observations. In chapter 5 the solution to a similar experiment with flat–bottom topography is discussed. Comparison with the benchmark experiment demonstrates the importance of topography in determining the vertical structure of the flow field. The results of two experiments with seasonal wind forcing are discussed in chapter 6. It is shown that the bottom topography has an important role in moderating the amplitude of the seasonal response. Chapter 7 discusses briefly the results of additional miscellaneous experiments intended mainly to examine the sensitivity of the solution to details of the model. The thesis concludes with a discussion of possible future directions in modelling the circulation of the Gulf of Alaska.

2. Review of the Northeast Pacific Circulation

The hydrographic and current measurements obtained from the Gulf of Alaska have recently been reviewed by Schumacher and Reed (1983). The circulation pattern that emerges from these observations is represent schematically in Fig. 1. The broad and sluggish North Pacific Current (a.k.a. the West Wind Drift) bifurcates near 45°N, as it approaches the west coast of North America, into the southward flowing California Current and the northward flowing Alaska Current. The latter is also a slow-moving current, several hundred kilometers wide and forms the eastward branch of the large-scale, wind driven, cyclonic circulation in the Gulf of Alaska. Near 150°W the Alaska Current narrows and intensifies to form the Alaskan Stream, a high–speed, southwestward flowing boundary current. Some of the water transported by the Alaskan Stream continues westward to enter the Bering Sea, while a portion may return to the North Pacific Current. It is this counterclockwise circulation system which constitutes the Alaskan Gyre.

We now consider in greater detail some of the salient features of this gyre for which intercomparisons with the numerical model results will be attempted. In particular we examine some measurements obtained from the Alaskan Stream, from along Line P and from the region offshore of Sitka, Alaska (57°N, 136°W) where a recurrent anticyclonic eddy has been observed. Also included are brief discussions of the seasonal and interannual variability of the gyre circulation and of the atmospheric circulation over the Gulf. Various coastal currents, such as the Kenai Current, are omitted from this discussion. Their influence is largely confined to the continental shelf which is not resolved in the model.

2.1 Alaskan Stream

The most often observed current in this region is the Alaskan Stream. Numerous hydrographic sections have been obtained over the years (e.g. Favorite (1967), Reed et al. (1980), Reed (1984)), as well as a limited number of current meter

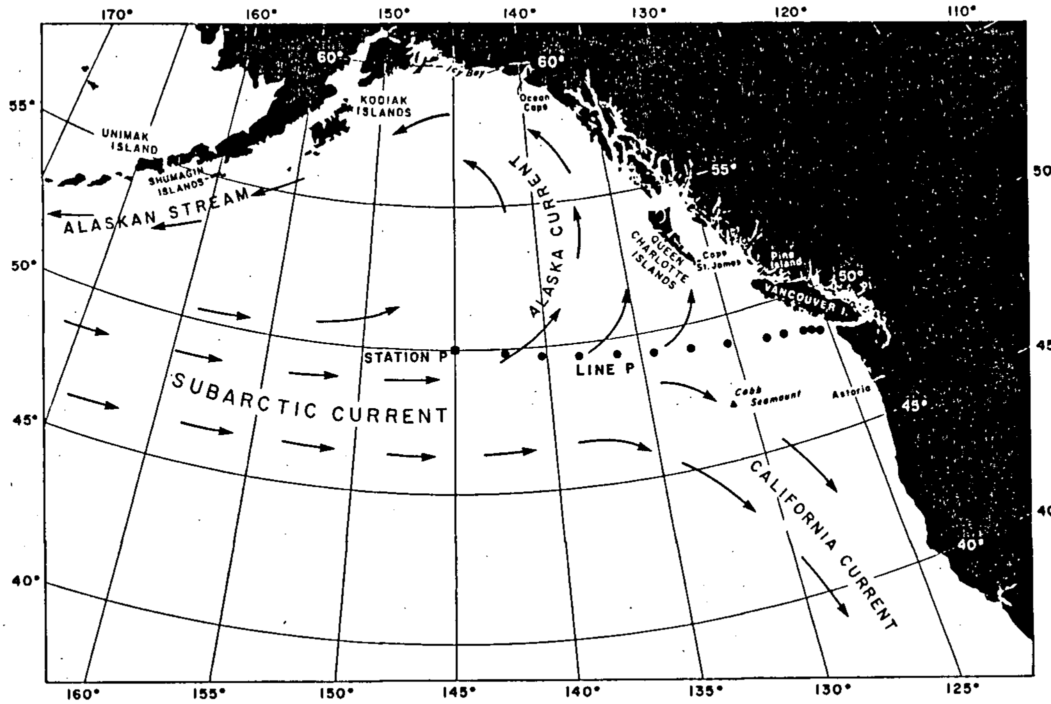

Figure 1. Schematic diagram of the long-term mean circulation in the Northeast Pacific Ocean. (Diagram courtesy of Dr. S. Tabata.)

records (Reed and Schumacher 1984, Warren and Owens 1985, 1988). These studies demonstrated that the Alaskan Stream is a stable, vertically and horizontally coherent current that originates at the head of the Gulf near 56° – 59°N, 145°W where it narrows and intensifies to flow over the continental slope, along the Aleutian Islands, well beyond 180°W. Fig. 2 shows the geopotential topography (0/1500 db) for Feb./Mar. 1980 and illustrates a typical synoptic pattern. The current is often remarkably free of lateral perturbations.

Reed et al. (1980) noted that the Stream has a baroclinic structure extending down to at least 3000 db, with isopycnals sloping downward toward the continental slope. Comparisons between direct current measurements and (computed) geostrophic currents suggest that the Stream is in approximate geostrophic balance (Reed and Schumacher, 1984). Surface currents determined from ship drifts can reach speeds of 100 cm s^{-1} in agreement with those calculated from the geostrophic relations (Reed et al. 1981). The baroclinic transport of the Stream and its variations has been estimated many times. For example, Reed et al. (1980) give the mean transport near Kodiak Island, adjusted for bottom depth variations to a common reference level of 1500 db, as 11.7 Sv with a standard deviation of 2.2 Sv ($1\,\mathrm{Sv} = 10^6\,\mathrm{m^3\,s^{-1}}$). They also report that a deeper reference level of 3000 db increases the baroclinic transport by as much as 5 Sv. Also, from repeated measurements near Cook Inlet, (150°W,58°N), Royer (1981) found that 80% of the baroclinic transport of the Stream occurs within 60 km of the shelf break.

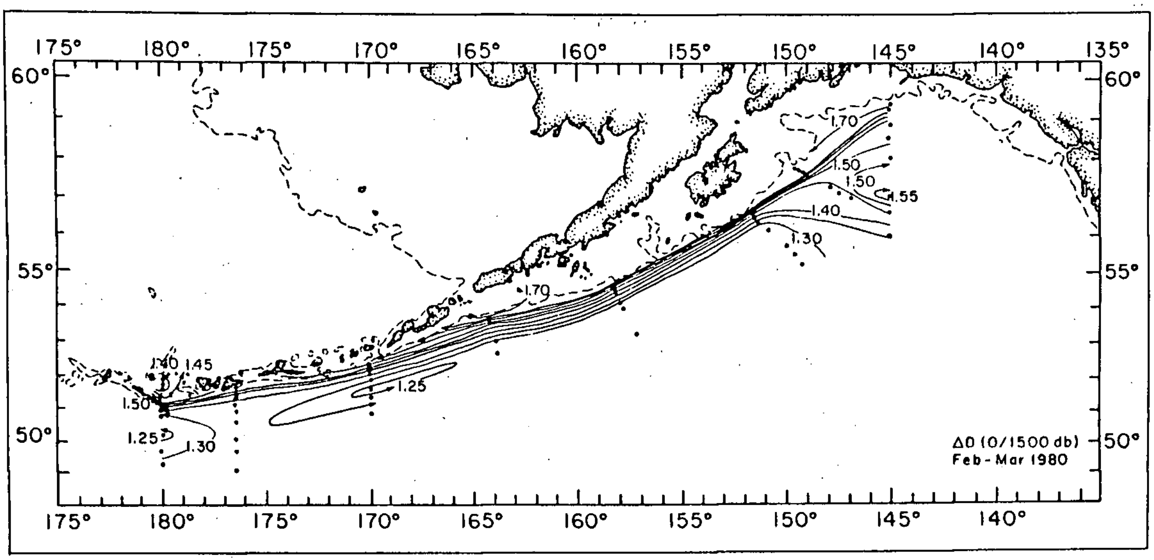

Figure 2. 0/1500 db geopotential topography of the Alaskan Stream (in ΔD, dyn m) for the period of February 11 to March 3, 1980 (from Reed, 1984).

From a detailed observational program conducted during the spring and summer months of 1981 and 1982, Warren and Owens (1988) combined direct current measurements with hydrographic data to construct a profile of the distribution of westward velocity with depth for the Alaskan Stream at 175° W (Fig. 3). The profile, which is representative of conditions during June 1981, shows that the velocity of the Stream increases monotonically from the bottom to a depth of 400 m. These observations indicate that the Stream does not display any flow reversals with depth. From the velocity profile, they estimate that the Alaskan Stream transports 28 Sv across the 175°W meridian.

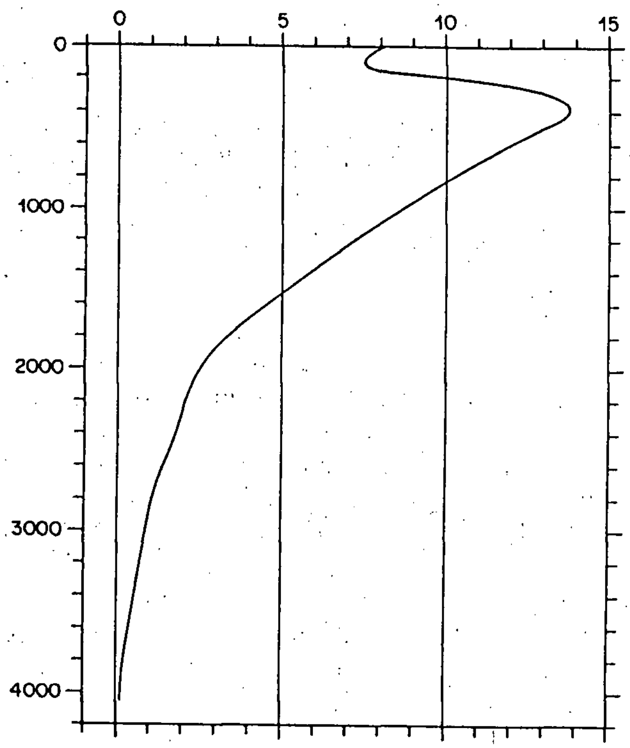

Figure 3. Westward component of geostrophic velocity (cm s^{-1}, abscissa) versus depth (m, ordinate) in the Alaskan Stream at 175°W during June 1981. The profile is adjusted using velocity measurements from a 2000 m current meter (from Warren and Owens, 1988).

Like other western boundary currents, the Alaskan Stream is subject to some degree of mesoscale variability. Reed et al. (1980) presented evidence for the existence of a vertically coherent anticyclonic eddy with a horizontal scale of about 150 km embedded in the Stream near Kodiak Island. Similarly the current meter records of Reed et al. (1981) suggested that an anticyclonic meander had passed their moorings near Kodiak Island. The time scale for this event was about 2 months. A recent AVHRR satellite image of the northern Gulf of Alaska (Fig. 4) confirms the occurrence of anticyclonic lateral meanders in the Alaskan Stream.

Despite these occurrences, the Alaskan Stream is comparatively more stable than other western boundary currents. A relatively straight current is often observed, contrasting, for example with the vigourous meandering that is characteristic of the Gulf Stream. Moreover, the ratio of eddy to mean kinetic energy is usually less than one and much smaller than those obtained from other western boundary currents. Nevertheless, it appears that mesoscale variability increases downstream from Kodiak Island. Fig 4 demonstrates the existence of wave-like lateral fluctuations of the Stream with wavelengths of about 150 km.

2.2 Line P Observations

Line P (Fig. 1) consists of a set of ten hydrographic stations extending from the B.C. coast (48°N, 126°40′W) out to Station P (50°N, 145°W). The Line P data constitutes a relatively long and well sampled time series for the NE Pacific. Data was collected along Line P at monthly intervals from 1959 to 1981, except for the period of Sept. '66 to Mar. '67 during which only a few stations were occupied. Tabata (1983) calculated the baroclinic transport across Line P, which cuts through the northward flowing Alaska Current. The average transport was about 5.2 Sv, relative to 1000 db and 6.9 Sv with a deeper reference level of 1500 db. Accordingly the baroclinic transport across Line P does not balance the transport of the Alaskan Stream. It seems reasonable to assume that some contribution to the transport of the Stream is due to northward flow west of Station P, since Line P does not extend

Figure 4. AVHRR (Advanced Very High Resolution Radiometry) image of the northwestern Gulf of Alaska on March 1, 1987 from the NOAA–10 satellite. Thermal variations in the ocean surface waters are sense by the satellite. Darker tones are assigned to higher temperatures. The Alaskan Stream is evident as a dark ribbon of water following the coastline. A meander in the Alaskan Stream with a scale of 150 km occurs on the right side of the image, and appears as a lump of warm water along the coast. Note also the occurrence of wavelike perturbations in the current further downstream. Photo courtesy of Dr. T. Royer.

across the entire Alaska Current.

2.3 Sitka Eddy

From an analysis of hydrographic data collected in the Gulf of Alaska *during* the period 1954-67, Tabata (1982) noted the repeated occurrence of an anticyclonic, baroclinic eddy located a few hundred kilometers west of Sitka, Alaska. This eddy has also been detected in the trajectories of satellite-tracked drifting buoys (Kirwan et al. 1978) and in infrared satellite imagery (Mysak 1985). It should be noted that, in the present context, the term 'eddy' usually refers to closed streamline features. Tabata (1982) also applied the term to features with anticyclonic curvature; his data often did not have enough spatial coverage to determine whether the streamlines were closed.

The Sitka eddy typically has a diameter of 200-300 km and is characterized by a warm, low salinity core with depressed isopycnals. It has a surface–intensified, baroclinic structure reaching depths of up to 2000 m. The eddy is usually found in the vicinity of (57°N, 138°W). The 0/1000 db geopotential contours from spring of 1958 shown in Fig. 5 illustrate a typical, well developed Sitka eddy. Surface axial speeds vary from an average of $15\,\mathrm{cm\,s^{-1}}$ to a maximum of 30–40 $\mathrm{cm\,s^{-1}}$ for the intense eddy observed in spring of 1961 (Tabata, 1982). The average 0/1000 db baroclinic transport of the eddy is about 5 Sv but can reach a maximum of 8 Sv. The eddy appears to form locally during the spring-summer period of a given year and then is thought to drift westward at speeds of 1–2 $\mathrm{km\,day^{-1}}$ and to persist for up to a year. The appearance of the eddy is to some extent intermittent. Although it has been observed in the majority of the years for which data are available, there are some years in which it is not present.

In a recent note, Gower (1989) examined sea surface anomalies over the Gulf of Alaska in the Geosat altimeter data. An eddy–like feature, bearing several of the characteristics that Tabata (1982) associated with the Sitka eddy was found during the period spring–fall, 1986. The surface height anomaly that Gower identified as a Sitka eddy propagated westwards at a speed of 1.2–2 cm $\mathrm{s^{-1}}$ from the formation region off Sitka, Alaska. Gower estimated the height anomaly associated with the

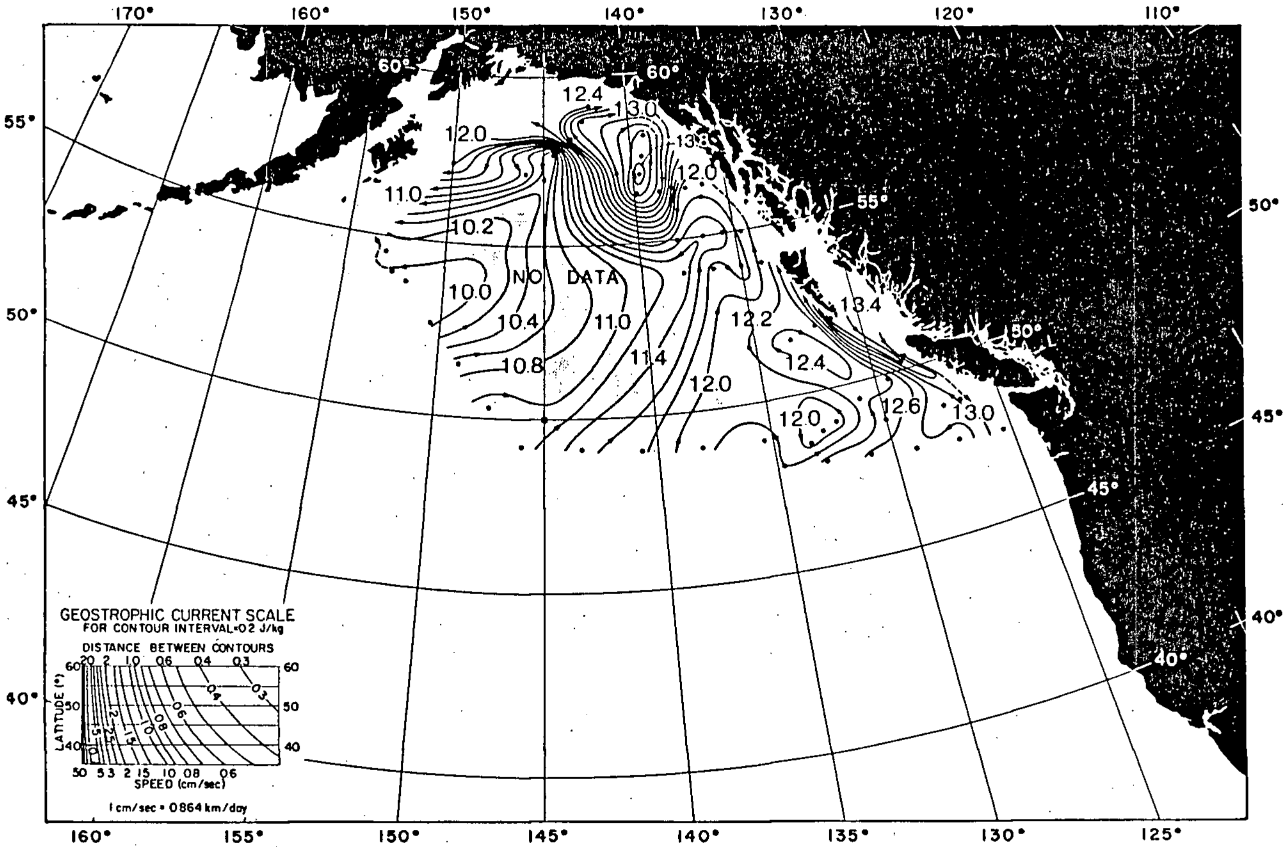

Figure 5. 0/1000 db geopotential topography of the eastern Gulf of Alaska (J kg^{-1}) for the period of March to April, 1958 (from Tabata, 1982). The Sitka eddy is centered at 140°W, 57°N.

eddy to be about 30 cm, yielding surface geostrophic velocities of 25 cm s^{-1}. The presence of the Sitka eddy appears to be a consistently recurring characteristic of the flow on the eastern Gulf of Alaska. Gower also traced the (westward) movement of other sea surface height anomalies in the Gulf. The Geosat data generally show that the sea surface of this region has considerably more structure than revealed by the hydrographic surveys of the area.

Swaters and Mysak (1985) proposed that the Sitka eddy is generated by the interaction of the flow of the Alaska Current with the local bottom topography.

Mysak (1985) suggested that the strength of the northward flow over the topography may be a controlling factor in the formation of an eddy. He finds a correlation between the magnitude of the baroclinic transport across Line P and the appearance of a Sitka eddy, and in turn, relates the Line P transport to the intensity of the atmospheric winter circulation over the Gulf.

2.4 Atmospheric Variability

The wintertime atmospheric circulation over the North Pacific is dominated by the presence of a strong cyclone, known as the Aleutian Low, which is typically centered at 50°N, 180°W. In the spring this low pressure system relaxes in intensity and shifts northward and westward. During the summer months the sea surface pressure distribution over the Gulf of Alaska is governed by the high pressure system centered at 35°N, 160°W which is known as the California High. Emery and Hamilton (1985) have shown that the seasonal cycle in the sea-surface atmospheric pressure over the Gulf of Alaska is subject to considerable interannual variability and that this may be related to major ENSO events in the tropical Pacific.

From the point of view of the upper ocean circulation, the wind stress curl is the most important atmospheric field. Like the sea surface pressure, the wind stress curl displays a substantial seasonal signal. The mean January and July wind stress curl fields over the Gulf of Alaska, constructed from the monthly wind stress data compiled by Hellerman and Rosenstein (1983), are shown in Fig. 6. The annual mean zero wind stress curl contour lies at approximately 45°N and is nearly zonal in orientation (see Fig. 10 in Ch. 4). During summer it shifts northward to about 48°N as the wind stress curl over the Gulf weakens but remains positive. The mean winter wind stress curl is considerably more intense than the annual mean and reflects the presence of the Aleutian low. The latitudinal position of the maximum of the curl is about 56°N and is subject to only moderate seasonal variation.

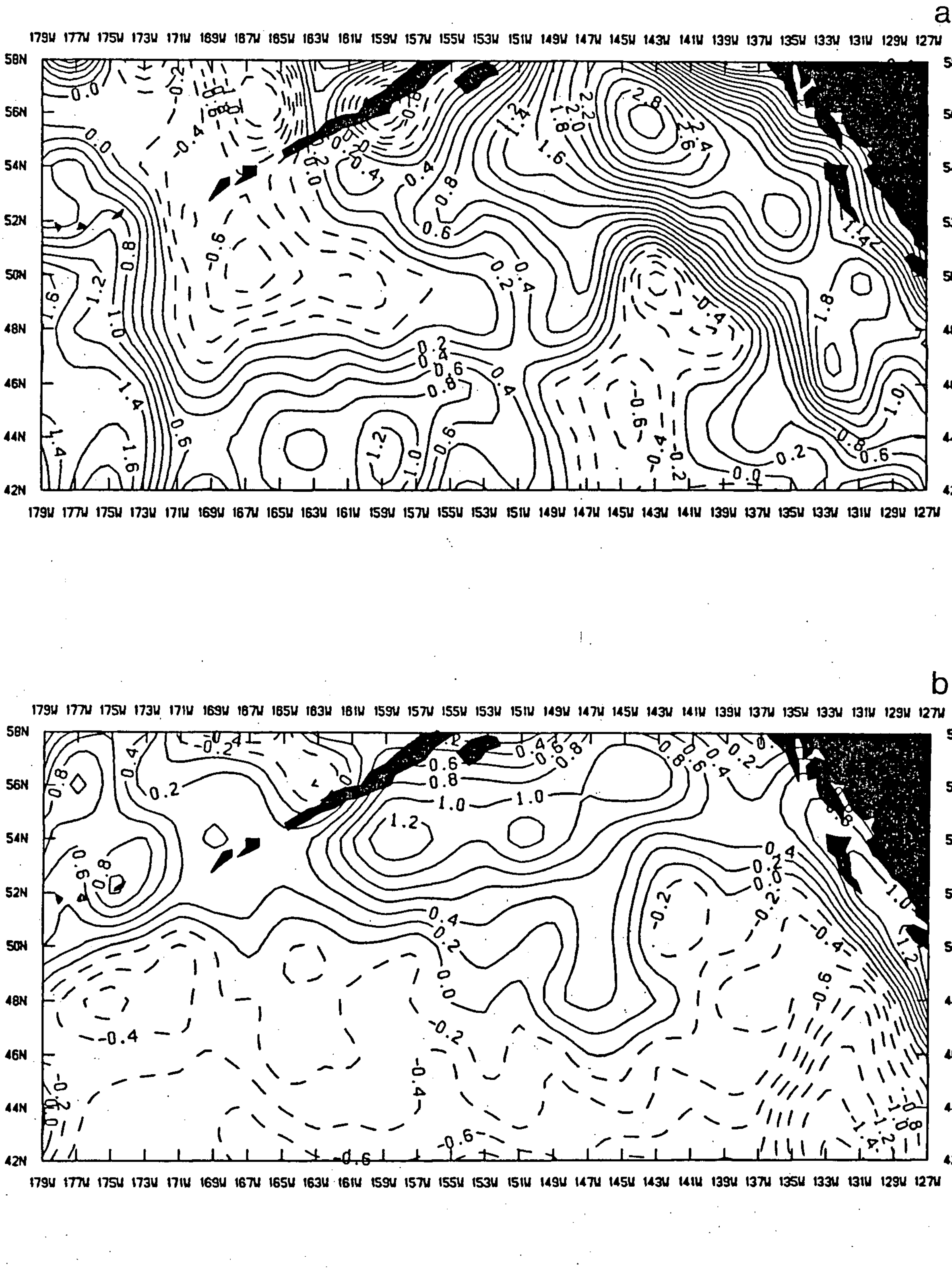

Figure 6. Mean wind stress curl fields computed from the data of Hellerman and Rosenstein (1983) over the NE Pacific Ocean for (a) the month of January and (b) the month of July. The contour interval is 0.2×10^{-7} N m^{-3}

2.5 Seasonal and Interannual Variability

The atmospheric circulation over the Gulf of Alaska shows very pronounced changes on seasonal time scales. This has led researchers to inquire whether the oceanic circulation likewise displays this strong seasonal variability. The observational record has tended to indicate that this is not the case. Tabata (1989) found that there was no statistically significant seasonal signal in the Line P 0/1000 db transport data. Reed et al. (1980) found no systematic seasonal variation to the 0/1500 db baroclinic transport of the Alaskan Stream. Royer (1981), using unadjusted transports relative to 1500 db, detected a small seasonal variation of about 1.3 Sv on a mean transport of about 9.5 Sv, with the maximum occurring in March.

From hydrographic sections taken over the NE Pacific during July and August of 1981, Royer and Emery (1987) found that a major change in the location of the Alaskan Gyre had occurred. The gyre center was shifted westward by some 700 km and, east of 145°W, there was a cessation of the usual northward flow of the Alaska Current. Associated with this, the transport feeding the Stream from the head of the gulf decreased by nearly a factor of two and there was a large northward transport across the southern boundary of the Stream between 150 and 165°W (Reed, 1984). These unusual conditions are believed to have persisted for at least one or two months duration. Because this situation has been observed only infrequently, this anomalous behaviour of the subarctic gyre is usually referred to as 'interannual variability' of the circulation. The observational record indicates that a similar and equally extreme event also occurred in summer 1958 (Royer and Emery, 1987).

Although the nature and causes of these changes is largely a matter of speculation at present, two hypotheses have been advanced. Reed (1984) attributed the anomalous conditions to a westward shift of the atmospheric circulation and a corresponding collapse of the wind stress curl on the eastern side of the basin during the three months or so prior to the time of the observations. Royer and Emery (1987) dispute this explanation and offer an alternative one. They suggest that an interaction of the flow with a group of seamounts found near 51°N and 145°W occurs. The latitudinal position of the North Pacific Current, which feeds into the northward flowing Alaska Current, is the controlling factor in this scheme. If the westward flowing North Pacific Current is located sufficiently far north, the seamounts are thought to deflect it such that the northward flow of the Alaska Current now lies to the west of the seamount region. In the more usual case the North Pacific Current flows further south and is not deflected so that northward flow occurs to the east of the seamount region.

3. Quasi–geostrophic numerical model

3.1 Governing Equations

We consider a beta–plane model of the ocean with the x and y coordinates representing distance in the eastward and northward directions respectively. The vertical variation of density is discretized into a finite number (N) of immiscible layers of constant density ρ_k and of thickness H_k (Fig. 7) with $k = 1, \ldots, N$. Variations in the depth of the fluid about a mean depth H are denoted by $h_B(x, y)$ and are contained exclusively within the lowest layer. The reduced gravity at the interfaces between layers is given by $g'_{k+\frac{1}{2}} = \frac{g(\rho_{k+1}-\rho_k)}{\rho_0}$, where g is the gravitational constant and ρ_0 is a reference density. A whole number subscript denotes a layer while a fractional subscript (e.g. $k + \frac{1}{2}$) denotes an interface. The quasi–geostrophic equations governing the conservation of vorticity and the interface displacement for a layered ocean on a beta plane are given by (e.g., Pedlosky 1979)

$$\begin{aligned} \frac{\partial \nabla^2 \psi_k}{\partial t} =& J(f + \nabla^2 \psi_k, \psi_k) + \frac{f_0}{H_k}(w_{k-\frac{1}{2}} - w_{k+\frac{1}{2}}) + A_H \nabla^p \psi_k \\ &+ \delta_{1,k} \frac{curl_z \boldsymbol{\tau}}{\rho_0 H_1} - \delta_{N,k} \epsilon \nabla^2 \psi_k \qquad \text{for} \quad k = 1, \ldots, N \end{aligned} \tag{3.1}$$

$$\frac{\partial(\psi_k - \psi_{k+1})}{\partial t} = J(\psi_k - \psi_{k+1}, \psi_{k+\frac{1}{2}}) - \frac{g'_{k+\frac{1}{2}}}{f_0} w_{k+\frac{1}{2}} \qquad \text{for} \quad k = 1, \ldots, N-1. \tag{3.2}$$

The streamfunction is given by ψ_k, the vertical interfacial velocity by $w_{k+\frac{1}{2}}$, ∇^2 is the horizontal Laplacian operator and $J(a, b) = a_x b_y - a_y b_x$ is the Jacobian operator (the x and y. denote differentiation). The Coriolis parameter is $f = f_0 + \beta y$, where f_0 is the value of the Coriolis parameter at the point that the beta plane is tangent to the earth and β is the latitudinal gradient of this parameter at this point. A_H is the lateral viscosity coefficient, ϵ is the linear bottom friction coefficient and $\delta_{i,j}$ is the Kronecker delta. The order of the dissipation operator is given by p. The streamfunction evaluated at the interfaces is a weighted average of the streamfunction from adjacent layers: $\psi_{k+\frac{1}{2}} = (H_{k+1}\psi_k + H_k \psi_{k+1})/(H_k + H_{k+1})$.

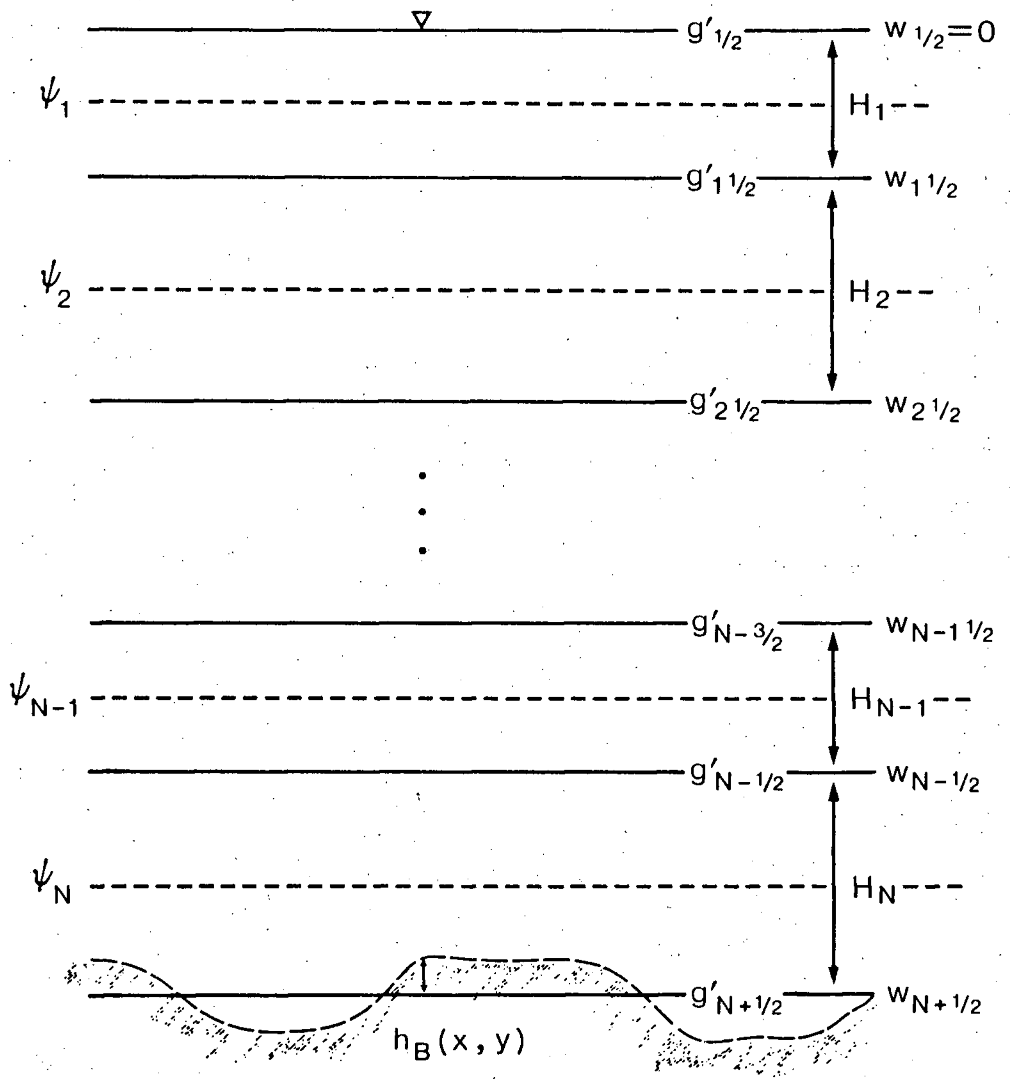

Figure 7. The vertical structure of an N–layer quasi–geostrophic model.

The horizontal geostrophic velocity components within a layer are given by

$$(u_k, v_k) = (-\frac{\partial \psi_k}{\partial y}, \frac{\partial \psi_k}{\partial x}), \tag{3.3}$$

while the interface height perturbations (positive upwards) are given by

$$h_{k+\frac{1}{2}} = \frac{f_0}{g'_{k+\frac{1}{2}}}(\psi_{k+1} - \psi_k). \tag{3.4}$$

Bottom topographic variations are incorporated in the model through the bottom boundary condition on the vertical velocity, viz,

$$w_{N+\frac{1}{2}} = -J(h_B, \psi_N). \tag{3.5}$$

In addition, McWilliams (1977) showed that the constraint

$$\int\int w_{k+\frac{1}{2}} dxdy = 0, \qquad \text{for} \quad k = 1, \ldots, N-1 \tag{3.6}$$

is necessary to ensure that mass is conserved in each layer of a closed domain.

The top layer of the model ocean is directly driven by the vertical component of the curl of the wind stress, $curl_z\boldsymbol{\tau}$, which is a forcing function that we will specify below. The effect of the wind stress curl is to produce an Ekman pumping tendency that is equivalent to a body force acting on the top layer.

Dissipation is included in the model through a horizontal friction and a linear bottom friction acting on the lowest layer. With $p = 4$ the dissipation operator reduces to the conventional Laplacian friction while $p = 6$ results in the scale selective biharmonic friction (Holland, 1978).

Equations (3.1)–(3.5) may be combined to yield an expression relating changes in the potential vorticity of a fluid parcel, Q_k, to dissipation and the external forcing, viz.,

$$\frac{D_k Q_k}{Dt} = A_H \nabla^p \psi_k + \delta_{1,k}\frac{curl_z\boldsymbol{\tau}}{\rho_0 H_1} - \delta_{N,k}\epsilon\nabla^2\psi_k \qquad \text{for} \quad k = 1, \ldots, N. \tag{3.7}$$

with

$$Q_k = \nabla^2\psi_k + f(y) + \frac{f_0}{H_k}(h_{k+\frac{1}{2}} - h_{k-\frac{1}{2}}) + \delta_{N,k}\frac{f_0 h_B}{H_N},$$

and

$$\frac{D_k}{Dt} \equiv \frac{\partial}{\partial t} + u_k\frac{\partial}{\partial x} + v_k\frac{\partial}{\partial y},$$

a material derivative for the layer k.

3.2 Method of Solution

Equations (3.1) and (3.2) with the boundary condition (3.5) are solved using finite differences over a uniform mesh of grid points representing the Gulf of Alaska. Using (3.2) and (3.5) to eliminate the vertical velocity in (3.1), a set of N-coupled equations is obtained that can be written in matrix form as

$$\partial_t(\nabla^2\Psi - \mathbf{M}\Psi) = \mathbf{R}, \tag{3.8}$$

where Ψ is a column vector of the layer streamfunction, $\Psi^T = (\psi_1, \psi_2, \ldots, \psi_N)$, and $\mathbf{M}$ is the tridiagonal matrix of coupling coefficients between layers. The nonzero row elements of $\mathbf{M}$ are of the form

$$-\frac{f_0^2}{g'_{k-\frac{1}{2}}H_k}, \quad \left(\frac{f_0^2}{g'_{k-\frac{1}{2}}H_k} + \frac{f_0^2}{g'_{k+\frac{1}{2}}H_k}\right), \quad \text{and} \quad -\frac{f_0^2}{g'_{k+\frac{1}{2}}H_k},$$

where for mathematical convenience we take $g'_{\frac{1}{2}} = g'_{N+\frac{1}{2}} = \infty$. The column vector $\mathbf{R}$ contains the nonlinear, dissipative and forcing terms. The elements of $\mathbf{R}$ are given by

$$J(f + \nabla^2\psi_k + \delta_{N,k}\frac{f_0 h_B}{H_N}, \psi_k) + \frac{f_0^2}{g'_{k-\frac{1}{2}}H_k}J(\psi_{k-1} - \psi_k, \psi_{k-\frac{1}{2}})$$
$$-\frac{f_0^2}{g'_{k+\frac{1}{2}}H_k}J(\psi_k - \psi_{k+1}, \psi_{k+\frac{1}{2}}) + A_H\nabla^p\psi_k + \delta_{1,k}\frac{curl_z\boldsymbol{\tau}}{\rho_0 H_1} - \delta_{N,k}\epsilon\nabla^2\psi_k.$$

Following Bengtsson and Temperton (1979), the layer equations (3.8) are decoupled into a set of modal equations by diagonalizing the coupling matrix $\mathbf{M}$, which is written as

$$\mathbf{M} = \mathbf{P}\mathbf{\Lambda}\mathbf{P}^{-1}, \tag{3.9}$$

where $\mathbf{P}$ is a matrix whose columns are the eigenvectors of $\mathbf{M}$. $\mathbf{P}$ satisfies the relation

$$\mathbf{MP} = \mathbf{P\Lambda}, \tag{3.10}$$

where $\Lambda = diag(\lambda_1^2, \lambda_2^2, \ldots, \lambda_N^2)$ is a diagonal matrix of eigenvalues. The significance of the eigenvalues is that they are the reciprocal of the square of the Rossby deformation radii of each mode. Since the determinant of $\mathbf{M}$ is zero, one of the eigenvalues of $\mathbf{M}$ is identically zero. This eigenvalue is associated with the barotropic mode which, in this rigid–lid model, has an infinite Rossby radius.

Substituting (3.9) into (3.8) and multiplying the left hand side by $\mathbf{P}^{-1}$, we obtain the decoupled system

$$\partial_t(\nabla^2\Phi - \Lambda\Phi) = \mathbf{P}^{-1}\mathbf{R} \tag{3.11}$$

where $\Phi = \mathbf{P}^{-1}\Psi$ is a column vector consisting of one barotropic mode, ϕ_1, and $N-1$ baroclinic modes, $\phi_i, \quad i = 2, \ldots, N$.

To integrate the system (3.11) forward in time we evaluate derivatives using centered space and time differences. The Jacobian operator given by Arakawa (1966) is employed for the nonlinear terms to ensure that the space differencing conserves kinetic energy and enstrophy. The terms in $\mathbf{R}$ are evaluated at time level n with the exception of the dissipation terms, which are evaluated at time level $n-1$ to ensure numerical stability. A Robert filter (Asselin 1972) with a very weak filter coefficient is applied at each time step to suppress the development of a computational mode in the solution.

Introducing the time differencing into (3.11) and denoting time levels by superscripts we have

$$(\nabla^2 - \Lambda)\Phi^{n+1} = 2\,\Delta t\,\mathbf{P}^{-1}\mathbf{R}^{(n,n-1)} + (\nabla^2 - \Lambda)\Phi^{n-1}, \tag{3.12}$$

where Δt is the time step increment. Given the streamfunction fields at time levels $n-1$ and n, we can evaluate the right hand side of (3.12). To obtain the Φ^{n+1} fields we then have to solve N Helmholtz equations.

These elliptic equations are solved in a domain Ω, with an irregular (i.e., non-rectangular) boundary $\partial\Omega$, on which Dirichlet boundary conditions are specified. The condition of no normal flow at the side walls of the domain requires that the ϕ_i be constant along $\partial\Omega$. The value of the ϕ_i on $\partial\Omega$ is determined by the constraint (3.6).

Since the interfacial vertical velocity fields are due entirely to the baroclinic modes, this constraint is met by requiring that

$$\int\int_{\Omega} \phi_i \; dxdy = 0, \qquad \text{for} \quad i = 2, \ldots, N. \tag{3.13}$$

Thus for each baroclinic mode we adopt the method of Holland (1978) and let the solution to each equation, of the form

$$(\nabla^2 - \lambda_i^2)\phi_i = f_i(x, y), \qquad \text{for} \quad i = 2, \ldots, N,$$

be $\phi_i = \phi_i' + C_i(t)\ \varphi_i$, where $\phi_i' = 0$ on $\partial\Omega$ and the φ_i satisfy

$$(\nabla^2 - \lambda_i^2)\varphi_i = 0, \qquad \varphi_i = 1 \quad \text{on} \quad \partial\Omega, \quad \text{for} \quad i = 2, \ldots, N.$$

The φ_i fields are independent of time and are determined only once at the outset of the integration. The constants $C_i(t)$ are determined from (3.13) and are given by

$$C_i(t) = -\frac{\int\int_{\Omega} \phi_i' dxdy}{\int\int_{\Omega} \varphi_i dxdy} \qquad \text{for} \quad i = 2, \ldots, N. \tag{3.14}$$

The barotropic mode, ϕ_1, is taken, without loss of generality, to be zero on $\partial\Omega$.

The finite difference Helmholtz equations are integrated in an irregular domain using a capacitance matrix technique (Hockney 1970) in conjunction with a direct Poisson solver (Swarztrauber 1984). We have included a brief description of our capacitance matrix algorithm in Appendix A.

Equations (3.1) and (3.2) are of fourth or sixth order and thus require the specification of not only the streamfunction, ψ_k, but also the relative vorticity, $\nabla^2\psi_k$, on $\partial\Omega$. Both the Laplacian friction term and the Arakawa Jacobian require $\nabla^2\psi_k$ as boundary data. This allows the relative vorticity generated at a boundary to be diffused into the interior. The biharmonic friction operator also requires that an additional boundary condition (on $\nabla^4\psi_k$) be specified. The boundary data on the relative vorticity depend on whether there is free-slip (zero stress) or no-slip at the boundary. In the free–slip case, $\nabla^2\psi_k = 0$ on $\partial\Omega$, while, in the no–slip case, the boundary vorticity evolves as part of the solution. For a no–slip wall the boundary vorticity is evaluated according to a first–order accurate method, due originally to Thom (1928) and used by Blandford (1971). At corner points the vorticity is evaluated using a variant of this method which effectively rounds the corner (see Roache (1973), p. 170, method no. 4). In the case of biharmonic friction, the boundary condition, $\nabla^4\psi_k = 0$ on $\partial\Omega$, is adopted.

3.3 Model Domain

The numerical integration is performed in Cartesian coordinates on a uniform mesh with a resolution of 20 km in the two horizontal coordinates. A discussion of the adequacy of the horizontal resolution is given in Appendix B. The domain, which extends up to 3200 km in the east–west direction and 1480 km in the north–south direction is shown in Fig. 8 along with contours of the bottom topography. The sidewall boundary along the continental margin was chosen to coincide as nearly as possible with the 1700 m depth contour. A mid–ocean boundary is placed to the south at around 45°N, a latitude corresponding approximately with the southern limit of the subpolar gyre and also with the zero contour of the annual mean wind stress curl. A second mid–ocean boundary forms a western wall at approximately 170°W.

A map projection was used to identify the grid points on the beta plane with a spherical coordinate on the earth. In this way a bottom depth value could be associated with each grid point. The Lambert equal–area projection was employed, but others, such as the Mercator projection, gave nearly identical results. The projection does introduce some distortion, although area is preserved in the transformation. A horizontal line in the domain no longer corresponds with a latitude circle. For example the southern boundary varies from 44°N at the east and west corners to 46°N at the center. The relations for the map projection were obtained from Snyder (1982).

A weak nine point filter (Shapiro 1970) was applied to the bottom topography to remove the small–scale bottom features which are poorly resolved by the grid. The resulting smoothed field was employed in the numerical model. Prominent topographic features, such as the Aleutian trench and various seamounts are evident in the bottom contours of Fig. 8.

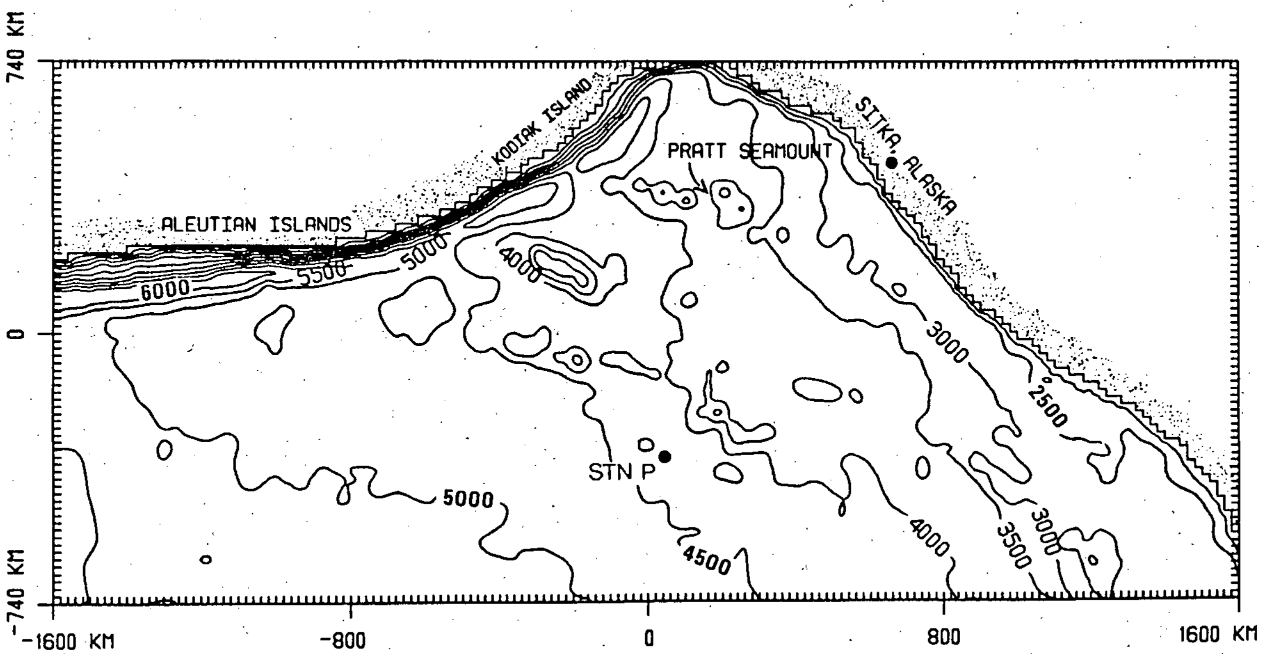

Figure 8. Map showing the model domain and bottom topography. The contour interval is 500 m.

In the vertical direction a three layer ($N = 3$) density structure is adopted. The layer thicknesses are: $H_1 = 200$ m, $H_2 = 600$ m and $H_3 = 4200$ m. The reduced gravities at the interfaces are $g'_{1\frac{1}{2}} = 1.0\times10^{-2}$m s^{-2} and $g'_{2\frac{1}{2}} = 0.5\times10^{-2}$m s^{-2}. With these values the deformation radii of the model are 17.2 km for the first baroclinic mode and 9.6 km for the second baroclinic mode. This compares well with average values of 17.6 km and 9.8 km for the deformation radii computed from hydrographic data collected in the Gulf of Alaska (Willmott and Mysak 1980).

3.4 Sponge Layer

With the 'artificial' western wall inserted near 170°W, the flow in this area will be necessarily unrealistic and consequently we wish to isolate this region so that it has as little effect as possible on the flow to the east. This is achieved by placing a region of enhanced friction, called a sponge layer, adjacent to the boundary. The method of Barnier (1986) was utilized to implement the sponge layer. This requires that a frictional term, similar to the bottom friction term for the lowest layer, be introduced to the right side of equation (3.1) for each layer.

The sponge layer was chosen to be 16 grid intervals (320 km) in width, which is wide enough to encompass the current along the western wall. The frictional coefficients gradually increase over 8 grid intervals from their interior values (which are zero for all but the lowest layer) to the maximum value of 1×10^{-6} s^{-1} which is an order of magnitude larger than the bottom friction coefficient in the interior. With these coefficients so specified, the sponge layer acts to damp fluctuations at the western boundary, independently of the spatial scale of the motion.

The effect of the sponge layer is to remove some of the cyclonic vorticity imparted to the fluid by the wind stress curl. Numerical experiments show that, in the absence of a sponge layer, the flow near the western wall develops intense, vertically coherent eddies. These eddies create the horizontal gradients necessary for the Laplacian friction to dissipate the excess cyclonic vorticity of the fluid particles. This must occur (in a steady state) before the particles can reenter the interior flow. The sponge layer is effective in suppressing the formation of such vorticies at the western boundary and thus allows the fluid that has reached the western wall to reenter the interior flow smoothly.

3.5 Energy and Vorticity Diagnostics

Several diagnostic tools have been developed to understand and quantify the complex response of the model. While several of these simply provide kinematical descriptions of the flow field (e.g., variance-preserving spectra), the energy and vorticity diagnostics yield insights into the dynamical processes which constitute the model response. Holland (1978) presents an energy diagnostic which reveals the potential and kinetic energy exchanges between the mean and fluctuating components of the flow. This is useful to identify the relative importance of barotropic and baroclinic instability processes. An alternative energy diagnostic, which reveals the energy transfers between vertical modes, has been adopted here. This form of energy diagnostic is better suited to unravel the modifications to the model solution arising from the presence of bottom topography. An equation is given below for the rate of energy transfer into each vertical mode. For simplicity, and to reduce the number of energy transfer terms, the partition between mean and fluctuating components of the flow is not made here.

Let $\psi_k(x,y,t) = \sum_{m=1}^{N} F_m^k\ \phi_m(x,y,t)$ where the F_m^k are the elements of the matrix **P** defined in eqn. (3.10). The latter are normalized such that

$$H^{-1} \sum_{k=1}^{N} H_k\, F_i^k\, F_j^k = \delta_{i,j}. \tag{3.15}$$

Flierl (1978) shows that the QG evolution equations for the layer streamfunction (3.1 and 3.2) may be transformed into evolution equations for the amplitude of normal modes, ϕ_m. The result is

$$\begin{aligned} \frac{\partial}{\partial t}(\nabla^2 - \lambda_m^2)\phi_m + \beta\frac{\partial \phi_m}{\partial x} &= -\sum_i\sum_j \xi_{i,j,m}\, J(\phi_i, (\nabla^2 - \lambda_j^2)\phi_j) \\ &+ \frac{F_m^1}{H}\, \frac{curl_z \boldsymbol{\tau}}{\rho_0} - \frac{F_m^N}{H} \sum_j F_j^N\, J(\phi_j, f_0\, h) \\ &- \frac{F_m^N\, H_N}{H}\, \epsilon \sum_j F_j^N\, \nabla^2 \phi_j + A_H \nabla^p \phi_m - s(x)\, \nabla^2 \phi_m. \end{aligned} \tag{3.16}$$

The sponge layer friction coefficient is denoted by $s(x)$ and is independent of the layer index. In addition,

$$\xi_{i,j,m} = \frac{1}{H} \sum_{k=1}^{N} F_i^k F_j^k F_m^k H_k \tag{3.17}$$

is the triple correlation coefficient between modes. We obtain an energy equation by multiplying (3.16) by ϕ_m^* and integrating over the entire domain, where

$$\phi_m^* = \phi_m(x,y,t) - \phi_m(x_b,y_b,t) \tag{3.18}$$

and (x_b, y_b) is any point on the boundary. This results in the following energy equation:

$$\begin{aligned}
\frac{\partial}{\partial t}(KE_m + PE_m) = & \int\int_\Omega [\phi_m^* \sum_i \sum_j \xi_{i,j,m}\, J(\phi_i, (\nabla^2 - \lambda_j^2)\,\phi_j)]\, dA \\
& - \frac{F_m^1}{H} \int\int_\Omega [\phi_m^* \frac{curl_z \boldsymbol{\tau}}{\rho_0}]\, dA + \frac{F_m^N}{H} \int\int_\Omega [\phi_m^* \sum_j F_j^N\, J(\phi_j, f_0\, h)]\, dA \\
& + \frac{F_m^N\, H_N}{H}\, \epsilon \int\int_\Omega [\phi_m^* \sum_j F_j^N\, \nabla^2 \phi_j]\, dA - A_H \int\int_\Omega [\phi_m^* \nabla^p \phi_m]\, dA \\
& + \int\int_\Omega [s(x)\phi_m^*\, \nabla^2 \phi_m]\, dA.
\end{aligned} \tag{3.19}$$

The kinetic and potential energies are given by

$$\begin{aligned}
KE_m &= \frac{1}{2} \int\int_\Omega [\nabla \phi_m^* \cdot \nabla \phi_m]\, dA, \qquad \text{and} \\
PE_m &= \frac{\lambda_m^2}{2} \int\int_\Omega [\phi_m^*\, \phi_m]\, dA,
\end{aligned} \tag{3.20}$$

respectively. The first term on the right hand side of (3.19) represents the transfer of energy to mode m from the nonlinear interaction of mode i and mode j. Since the nonlinear interactions effect only a redistribution of energy among the modes, the summation of this term over all the modes is zero. The second term gives the rate of transfer of energy from the wind stress curl to mode m. The next term gives the rate of transfer to mode m from the interaction of the other modes with the bottom topography. This term also involves only a redistribution of energy among the modes. The last three terms give the rate of dissipation of mode m energy to bottom friction, horizontal friction and sponge layer friction respectively. The energy transfers are shown schematically for a model with 3 layers (modes) in Fig. 9.

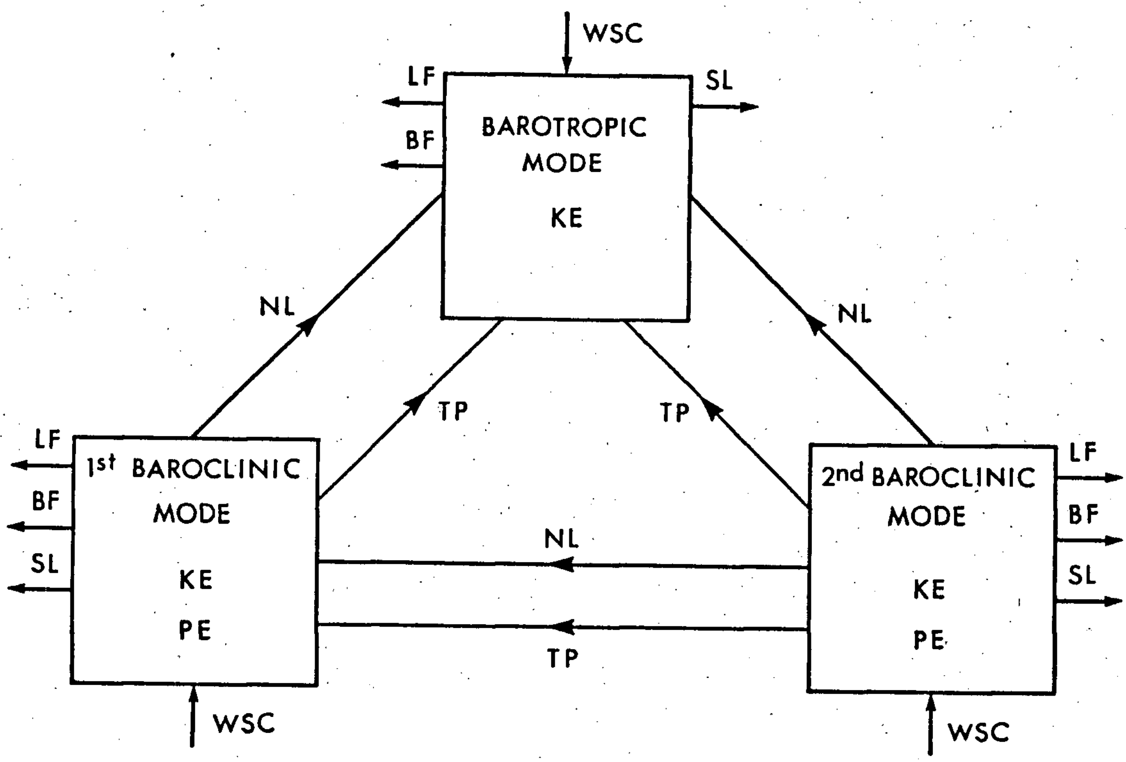

Figure 9. Schematic diagram showing the energy transfers between the three vertical modes. WSC stand for the transfer due to the wind stress curl, LF for that due to Laplacian friction, BF for that due to bottom friction, SL for that due to sponge layer friction, TP for that due to bottom topography and NL for that due to nonlinear interactions between modes. In this diagram, arbitrary directions were chosen for the sense of the energy transfers between the modes.

A different perspective on the model solution is obtained through the construction of vorticity budgets. In contrast to the energy transfers which are integrated over the entire domain, the vorticity budgets are examined over subregions to determine the geographical variation of the dominant vorticity balances. To obtain local vorticity budgets it is useful to effect a Reynold's decomposition of the streamfunction fields into mean and fluctuating components. These are defined respectively as

$$\overline{\psi}_k(x,y) = \frac{1}{T}\int_0^T \psi_k(x,y,t)dt, \qquad \text{and}$$
$$\psi_k'(x,y,t) = \psi_k(x,y,t) - \overline{\psi}_k, \tag{3.21}$$

where T is the averaging period (usually ten years). This allows for an examination of the relative importance of mean and eddy vorticity terms and of the dominant vorticity balances over the domain.

The vorticity analysis closely follows that of Harrison and Holland (1981). Separating the streamfunction into mean and eddy components (according to (3.21)), in (3.1), and time–averaging, we obtain the following mean vorticity equation for layer k:

$$\begin{aligned}\overline{\frac{\partial \nabla^2 \psi_k}{\partial t}} &= PADV + MADV + EADV + STR_{k-\frac{1}{2}} - STR_{k+\frac{1}{2}} \\ &\quad + DISS + BFRIC + CURL + TOPO.\end{aligned} \tag{3.22}$$

The terms in this equation are given by:

$$\begin{aligned}
PADV &= J(f, \overline{\psi_k}),\\
MADV &= J(\nabla^2\overline{\psi_k}, \overline{\psi_k}),\\
EADV &= J(\overline{\nabla^2\psi_k', \psi_k'}),\\
STR_{k-\frac{1}{2}} &= \frac{f_0^2}{g'_{k-\frac{1}{2}}H_k}\left[\, J(\overline{\psi_{k-1}} - \overline{\psi_k}, \overline{\psi_{k-\frac{1}{2}}}) + J(\overline{\psi'_{k-1} - \psi'_k, \psi'_{k-\frac{1}{2}}})\right],\\
STR_{k+\frac{1}{2}} &= \frac{f_0^2}{g'_{k+\frac{1}{2}}H_k}\left[\, J(\overline{\psi_k} - \overline{\psi_{k+1}}, \overline{\psi_{k+\frac{1}{2}}}) + J(\overline{\psi'_k - \psi'_{k+1}, \psi'_{k+\frac{1}{2}}})\right],\\
DISS &= A_H \nabla^p \overline{\psi_k},\\
BFRIC &= \delta_{N,k}\, \epsilon \nabla^2 \overline{\psi_k},\\
CURL &= \delta_{1,k}\, \frac{\overline{curl_z \boldsymbol{\tau}}}{\rho_0 H_1},\\
TOPO &= \delta_{N,k}\, J(\frac{f_0 h_B}{H_N}, \overline{\psi_k}).
\end{aligned}$$

$PADV$ is the mean advection of planetary vorticity tendency, $MADV$ the mean advection of mean relative vorticity tendency, and $EADV$ the eddy advection of eddy relative vorticity tendency. The two stretching terms $STR_{k-\frac{1}{2}}$ and $STR_{k+\frac{1}{2}}$ include contributions of mean and eddy vortex stretching tendency for the interface above and below the layer, respectively. $DISS$ represents the lateral diffusion of mean vorticity tendency, while $BFRIC$ gives the mean contribution from the bottom friction. The last two terms, $CURL$ and $TOPO$, give the contribution to the vorticity balances from the external forcing and the topographic vortex stretching tendency. In a statistically steady state, the term on the left side of (3.22) should vanish provided that the time–averaging is done over a sufficiently long period.

4. Benchmark Experiment

A sequence of experiments has been conducted with the model described in the preceeding chapter. These are summarized in Table 1. For most of the experiments, the wind forcing is a steady, climatological (i.e., mean annual) wind stress curl field (Fig. 10), derived from the Hellerman and Rosenstein (1983) normal monthly wind stress data. This curl field has a maximum near 56°N and the zero contour, separating regions of cyclonic and anticyclonic forcing, has an approximately zonal orientation along 45°N. The map projection discussed in section 3.3 was employed to identify a wind stress curl value to each point in the domain.

Experiment	Friction	Topography	Forcing	Comment
MT	Laplacian, ($200\ m^2\ s^{-1}$)	Variable	Steady	Reference case
MF		Flat		
MT–FS				Free–slip coast
ST			Seasonal	
SF		Flat	Seasonal	
MT–BH	Biharmonic, ($-2 \times 10^{10}\ m^4\ s^{-1}$)			
MT–SL				Weak sponge layer
MT–ST		Variable, Smoothed		
QGBOX1		Flat		Box model, 20 km grid
QGBOX2		Flat		Box model, 10 km grid

Table I. List of numerical experiments. A blank entry indicates the parameter is the same as in experiment MT.

The bottom friction coefficient was set to the value of $1 \times 10^{-7}\ s^{-1}$ (e.g. Holland 1978) for all the experiments, while those experiments with Laplacian friction (p=4) have the lateral viscosity set to a value of 200 m^2 s^{-1}. To obtain turbulent flow, it is necessary to have a low value for this coefficient. A useful criterion for selecting it is to require that the frictional boundary layer be resolved by the grid. Based on the value given above, the scale of the Munk boundary layer, $\delta_M = (\frac{A_H}{\beta})^{\frac{1}{3}}$, is 25 km. Thus the grid (barely) resolves this boundary layer. An experiment (not described in this thesis) similar to MT, but with $A_H = 100\ \mathrm{m^2\ s^{-1}}$, gave a noisy relative vorticity field near the western boundary. However, with $A_H = 200\,\mathrm{m^2\ s^{-1}}$, this noise is greatly reduced.

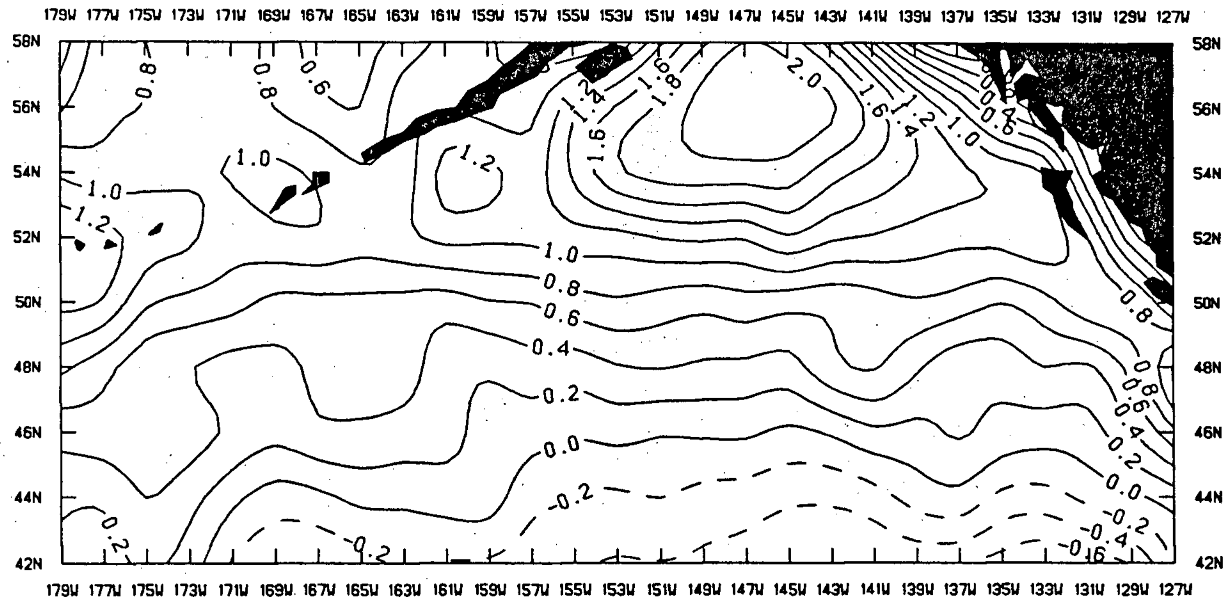

Figure 10. Climatological annual mean wind stress curl over the NE Pacific Ocean computed from the data of Hellerman and Rosenstein (1983). The contour interval is 0.2×10^{-7} N m^{-3}.

In this chapter, a detailed description of a benchmark experiment (MT) is presented while subsequent chapters give the results from additional experiments in which the basic set of parameters used in MT are varied. The emphasis here will be on a comparison of the numerical simulation from MT with the available observations from the Gulf of Alaska. To maintain a certain realism, the bottom topography (Fig. 8) is included. A discussion of the influence of the topography on the solution is deferred to the next chapter where a comparison with a flat–bottom experiment is presented.

In the reference experiment, the no–slip condition is adopted along the continental boundary, while the western and southern boundaries are free–slip. This seems to be a physically reasonable choice since there should be no boundary–generated vorticity at the mid–ocean boundaries, but it is expected that vorticity should diffuse into the ocean interior from the continental boundary (Stewart, 1989). One experiment (MT–FS) was run with a free–slip coastal boundary to assess the influence of this boundary condition. Except in the boundary current region, the solution was not greatly different from that with no–slip. Some of the effects that the no–slip condition introduces to the boundary current are discussed in this chapter, but no further description of the free–slip calculation is given.

4.1 Results

For the reference experiment, the model was integrated from an initial rest state until a state of statistical equilibrium was achieved. The model was then integrated for an additional ten years (with 1 year=360 days) of simulated time during which the streamfunction fields were stored on magnetic tape at 4–day intervals. The time history of the basin–integrated kinetic and potential energies per unit area for this latter period shows that these quantities fluctuate around a well–defined mean that is characteristic of the equilibrium state (Fig. 11). In this figure, the highly baroclinic nature of the model response is indicated. The potential energies of the interfaces are about 40 times the kinetic energies of the overlying layers. In addition, the kinetic energy associated with the bottom layer is very weak.

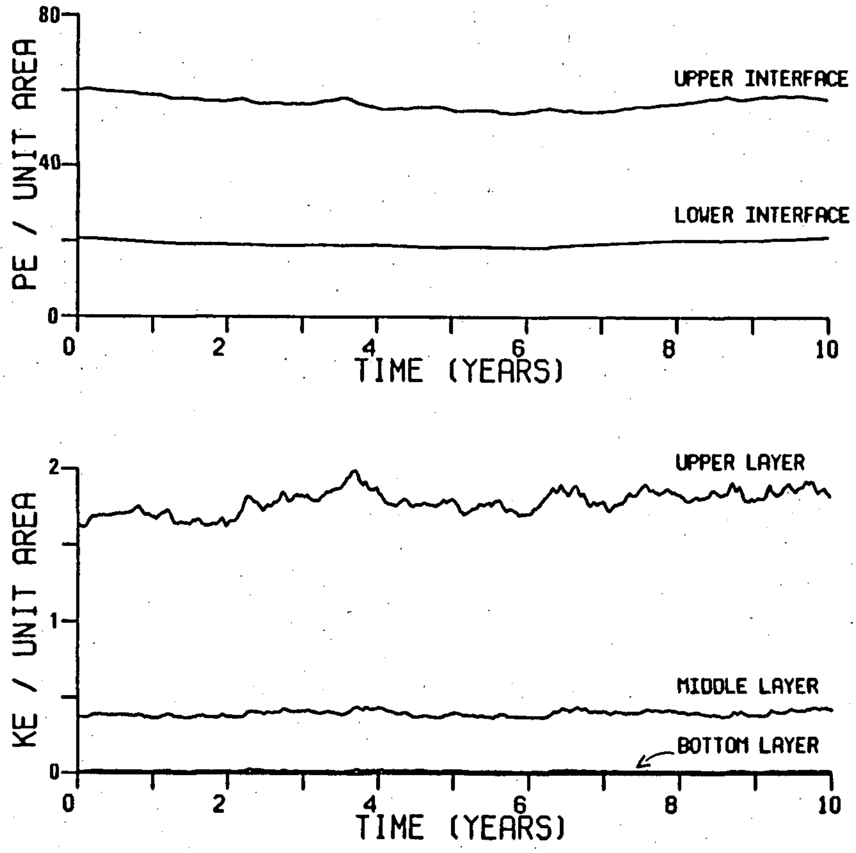

Figure 11. Time–series of the basin–integrated kinetic and potential energies per unit area, for the ten–year duration of experiment MT. Units are 10^3 J m^{-2}.

4.1.1 Instantaneous fields

Examples of the streamfunction field from each of the three layers are shown in Figs. 12a–c. These snapshots were taken from Day 2900 (8.05 y) of the ten–year run. Several features present in these instantaneous fields are characteristic of the entire numerical experiment. The top layer flow is considered first; however the middle layer has a very similar instantaneous pattern of motion so that much of the discussion also applies to this layer. The lowest layer has an entirely different pattern of motion, and a discussion of it is momentarily deferred.

A cyclonic circulation is established in the top layer of the domain. It is composed of several regions of distinct flows, some of which have a correspondence to those observed in the NE Pacific. On the eastern side of the domain, a sluggish northward flowing current is evident that corresponds to the Alaska Current. The model Alaska Current meanders slowly but incessantly and occasionally it breaks off into closed streamline eddies. As the head of the Gulf is approached, the model Alaska Current feeds into an intense southwestward flowing boundary current which corresponds to the Alaskan Stream shown in Fig. 2. Maximum velocities in this current reach 60–70 cm s^{-1}. The model Alaskan Stream flows continuously from the head of the Gulf out to the sponge layer and the artificial western boundary of the domain. The instantaneous width of the model Stream is about 100 km which agrees well with the estimate given by Royer (1981) from observations. South of the boundary current, there is a region of recirculating flow of moderate intensity with particle velocities of about 10–15 cm s^{-1}. This recirculating flow progressively increases the volume transport of the model Alaskan Stream with distance downstream.

In this regional model, there are return flows adjacent to the artificial western and southern boundaries that are not in any way realistic. Nevertheless, the behaviour of the circulation in these regions is of some interest. Along the western wall, the sponge layer seems effective at stabilizing the flow so that it may rejoin the interior without breaking up into eddies. This occurs in two ways: first, as a recirculation in the northwest corner, and second, as a boundary current along the south wall, which eventually feeds into the model Alaska Current. Adjacent to the southern boundary there is a region extending northward about 200–300 km where an adjustment takes place before the wind stress curl begins to drive the circulation to the northeast. This adjustment region may be an artifact of the presence of the southern boundary, in which case it would probably not appear in a larger model.

The circulation in the bottom layer (Fig. 12c) is in great contrast to that of the two overlying layers. The well–organized circulation pattern found above is absent; instead the abyssal flow is very weak and consists primarily of numerous eddies of

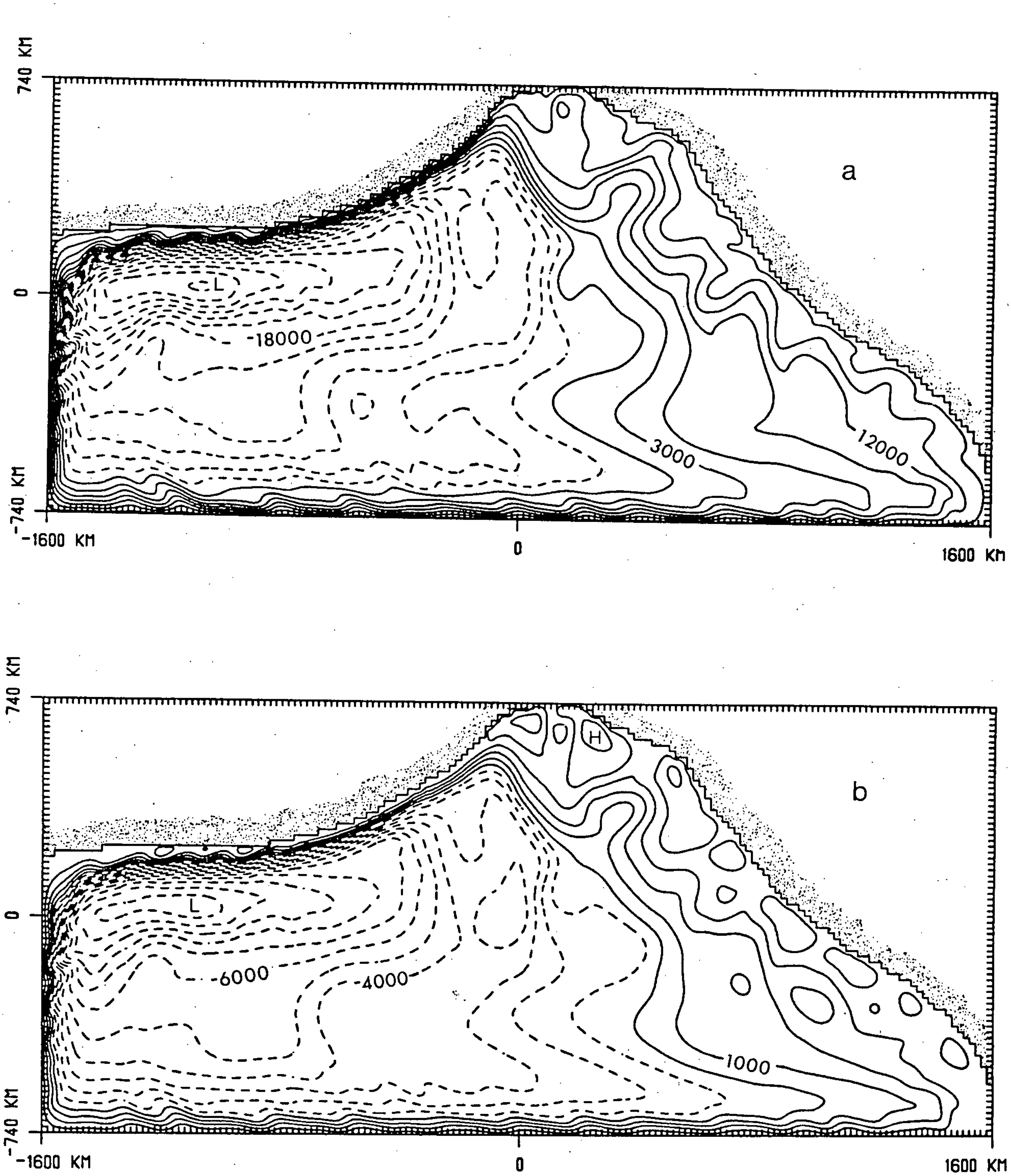

Figure 12. The instantaneous streamfunction fields on Day 2900 for (a) the top layer (CI=3000 m^2 s^{-1}), (b) the middle layer (CI=1000 m^2 s^{-1}), (c) the bottom layer (CI=75 m^2 s^{-1}). Solid lines are drawn for positive contour values while dashed lines are drawn for negative contours.

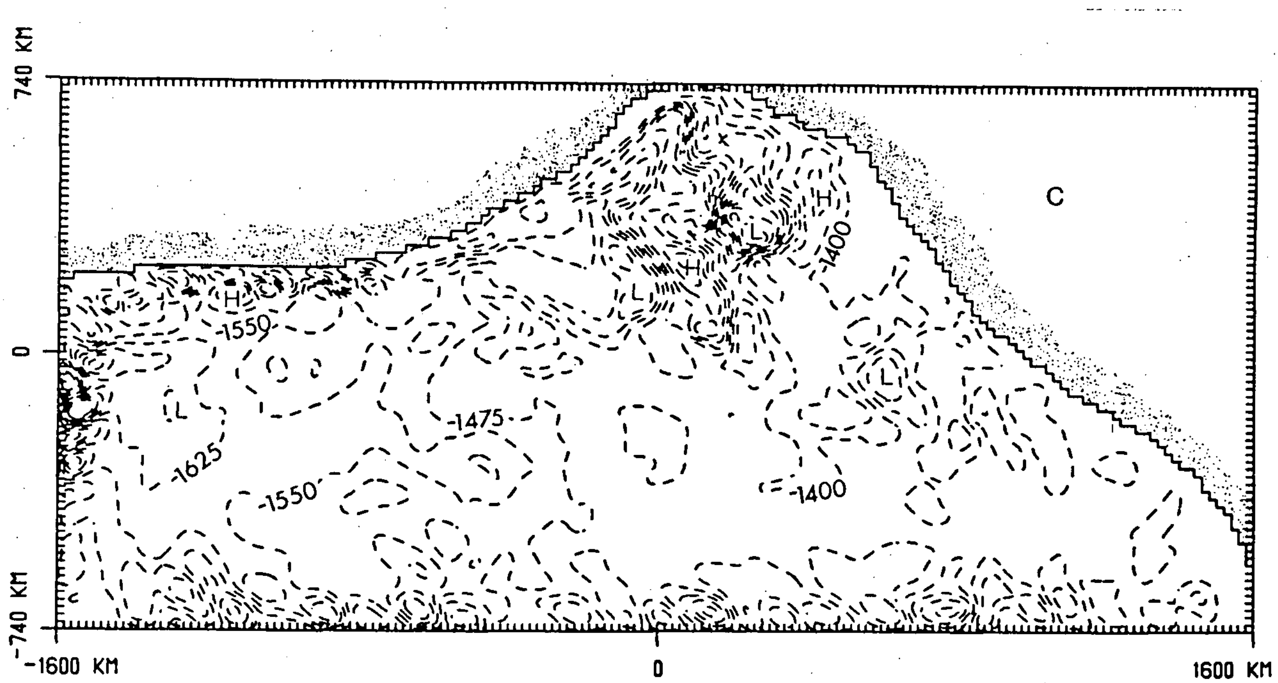

Figure 12 continued.

both cyclonic and anticyclonic rotation, mostly concentrated in the northern half of the domain. The scale of these eddies is clearly related to the bottom roughness. In the boundary current region, the eddy length scale is comparable to the width of the Aleutian Trench. In the vicinity of large seamounts, the eddies assume the scale and even, to some extent, the shape of the seamounts. The reason for the very different circulation pattern of the bottom layer lies in the attenuation of the barotropic mode of motion by the topography. This will be the subject of further discussion in Chapter 5.

Two sequences of the top layer streamfunction are given in Figs. 13a–c and 14a–d to illustrate the transient motions associated with eddy variability in the model.

The first sequence, with an 80 day interval between snapshots, shows an episode of anticyclonic ring generation from a meander in the Alaska Current near the head of the Gulf. The meander originally appeared as a small perturbation to the southeast in the Alaska Current. On a time scale of about 250 days, it grew in amplitude and moved to the northwest before pinching off into a ring on Day 1120. The ring persisted as an identifiable structure for the next 360 days. Over this time period, it propagated to the west at a speed of about 1 km day^{-1} and, in the process, slowly diminished in size and intensity.

Ring generation, as illustrated above, is largely confined to the Alaska Current and, even there, occurs rather infrequently. The large amplitude meandering of the model Alaska Current often produces regions of cyclonic and anticyclonic curvature in the flow, particularly near the head of the Gulf. However, over the course of the ten-year experiment only a small number (4) of these meanders actually pinched off to form (anticyclonic) rings.

It is tempting at this point to identify the anticyclonic ring of Figs. 13a–c as a model Sitka Eddy; the comparison holds in some respects. The model eddy is highly baroclinic, appears in approximately the correct location, and is of the correct rotation and horizontal scale ($\sim$ 200 km initially). In addition, it is a long-lived feature that moves westward in a manner consistent with the few observations. Some discrepancy does exist in the comparison: the model eddy, with a transport of about 2 Sv, is weaker than those typically observed. This may be due to the horizontal friction which is likely too large and therefore prevents the development of eddies with sufficient intensity at the head of the Gulf. As illustrated in section 7.1, lateral friction also has an influence on the frequency of eddy production in the model Alaska Current.

If the suggestion given above is correct, then it would then appear that the formation of the Sitka Eddy is due to a baroclinic instability of the Alaska Current.

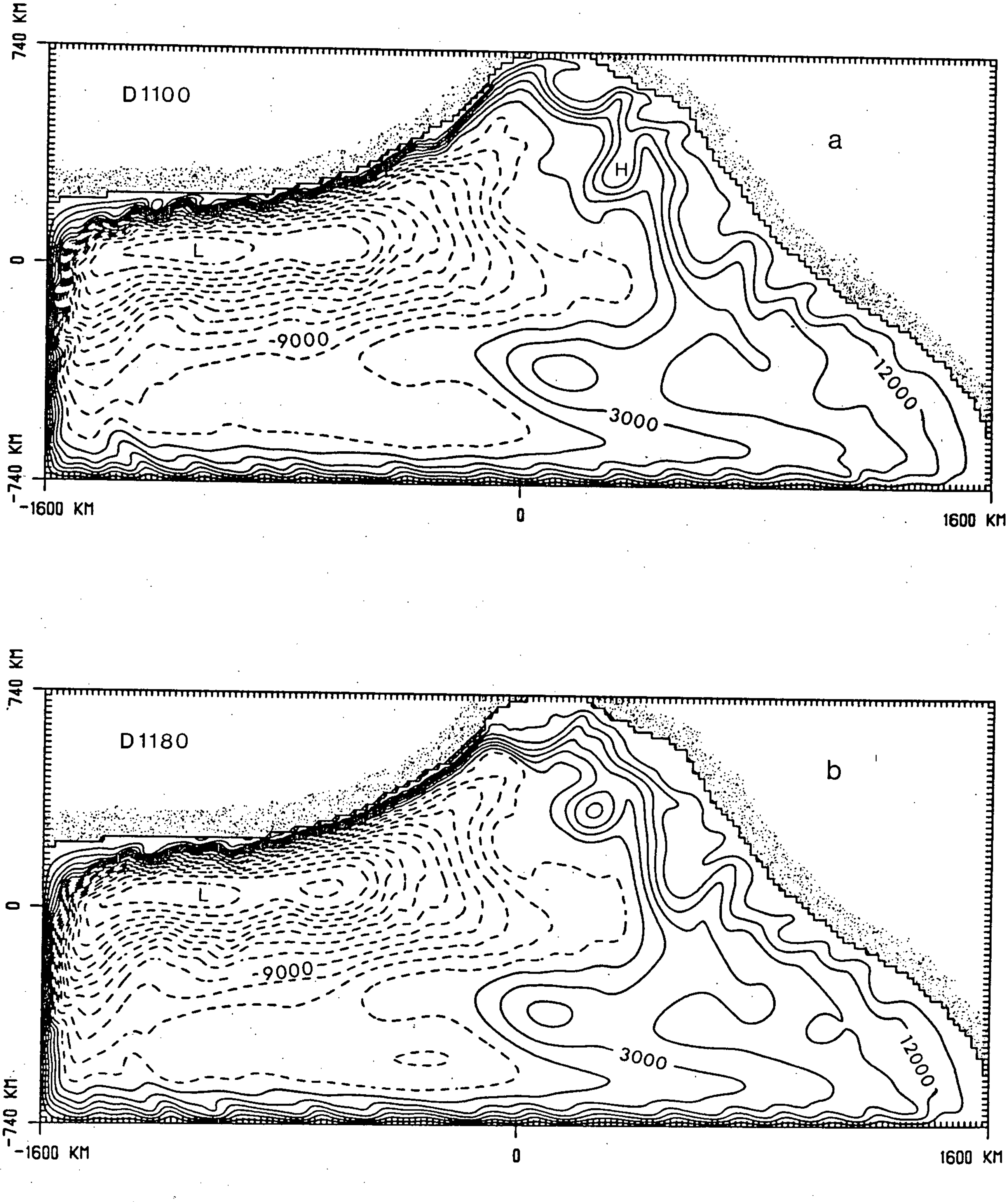

Figure 13. A time–sequence of the top layer streamfunction field at 80–day intervals beginning on Day 1100 (CI=3000 $m^2\ s^{-1}$)

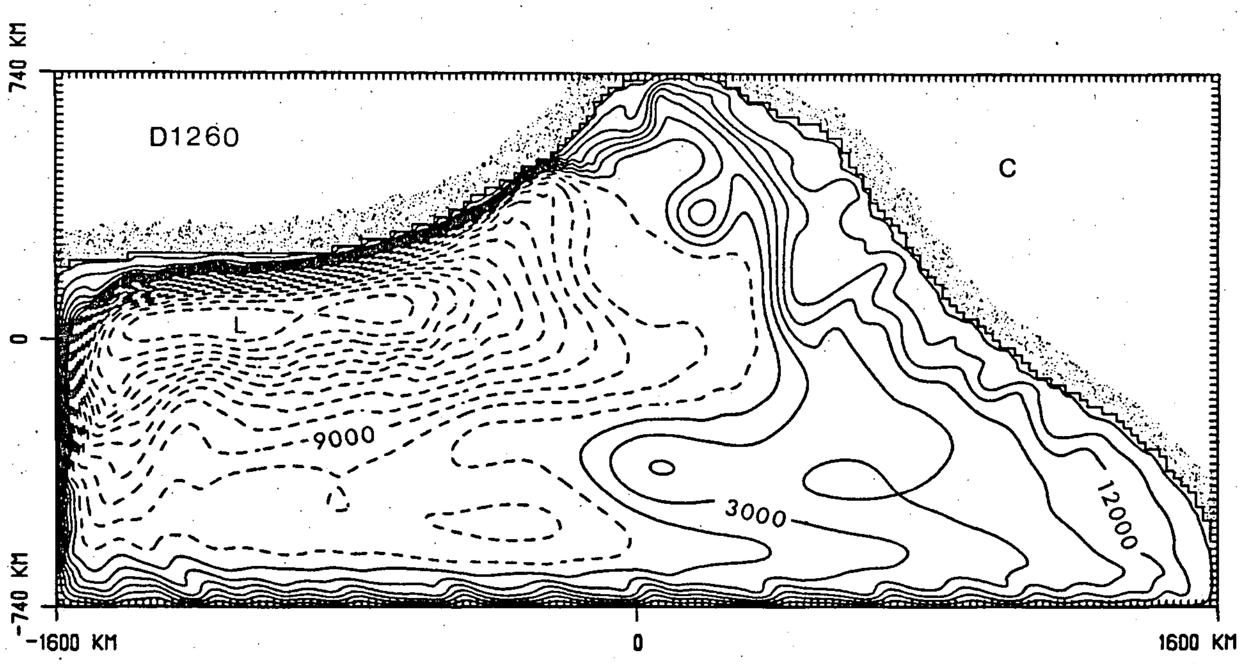

Figure 13 continued.

(As discussed below, this is the dominant form of instability over interior regions of the domain.) The theory, given by Willmott and Mysak (1980), in which the generation of the Sitka Eddy is dependent upon very low frequency oscillations of the wind field may well be superfluous. Swaters and Mysak (1985) showed that the local bottom topography could have an important role in the generation of the Sitka eddy. Further experimentation is required to assess the influence of topography on the generation of eddies in the model Alaska Current.

Figs. 14a–d are included to illustrate the characteristic variability of the model Alaskan Stream. This current is typically a parallel flow lying adjacent to the sloping boundary. However, throughout the course of the experiment, the model Stream is subject to aperiodic meandering, which produces localized regions of anticyclonic curvature in the flow. These meanders are perturbations that originate near the head of the Gulf and propagate downstream at a speed of about 2 km day^{-1} causing a lateral displacement of the current axis that may exceed 200 km. The sequence illustrated in Fig. 14 is a particularly large amplitude event of this type. The amplitude of these perturbations decreases with distance downstream, and rarely do they reach the region off the Aleutian Islands where the boundary is zonal. Since only anticyclonic meanders occur, and these never break off to form rings, the model Stream remains a continuous, albeit laterally displaced, current.

As discussed in Chapter 2, there is evidence to suggest that the large amplitude meandering observed in the model boundary current also occurs in the Alaskan Stream. A very similar structure is found in the AVHRR image of Fig. 4. Reed et al. (1980) and Reed and Schumacher (1984) also noticed that the Stream was subject to aperiodic, vertically coherent, lateral meandering. Their observations indicated that these perturbations propagated downstream, but a phase speed was not given.

Further downstream and offshore from the zonal boundary, the separated model Stream undergoes smaller amplitude (40–60 km) lateral motions. In contrast to the episodic variability found farther upstream, the meandering here is quasi–periodic and of high frequency (~ 0.08 cycles day^{-1}). These perturbations are not traceable back to the head of the Gulf but appear to originate locally. In contrast to these results, the boundary current in the solution from MT–FS was virtually unperturbed over the course of a 10–year integration.

4.1.2 Mean fields

Mean streamfunction fields, computed according to (3.20), are shown in Figs. 15a–c. As is characteristic of this experiment, the mean flows in the upper two layers are generally very close in pattern but are intensified in the top layer. Some

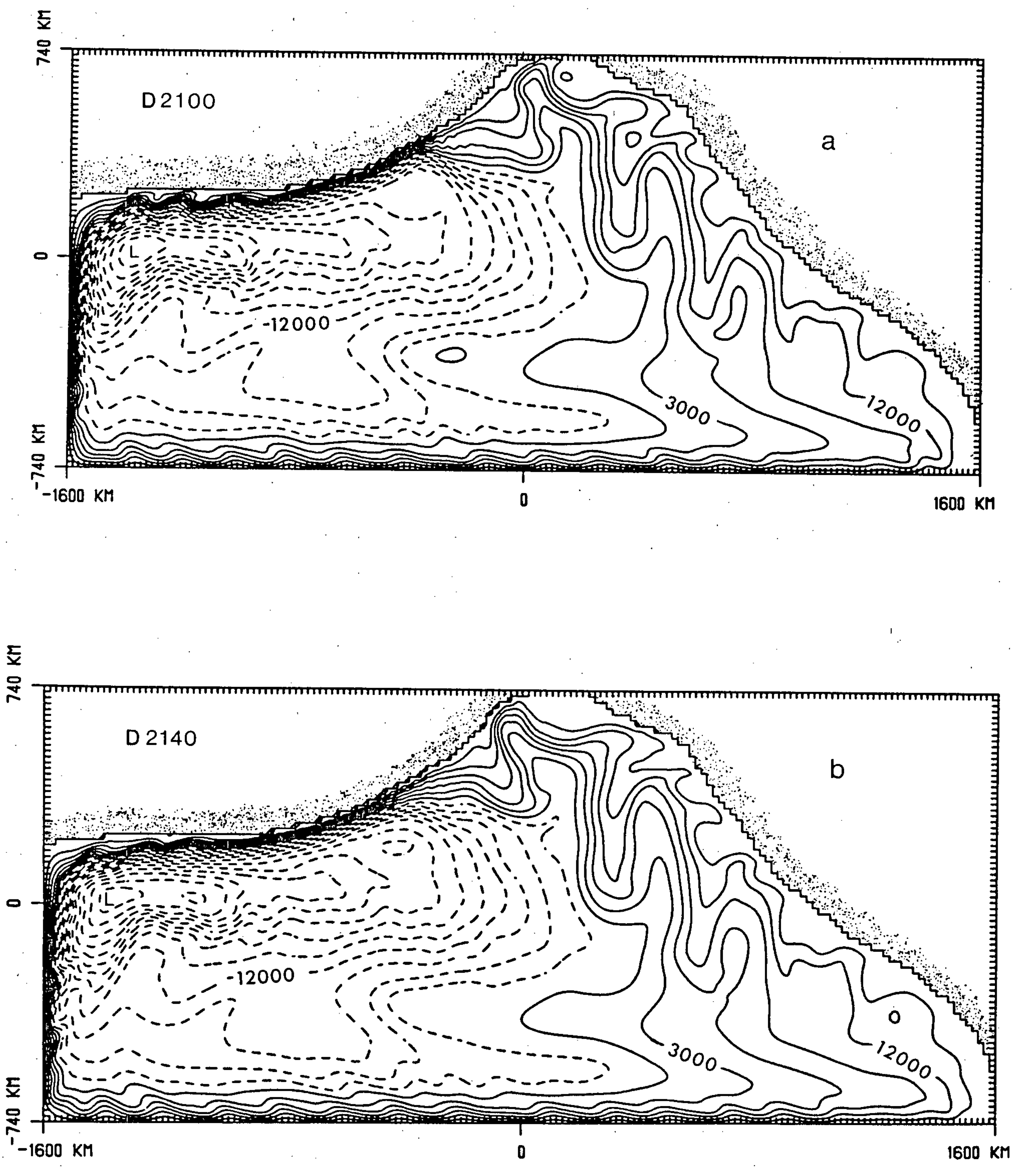

Figure 14. A time-sequence of the top layer streamfunction field at 40-day intervals beginning on Day 2100 (CI=3000 $m^2\ s^{-1}$)

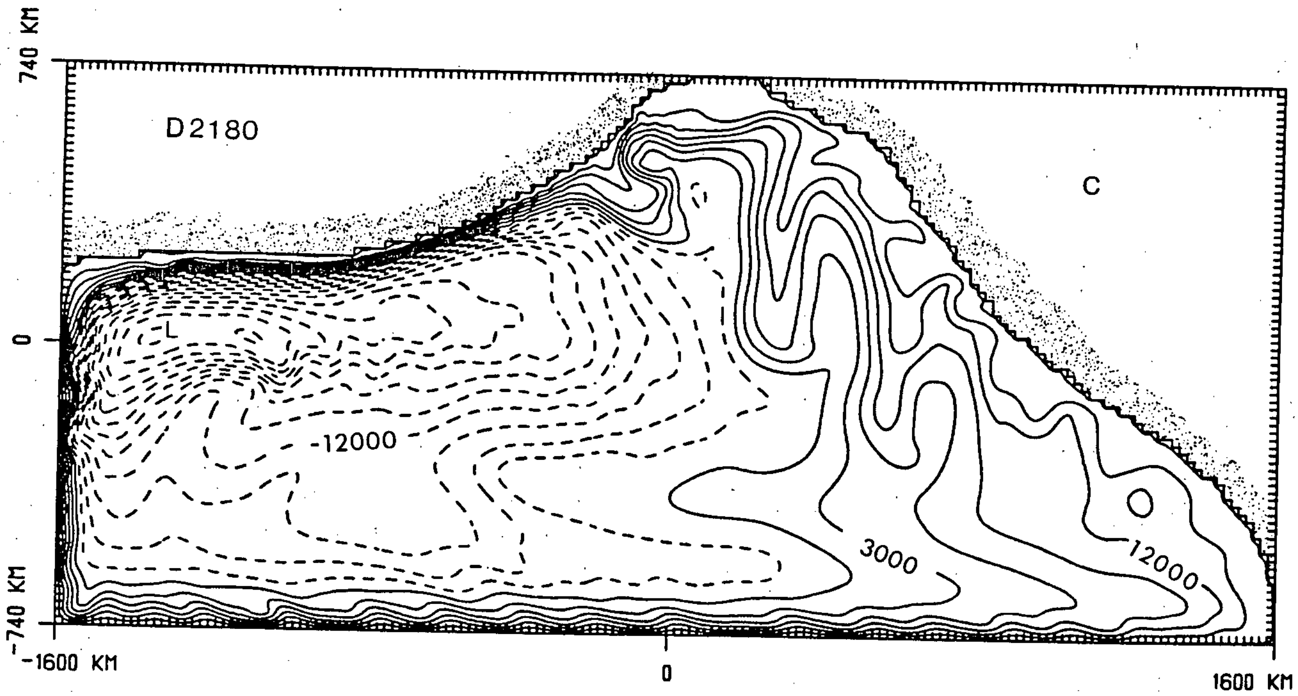

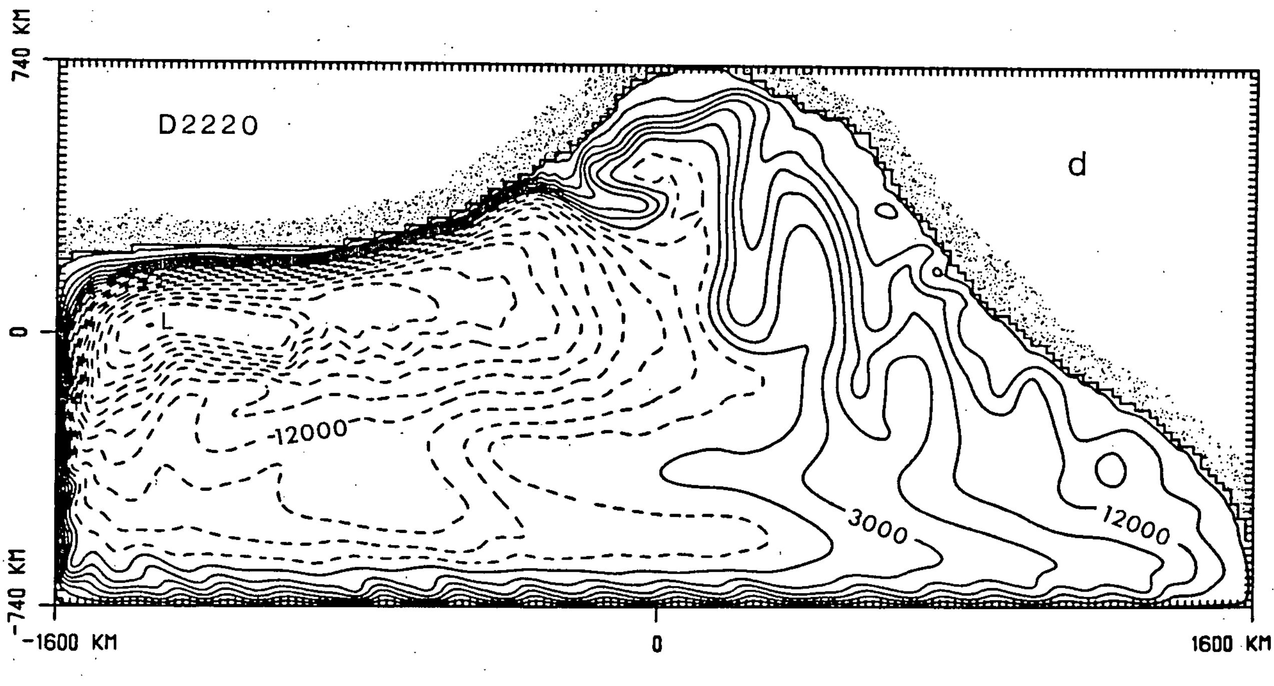

Figure 14 continued.

difference is found in the circulation pattern of these two layers near the northeastern boundary. The bottom layer shows only very weak mean flows. It contains a broad eastern interior region with virtually no mean motion.

The mean gyres include a broad weak Alaska Current which funnels near the head of the Gulf into the model Alaskan Stream. In the model Alaska Current, mean velocities in the top layer are weak, ranging from 2 to 5 cm s^{-1} with larger values near the head of the Gulf. The flow velocity in the model Stream increases in magnitude with distance downstream, while becoming less baroclinic. Mean particle velocities increase downstream from the Mean particle speeds range from 35 (9) cm s^{-1} off Kodiak Island to 55 (15) cm s^{-1} off the Aleutian Islands for the top (middle) layer. The current measurements of Reed and Schumacher (1984) provide a point of comparison with the computed values. They obtained 10 month mean speeds of 24 (19) cm s^{-1} at 300 (500) m depth. The model values at these depths are 22 and 9 cm s^{-1}, which suggests that the mean flow speed in the top layer of the model is approximately correct while that of the middle layer is somewhat low.

The mean horizontal scale of the western boundary current is about 100 km off Kodiak Island and increases downstream due to recirculation of flow along its southern flank. Separation of the mean boundary current occurs as the boundary becomes zonally oriented. It is notable that the mean boundary current separates from the boundary at the point where the deep isobaths also diverge away from the boundary (Fig. 8).

The model transport between Station P and the coast is about 5.7 Sv and is almost entirely confined to the two uppermost layers. This value is approximately equal to the transport computed from the Sverdrup relation using the wind stress curl forcing. For comparison, the observed 0/1000 db baroclinic transport across Line P is 5.2 Sv (Tabata, 1989). Using a 1500 db reference level increases the observed transport to 6.9 Sv. Thus the model somewhat underestimates the volume

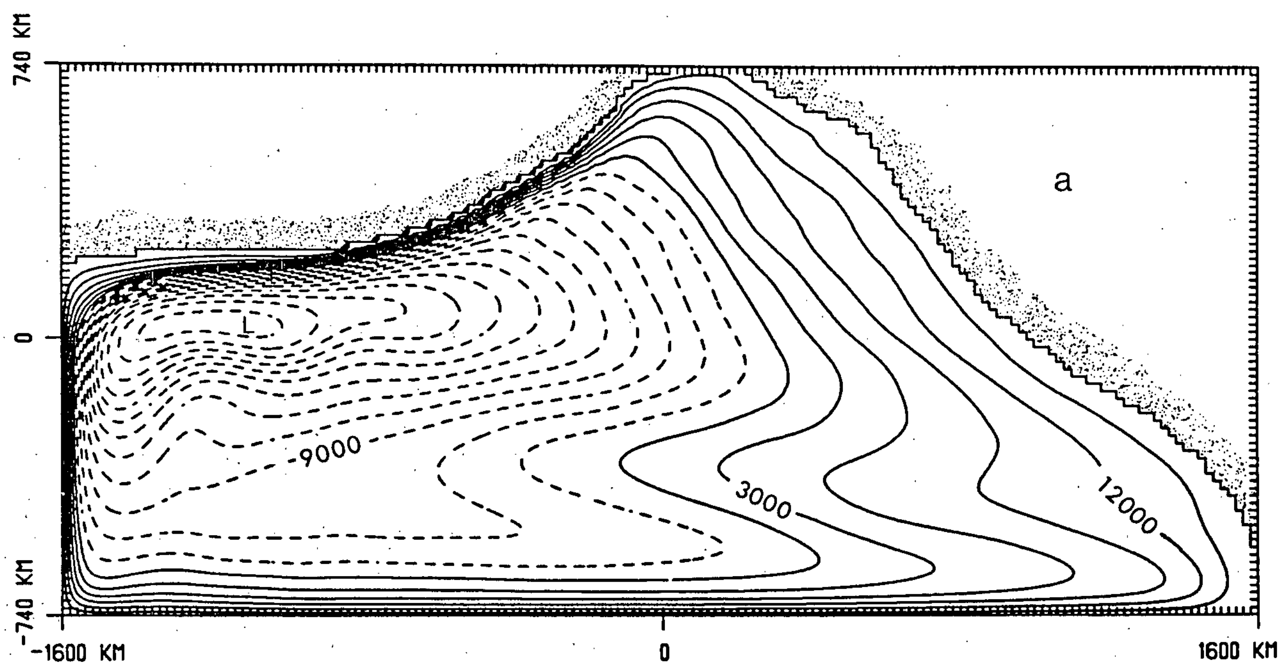

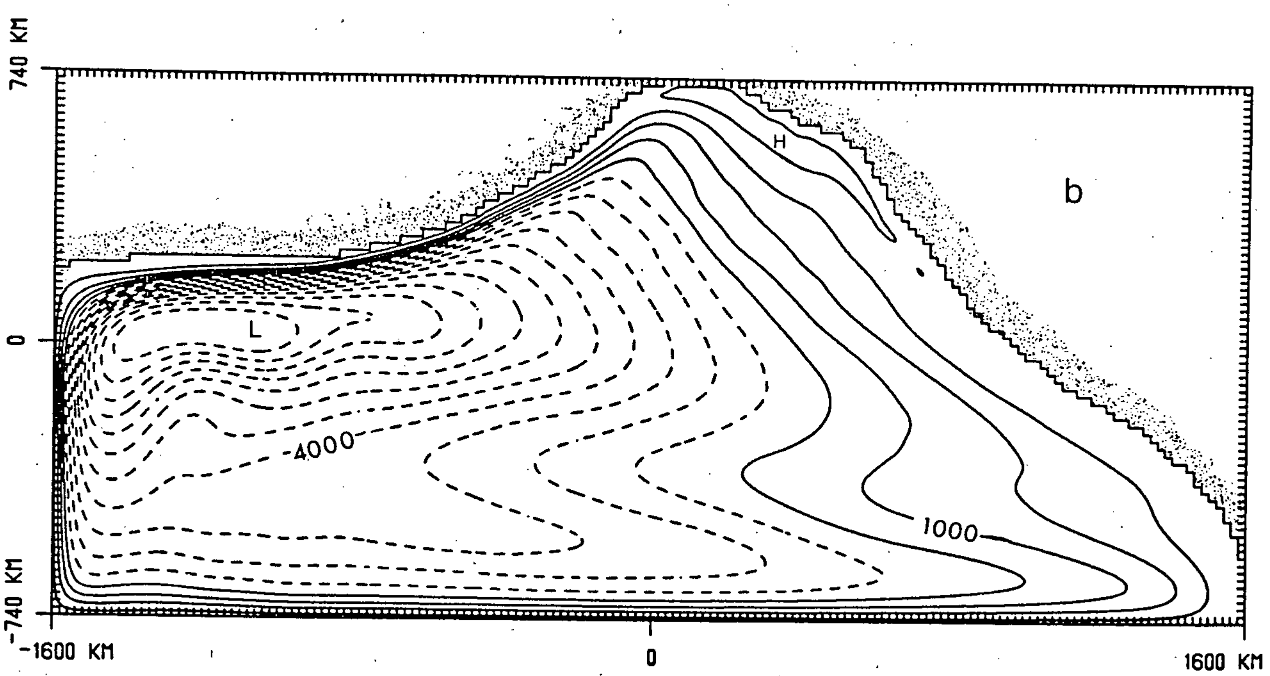

Figure 15. The mean streamfunction fields for (a) the top layer (CI=3000 $m^2\ s^{-1}$), (b) the middle layer (CI=1000 $m^2\ s^{-1}$) and (c) the bottom layer (CI=25 $m^2\ s^{-1}$).

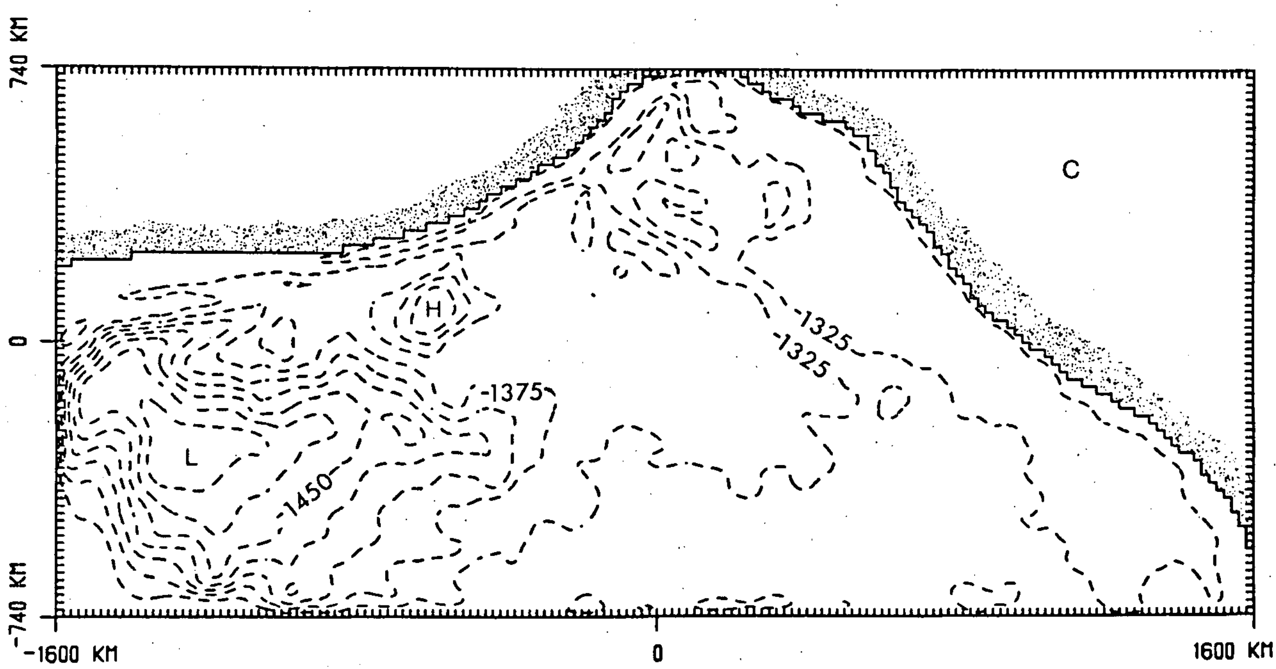

Figure 15 continued.

transport across Line P. This is an indication that the Hellerman and Rosenstein (1983) monthly wind stresses underestimate the true winds over the NE Pacific. The transport comparison also points to the inadequacy of the vertical resolution.

Comparison with transport estimates off Kodiak Island gives essentially the same impression. The model transport between Kodiak Island and 100 km offshore has a value of about 8.0 Sv and again is almost entirely confined to the top two layers. Royer (1981) gives the observed 0/1500 db mean transport of the Alaskan Stream off Kodiak Island as 9.5 Sv. In addition, Reed et al. (1980) found that the use of a 3000 db reference level augmented the Stream transport by as much as 5 Sv. Thus the model Alaskan Stream transport appears to be somewhat low and there is insufficient transport in the bottom layer.

A final transport comparison for the maximum Alaskan Stream transport may be attempted. For the model, this quantity is about 21.1 Sv of which 11.0 Sv and 9.3 Sv are found in the top two layers. Combining hydrographic and current meter data, Warren and Owens (1988) estimated that the Alaskan Stream transports 28 Sv across 175°W. The model transport again appears to be too small, although an extension of the model boundary beyond 175°W would probably make up for some of the discrepancy between the observed and model transports.

Adjacent to the northeastern boundary, the mean streamfunction field in the middle layer (Fig. 15b) has a weak anticyclonic circulation. Associated with this is a mean southeastward flowing current, which transports a maximum of 0.5 Sv. This feature arises, in a mean sense, from time–averaging the anticyclonic eddies, which appear continuously at the eastern margin of the basin in the middle layer (Fig. 12b). The parallel experiment with a free–slip boundary condition showed the same anticyclonic structure near the eastern boundary.

The mean potential vorticity fields are fundamental to the quasi–geostrophic model and they place an important constraint upon the fluid motion. In the absence of eddies and nonconservative effects (external forcing and dissipation) the flow must follow the mean potential vorticity contours. In the lowest layer, the topographic term is the dominant vorticity term of the mean potential vorticity, $\overline{Q_3}$. In this case, the spatial pattern of the field looks much like the topography of Fig. 8. In the top layer, $\overline{Q_1}$ is determined mainly by the interfacial displacement. It has a horizontal distribution which is very similar to the streamfunction field of Fig. 15a. This pattern is consistent with the observed spatial distribution of potential vorticity on upper–ocean isopycnal surfaces in the subpolar gyre (Talley, 1988).

The two interfacial displacement terms in (3.7) are also dominant for the mean potential vorticity field of the middle layer, $\overline{Q_2}$, which is contoured in Fig. 16. There is a region of weak potential vorticity gradients found in the southeastern part of the domain. This is suggestive of the process of vorticity 'homogenization' proposed by Rhines and Young (1982) and verified in the quasi-geostrophic model of Holland et. al. (1984).

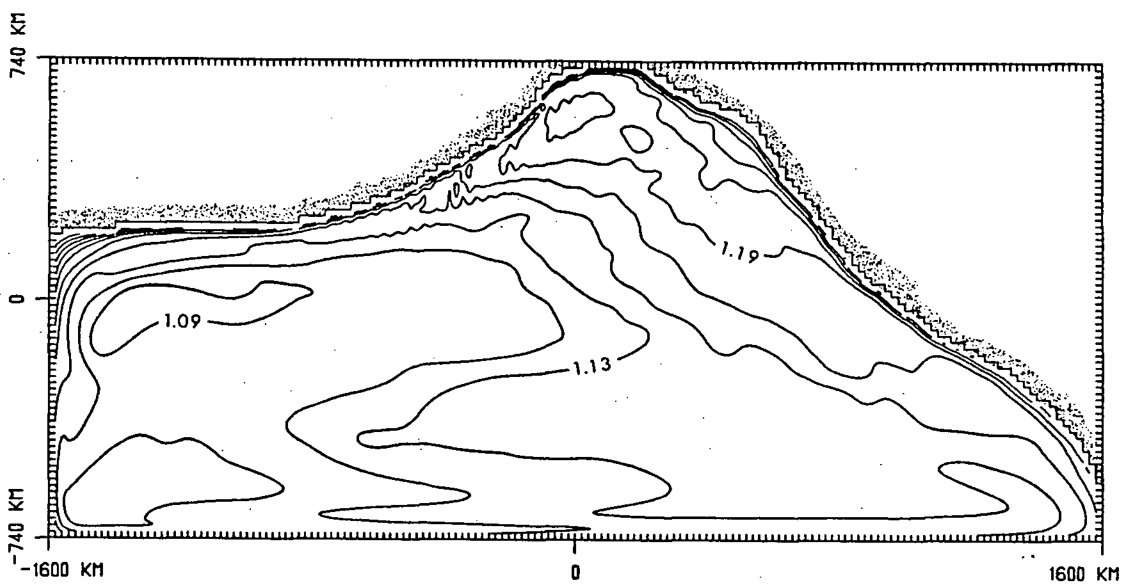

Figure 16. The mean potential vorticity field of the middle layer, $\overline{Q_2}$ (CI=2×10^{-6} s^{-1}).

McWilliams (1977) showed that a necessary condition for instability of the mean flow of a layer model is that

$$\frac{\partial \overline{\psi}_k}{\partial \overline{Q}_k} < 0 \qquad \text{for any} \quad k. \tag{4.1}$$

The scatter diagrams of Figs. 17a–b show the relationship between the streamfunction and potential vorticity fields for the top and middle layers of the model. For the top layer, the necessary condition for instability is clearly met, over the entire domain. For the middle layer, the scatter diagram shows that the necessary condition for instability does not hold in a systematic fashion. There are nevertheless localized regions in which (4.1) holds in the middle layer. For example, the condition must hold at some point within the closed contours of $\overline{Q_2}$ found at the head of the Gulf (Fig. 16).

The relatively tight linear relation between $\overline{\psi}_1$ and $\overline{Q}_1$ in Fig. 17a suggests that $\overline{Q_1} = \overline{Q_1}(\overline{\psi_1})$ and that the model solution can be approximately characterized by

$$J(\overline{\psi_1}, \overline{Q_1}) = 0. \tag{4.2}$$

Despite the presence of nonconservative effects and eddies, the mean solution for the top layer approximates the free advection of potential vorticity. The modest scatter about a unique relationship between $\overline{\psi_1}$ and $\overline{Q_1}$ indicates that (4.2) is not an exact description of the solution. Fig. 17b and a similar diagram for the bottom layer indicate that a relation of the form of (4.2) is not valid for the middle obottom layers.

4.1.3 Eddy Fields

The eddy kinetic energy (EKE) fields are shown in Figs. 18a–c. For each layer the EKE is always largest in the model Alaskan Stream region and much weaker over the interior of the domain. The transition from the quiescent interior to the eddy intense regions of the Stream is gradual near the head of the Gulf but very sharp further downstream. Within the Alaskan Stream the EKE field has a maximum off the Aleutians Islands that is associated with high frequency lateral meandering of the current. This maximum is absent in the experiment with a free–slip coastal boundary (MT–FS). The EKE field at the head of the Gulf, away from the western boundary, reflects the eddy energy associated with low frequency meandering of the Alaskan Current.

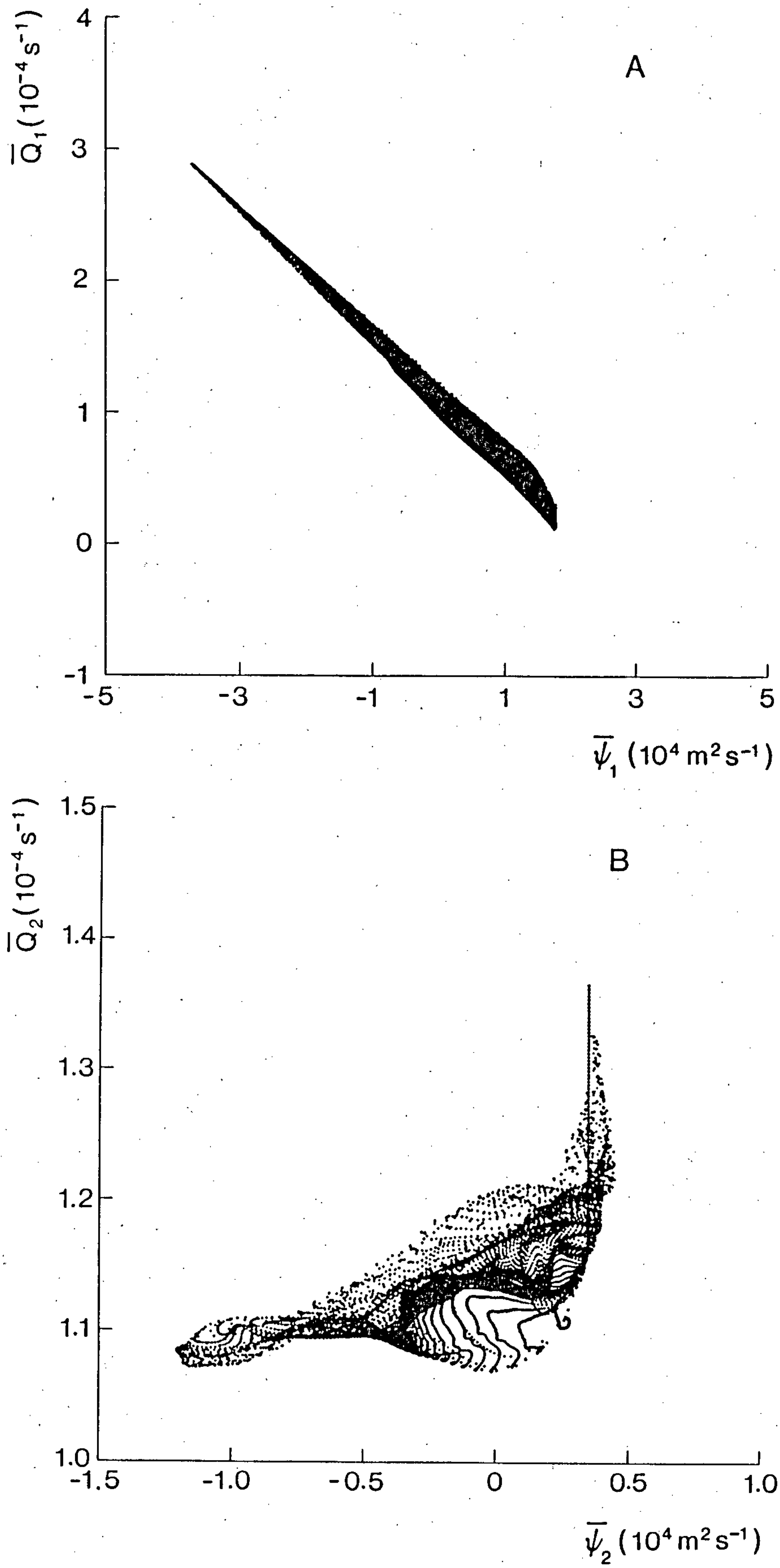

Figure 17. Scatter diagrams of mean potential vorticity, $\overline{Q_k}$, plotted against mean streamfunction, $\overline{\psi_k}$, for (a) the top layer and (b) the middle layer.

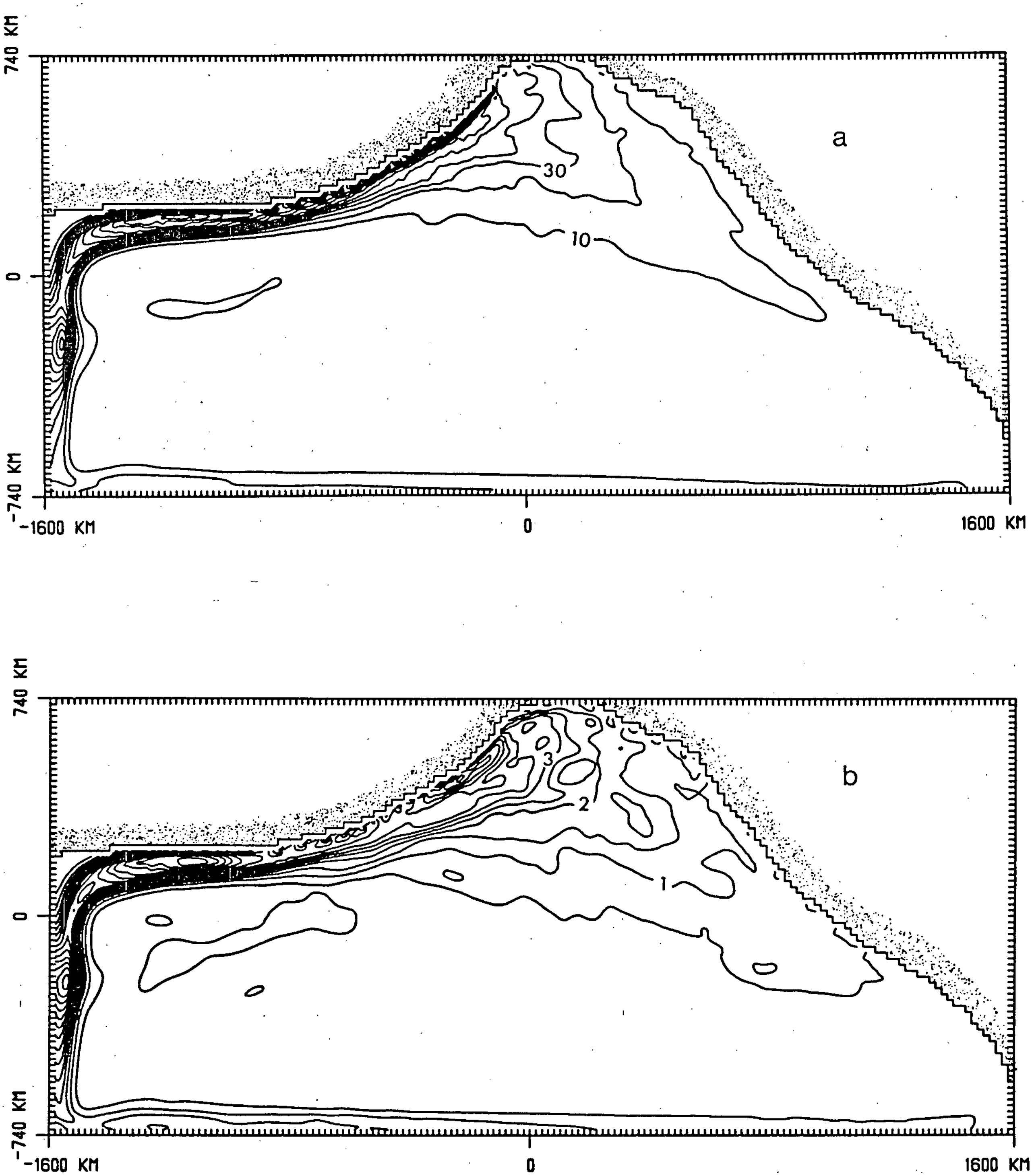

Figure 18. The eddy kinetic energy fields for (a) the top layer (CI=10 $cm^2\ s^{-2}$), (b) the middle layer (CI=0.5 $cm^2\ s^{-2}$), and (c) the bottom layer (CI=0.05 $cm^2\ s^{-2}$).

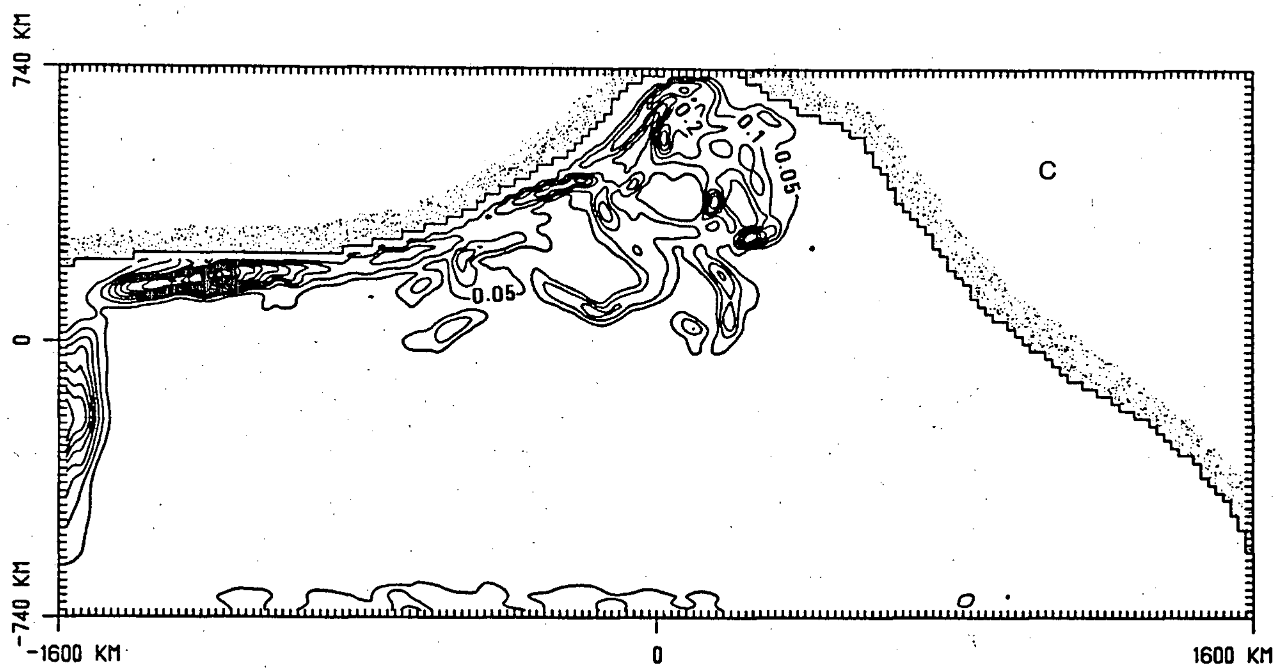

Figure 18 continued.

The ratio of the EKE to the kinetic energy of the mean flow, KE, is a measure of the strength of the variability of the flow relative to the mean. In the lowest layer, with its very weak mean flows, the variability dominates everywhere over the mean, with the EKE/KE ratio ranging from 10–50. For the top layer of the model Alaska Current, this ratio is about 2 and increases to about 3 in the vicinity of the Sitka Eddy region. In the recirculation region farther to the west, the variability is small and the ratio is typically only 0.1–0.2. The western boundary current region is also characterized by comparatively small variability of the flow. Downstream, in the separated current off the Aleutian Islands, the ratio is only about 0.1. Further upstream, where the current is bounded by a sidewall, the EKE/KE ratio increases to 0.2.

These results are, for the most part, consistent with the observations of Reed and Schumacher (1984). They obtained an EKE/KE ratio of 0.4 in the upper layers of the Alaskan Stream off Kodiak Island while the model gives a value of 0.2. The magnitude of the observed EKE at 300 m depth was about 80 $cm^2\ s^{-2}$ which, as Reed and Schumacher suggest, is quite low in comparison to other western boundary currents. Measurements taken from comparable locations in the Gulf Stream or the Kuroshio Extention indicate both a larger EKE/KE ratio and higher levels of eddy energy. The model gives a EKE of 55 $cm^2\ s^{-2}$ at 300 m depth which indicates that the level of variability, particularly in the middle layer, is somewhat underestimated

.

At this point, a comparison with global estimates of the EKE field is appropriate. Wyrtki et al. (1976) estimated the near-surface EKE field over the world ocean from ship drift data. In the interior of the NE Pacific, they estimated a nominal value of about 400 $cm^2\ s^{-2}$. Subsequent estimates of the EKE field in the NE Pacific (Fu, 1983; Thomson, 1986) have obtained much smaller values of the order of 50 $cm^2\ s^{-2}$. The model results agree much better with the latter estimate. Even in experiment MT–BH (biharmonic friction, section 7.1), the EKE level over the Alaska Current region is several tens of $cm^2\ s^{-2}$, far below the estimate of Wyrtki et al. (1976).

A different view of the eddy variability is obtained from maps of the interfacial eddy potential energy (EPE) as shown in Figs. 19a–b. The predominance of eddy fluctuations in the boundary current region is again evident here; however, the constrast with the interior regions is not as pronounced as for the EKE. While the eddy potential and kinetic energies are roughly comparable in the boundary current (an EPE/EKE ratio of 2–3), the EPE is much greater over a large expanse of the interior. This is consistent with our analyses in Section 4.5 which indicate that baroclinic processes are dominant in accounting for the variability of the model Alaska

Current.

Emery (1983) computed the eddy potential energy from temperature variations at 300 m depth over the entire North Pacific. He obtained very large values (O(1500 cm^2 s^{-2})) in the Gulf of Alaska, which were comparable to those of the Kuroshio Extension. Emery considered this result to be implausible and attributed it to having used temperature rather than salinity (the primary determinant of density in the Gulf) to estimate the EPE. The results presented here tend to confirm this assessment.

4.1.4 Space–time (Hovmöller) Diagrams

Hovmöller diagrams of the top layer streamfunction from two sections of the domain (see Fig. 24) are shown in Figs. 20a–b. The first is a y versus t diagram taken along the N–S line x=360 km, which cuts diagonally across the Alaska Current. It shows northward phase propagation at a rate of 0.5 km day^{-1} for the northern half of the section (y > 200 km). This occurs intermittently – not every year–long record shows northward phase propagation in the Alaska Current.

The second section begins near the head of the Gulf at x=–20 km and follows along the curving western boundary out to x=–1040 km. This diagram discloses the phase propagation along the path of the Alaskan Stream in the top layer. The phase speed increases from about 1 km day^{-1} in the upstream region to about 13 km day^{-1} farther downstream. The change is fairly abrupt and occurs at about 400 km from the upstream end of the section. The adjoining boundary is still sloping at this point and is not yet zonally oriented. In addition, the fluctuations are of much higher frequency past this point. Th bottom layer (not shown) shows similar high frequency fluctuations and phase propagation in the downstream region. In the next section, cross–spectral analysis is employed to interpret this high frequency signal in terms of wave modes.

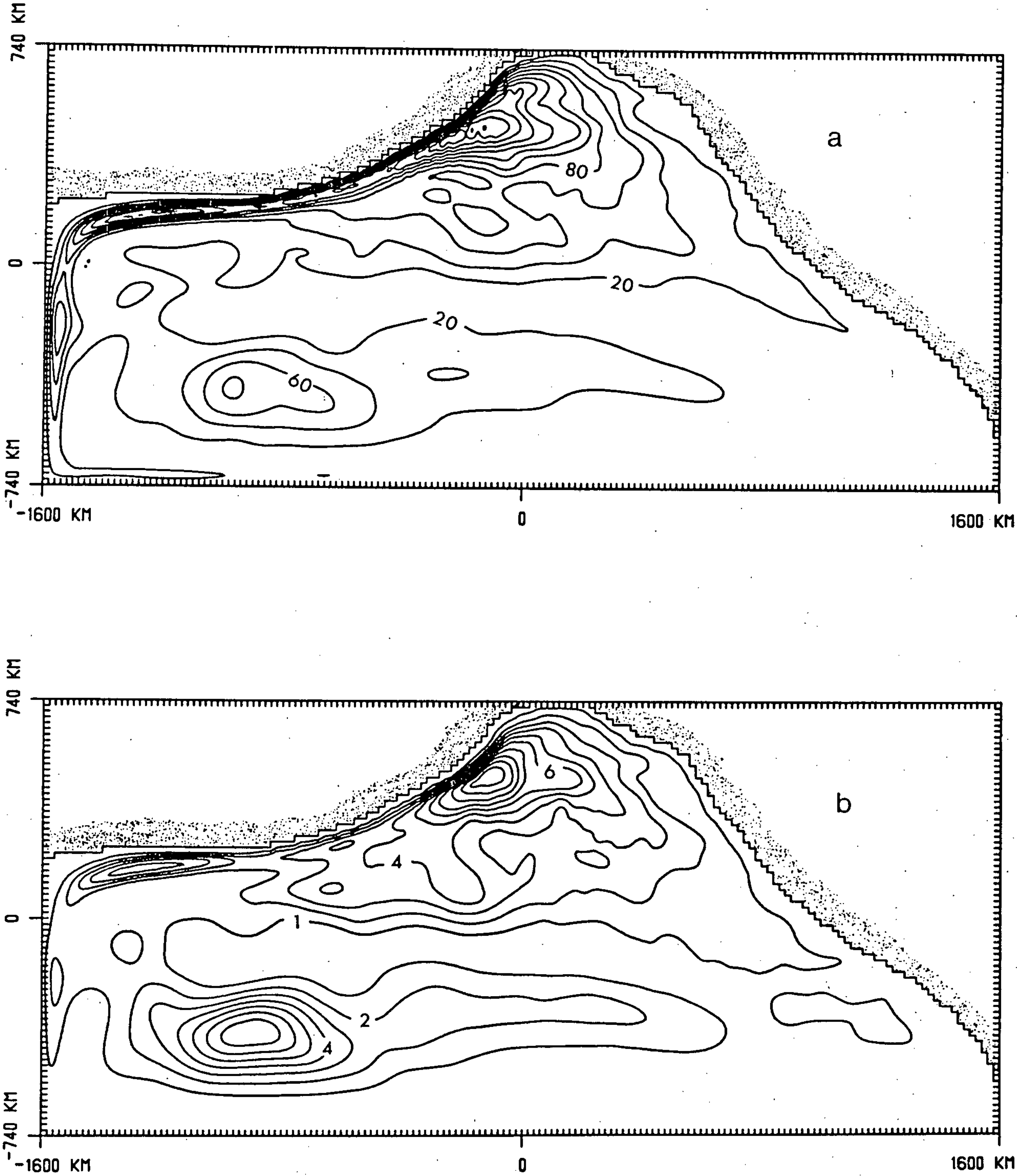

Figure 19. The eddy potential energy fields for (a) the top interface (CI=20 $cm^2\ s^{-2}$) and (b) the bottom interface (CI=1 $cm^2\ s^{-2}$).

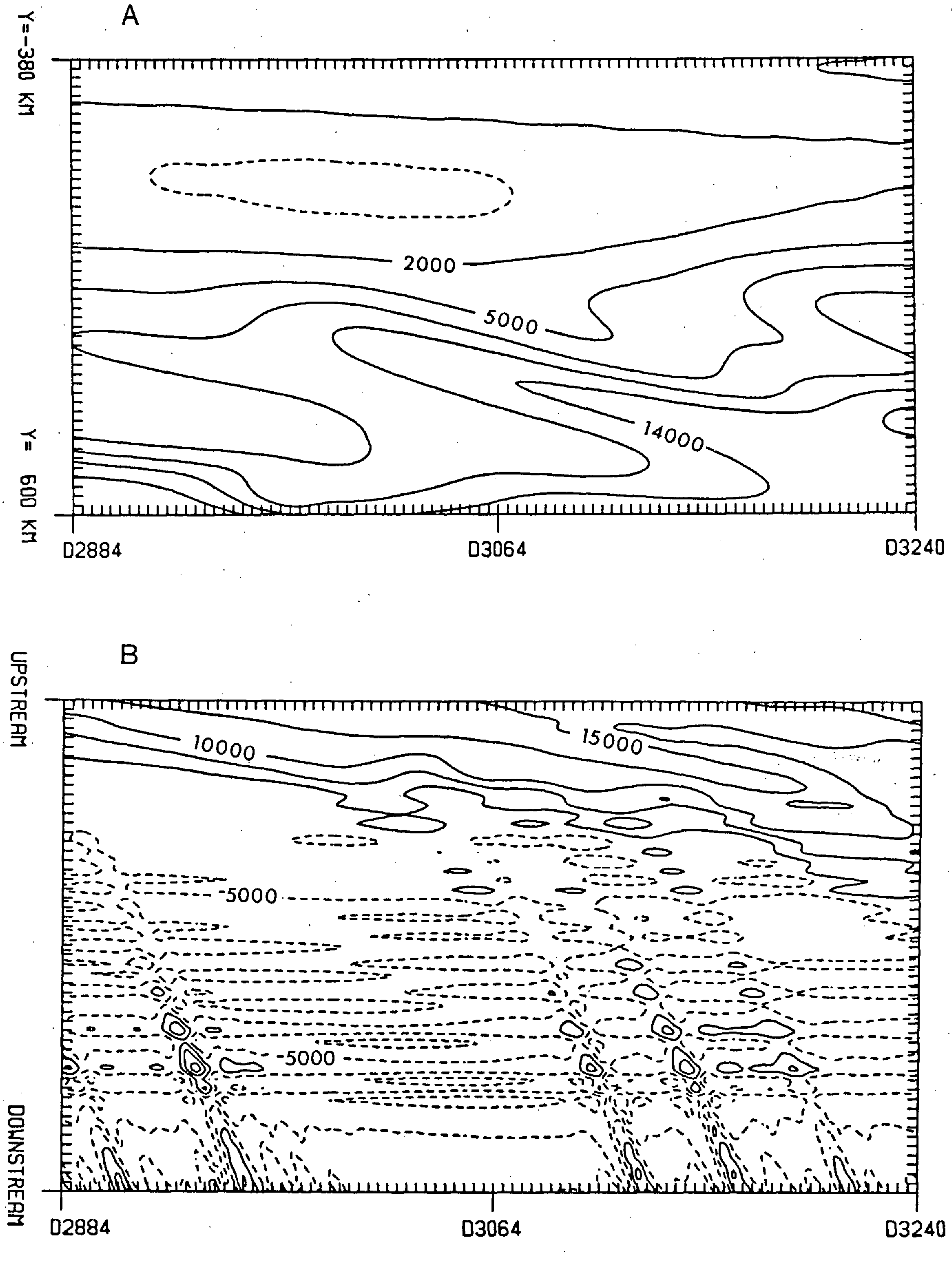

Figure 20. Hovmöller diagrams of the top layer for (a) a section (y vs t) through the Alaska Current region (CI=3000 m^2 s^{-1}) and (b) a section along the Alaskan Stream (CI=5000 m^2 s^{-1}). One year of data from the ninth year of the experiment is shown. The locations of the sections are shown in Fig. 24

4.1.5 Spectral Analysis

To further examine the temporal variability of the model, spectra and coherences of the streamfunction fluctuations were computed at a number of points over the domain. Selected spectra, plotted in variance preserving form, are shown in Figs. 21a–c. In comparing these various spectra, a striking feature is the spatially inhomogeneous nature of the variability. Over interior regions, in each of the three layers, the spectra are consistently 'red'; i.e., low frequency motions with periods in excess of 300 days contain most of the energy (e.g. Fig. 21a). These spectra are markedly different from those given by Holland (1978), which show a well–defined peak at a 64 day period with very little energy at lower frequencies. As explained below, the reason is once again the inclusion of topography in the model.

In the boundary current region, higher frequency motions become progressively more energetic with distance downstream. Off Kodiak Island, the top layer spectra are still very red, but the 'mesoscale' frequency band (50–100 day period) is somewhat more energetic than in the interior (Fig. 21b). Farther downstream, particularly after the Stream has separated, the spectra display a high frequency, surface–intensified signal that is due to topographic waves propagating westward along the steep shelf of the Aleutian Trench (Fig. 21c). This signal is the dominant one very close to the sidewall boundary. Farther offshore (say 60 km) the energy is divided between the low and high frequency bands. The sampling period of four days is too long to properly resolve the high–frequency signal in the Alaskan Stream. To better define this signal, the 10–year experiment was extended for 120 days and sampled at a 1–day interval. Spectra computed from this short run showed a single well–defined peak at 0.07–0.08 cpd, which falls off sharply at both higher and lower frequencies.

Inspection of the spectra from the free–slip experiment (MT–FS) showed that the high frequency signal, though still present, was reduced in amplitude by a factor of 5 to 10 compared to the reference experiment. This indicates the importance of

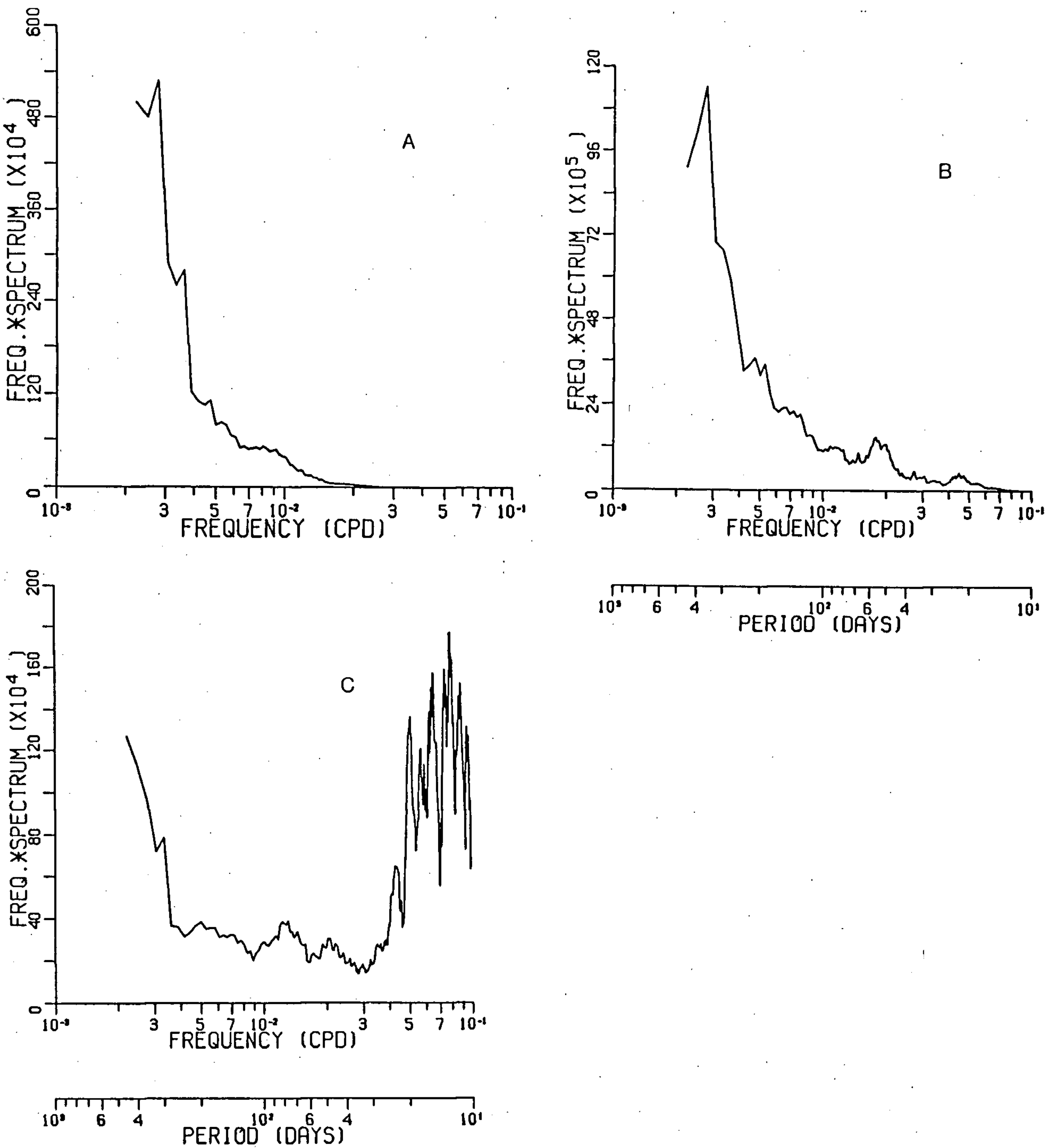

Figure 21. Variance–preserving autospectra of the top layer eddy streamfunction fields from locations in (a) the Alaska Current (at Point **X** on Fig. 24), (b) the Alaskan Stream off Kodiak Island (Point **Y** on Fig. 24) and (c) the Alaskan Stream off the Aleutian Islands (Point **Z** on Fig. 24). Units are cpd $\times \frac{m^4 \ s^{-2}}{cpd}$.

the production of anticyclonic vorticity by the sidewall boundary condition for the generation of topographic waves in the Alaskan Stream.

Coherences were calculated between the streamfunction fluctuations at points over the domain that are separated either vertically or horizontally. The vertical coherences discussed below are between fluctuations of the top and middle layers. In all cases, very similar results are obtained from coherence calculations that involve the bottom layer with those above. Figs. 22a–b show the coherence and phase between fluctuations in the top and middle layers at two representative locations, one in the interior and the other in the boundary current (corresponding to Figs. 21a–b). At the interior point, we see that the fluctuations are coherent at the 99% confidence level over almost the entire range of frequencies. There is a characteristic drop in the coherence at about 0.02 cpd. Below this frequency the bottom layer fluctuations have a significant phase lead over those of the top layer while at higher frequencies there is essentially no phase difference. The phase lead with depth suggests that the low frequency fluctuations are the result of a baroclinic instability process. This may be substantiated by examining the signs of the rates of conversion of mean kinetic and mean potential energies to eddy kinetic and eddy potential energies (see Holland 1978 for details). These two types of energy conversion are the signature of barotropic and baroclinic instability processes, respectively. Away from the boundary current region, the dominant energy conversion is from mean potential to eddy potential energy. Within the boundary current, the conversion rate of mean kinetic to eddy kinetic energy is comparable to that of mean potential to eddy potential energy.

Fig. 22b indicates that the fluctuations of the top and middle layers in the model Alaskan Stream are coherent over the entire resolved spectrum. The phase shows that the bottom layer fluctuations slightly lead those of the top layer for all but the lowest frequencies. The current measurements obtained by Reed and Schumacher (1984) also indicated a high degree of coherence at points separated

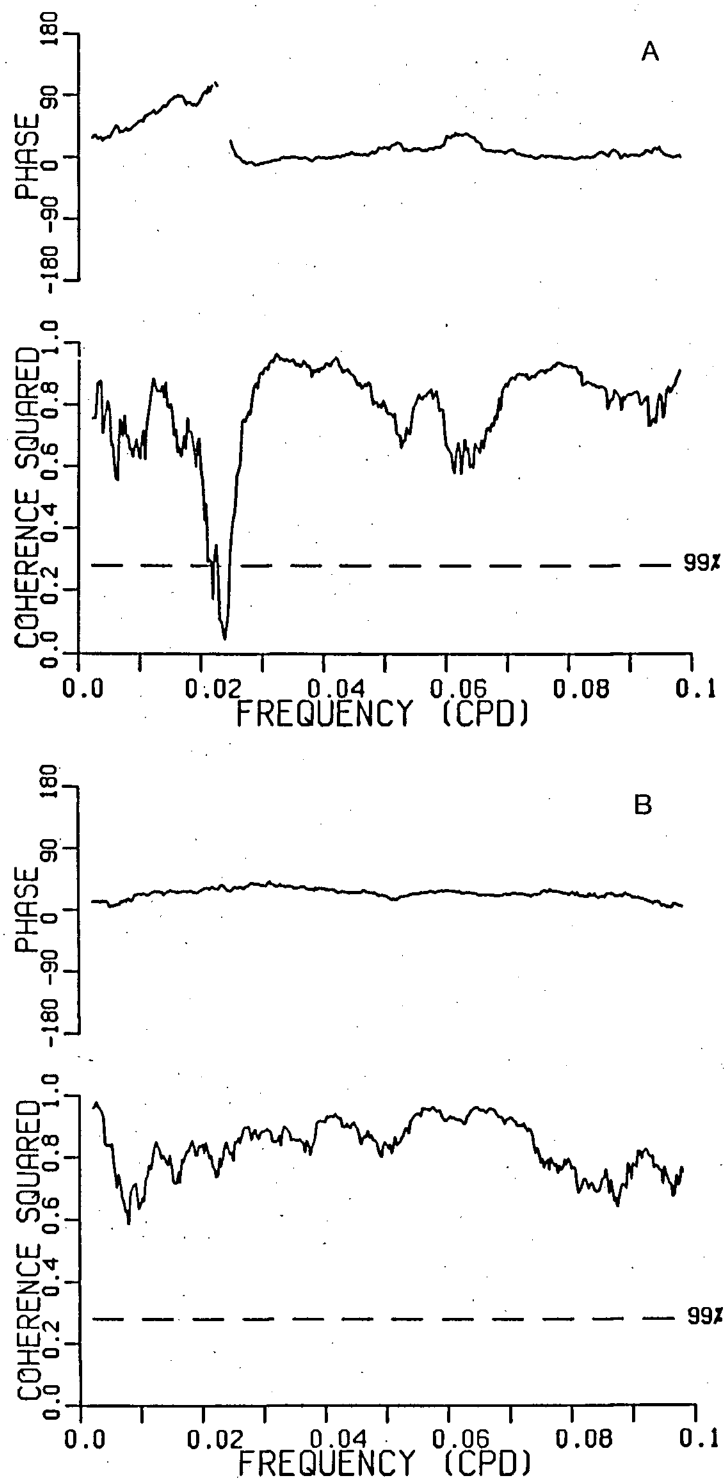

Figure 22. Coherence squared and phase between streamfunction fluctuations in the top and middle layers at locations in (a) the Alaska Current (Point **X**, Fig. 24) and (b) the Alaskan Stream (Point **Y**, Fig. 24). Positive phase implies that the middle–layer fluctuations are leading. The dashed horizontal line indicates the 99% significance level for coherence.

vertically by several hundreds of metres in the axis of the Alaskan Stream.

Additional coherence and phase plots are shown in Figs. 23a–b for points in the western boundary current separated by 40 km in the cross–stream direction and 60 km in the downstream direction. The cross–stream diagram shows that fluctuations are laterally coherent over a wide frequency range, with the offshore fluctuations leading those inshore. The model of barotropic instability, that Mysak (1982) applied to the Alaskan Stream, predicted a similar phase relation in the cross–stream direction. However, Figs. 22b and 23a suggest that both baroclinic and barotropic instability processes are important in the region. Over the length of the Alaskan Stream, the energy conversion due to both of these processes is important.

The coherence and phase for two points separated by 60 km in the model Alaskan Stream off the Aleutian Islands are given in Fig. 23b. As in the previous figures, the fluctuations are coherent across the entire band of frequencies. However, in this case, the phase lag of the downstream point increases in a nearly linear fashion with increasing frequency. Other phase diagrams computed for points separated by 120 km (not shown) also indicate a linear increase in phase lag with frequency, but at twice the rate of Fig. 23b. The simplest interpretation of this phenomena is that the fluctuations are due to topographic waves propagating in the downstream direction of the Alaskan Stream. It is possible to estimate the wavelength of the fluctuations from Fig. 23b. At 0.08 cycles day^{-1} the downstream phase lag is about 135°. For two points separated by 60 km, this implies a wavelength of 160 km, which corresponds quite well with a direct estimate of the wavelength of the fluctuations from the eddy fields. The separation between successive highs of the eddies, in the downstream region of the Alaskan Stream, is about 8 grid intervals, or 160 km. Given a frequency of f=0.08 cpd and a wavelength of L=160 km, the phase speed, $c = f \times L$, is 12.8 km day^{-1}. This is in excellent agreement with the 13 km day^{-1} phase speed estimate of Section 4.1.4. The maximally unstable wave obtained in Mysak's (1982) highly idealized barotropic model of the Alaskan Stream also had similar properties, with a wavelength of 138 km and a phase speed of 10.4 km day^{-1}.

Direct measurements from the downstream region of the Alaskan Stream are not yet available for comparison with the results described here. However, recent satellite images (e.g., Fig. 4) show that the Alaskan Stream in this region is subject to quasi-periodic, cusp-shaped, lateral perturbations with a wavelength of about 150 km. Based upon the model results described above, it is conjectured that these disturbances in the Stream are due to topographic waves with a baroclinic structure.

4.1.6 Vorticity Budgets

The terms in (3.22) were integrated over five subregions, which were considered to be dynamically distinct (Fig. 24). The sponge layer and a strip along the southern boundary have been omitted. There are two distinct western boundary current subregions, a southwestern recirculation subregion, and two interior subregions adjacent to the eastern boundary. The boundary current region was partitioned into two halves to check whether different dynamical balances hold in the separated Alaskan Stream and in the wall-bounded Stream. The interior region to the east was also partitioned for similar reasons.

As Harrison and Holland (1981) have discussed, the choice of subregions can be a difficult matter. One problem that can arise is that, over a subregion, a term may vary from large positive to large negative values so that cancellation results upon integration, and a small net value is obtained. This may then leave the erroneous impression that the term is unimportant over the subregion. The subregions given in Fig. 24 were chosen on the basis of the different flow regimes suggested by the mean streamfunction. However, the western boundary current has a complex structure, with some terms changing sign over the width of the current. Thus the boundary layer current can contain several sublayers with different dynamical balances. With

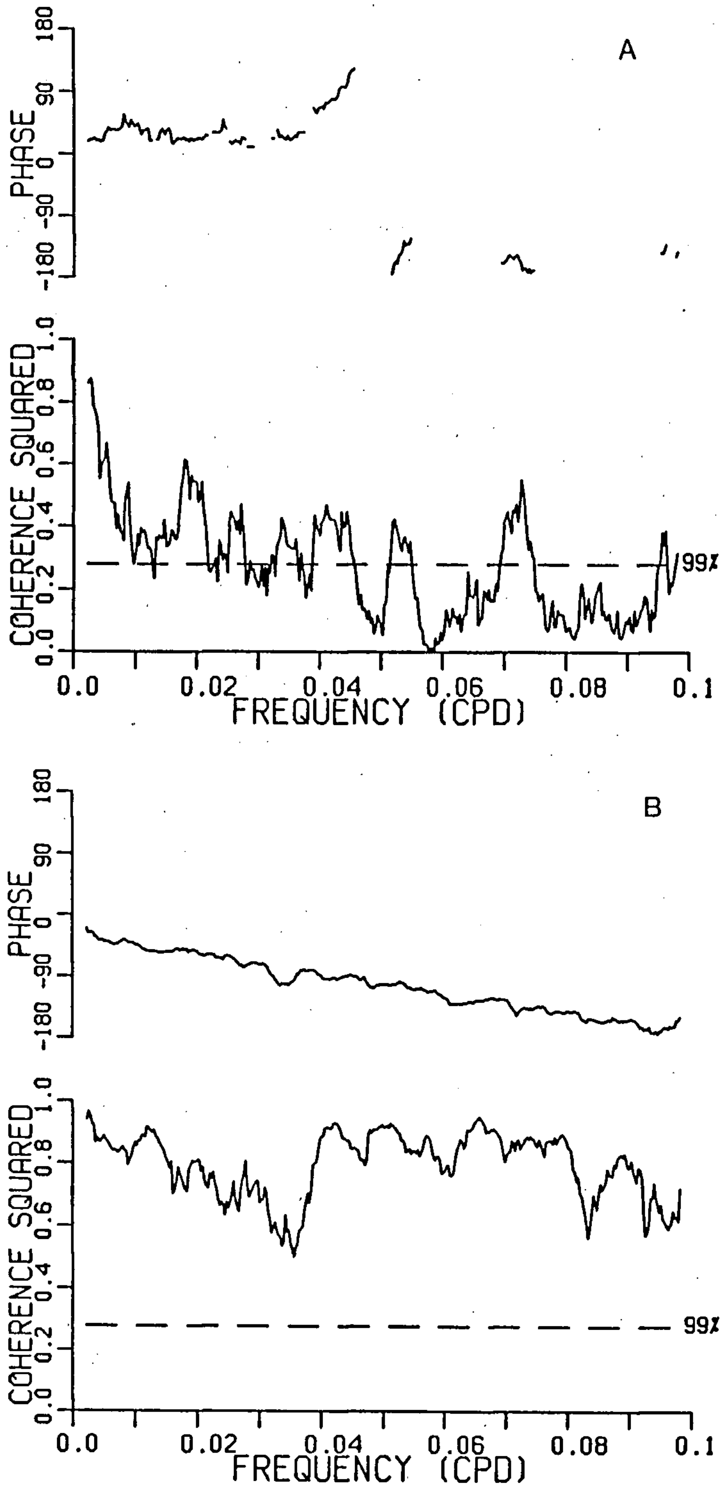

Figure 23. Coherence squared and phase between top layer streamfunction fluctuations at locations in the Alaskan Stream. In (a) the points are separated by 56 km in the cross-stream direction and are located off Kodiak Island (Point **Y**, Fig. 24). In (b) the points are separated by 60 km in the downstream direction and are located off the Aleutian Islands (Point **Z**, Fig. 24). The phase is positive when the offshore point is leading in (a) and when the downstream point is leading in (b).

this caveat in mind, vorticity budgets are presented for both the depth–integrated flow and the top and middle layers of the model.

A 10–year period (e.g., as employed by Harrison and Holland) was used for the time–averaging in (3.22). In the following tables, the effect of a small residual time derivative term will be noticed. (In the absence of a residual, the terms in each of the columns of Tables 2–4 would sum to zero.) For all the cases discussed, this residual is much smaller than the dominant vorticity terms.

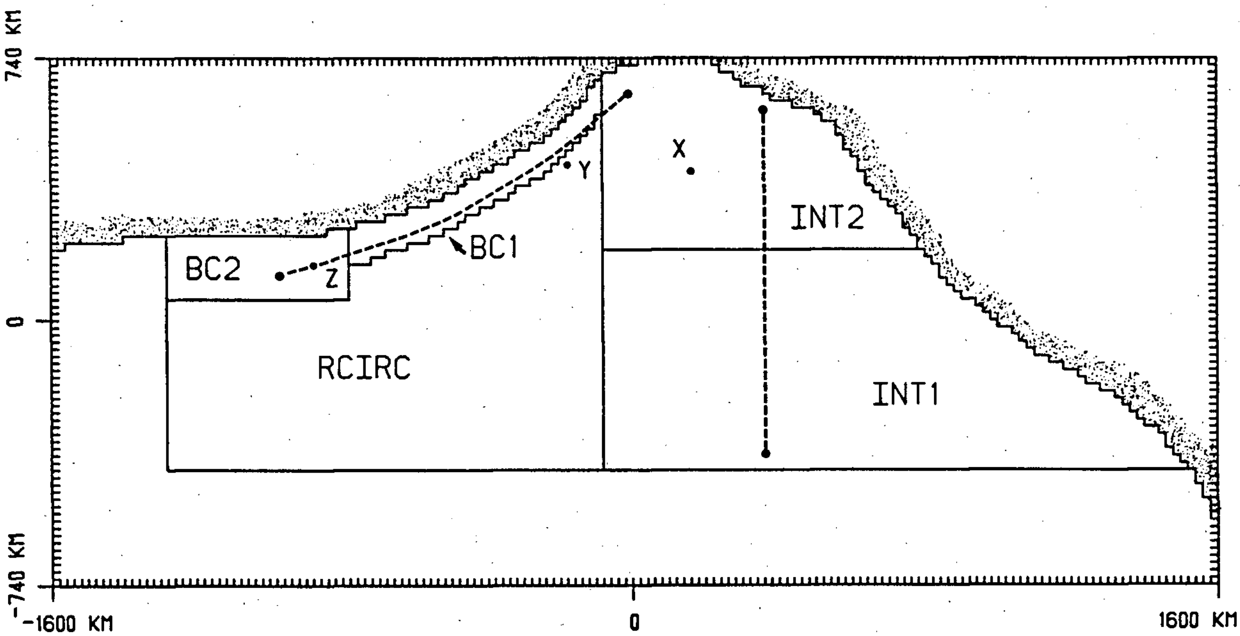

Figure 24. Subregions of the model domain used in the computation of vorticity budgets. The dashed lines indicate the sections of the Hovmöller diagrams given in Fig. 20. The points labeled X,Y and Z give the locations for the spectra and coherences of Figs. 21–23.

The most readily interpreted budgets are the depth–integrated ones in which the vortex stretching terms exactly cancel. The resulting budgets are summarized in Table II where the various terms, such as $PADV$, now represent a summation over the three layers. In both interior subregions, the Sverdrup balance between planetary advection and the wind stress curl is obtained, although the advective terms also make a modest contribution in subregion INT2 (17% of $PADV$). In the RCIRC subregion, the dominant balance is again between planetary advection and the wind curl. The MADV term also makes a significant contribution (46% of $PADV$), most of which derives from large negative values near the BC2 subregion.

	Subregions				
Vorticity terms	INT1	INT2	RCIRC	BC1	BC2
$PADV$	-71.4	-43.8	-57.5	40.6	9.2
$MADV$	-1.1	-5.0	-31.1	18.4	-4.9
$EADV$	-0.4	-2.6	4.7	-20.3	-9.8
$DISS$	-1.0	-1.6	5.6	-49.0	-3.9
$CURL$	73.9	49.8	82.5	11.1	10.1
$BFRIC$	0.0	0.2	-0.1	0.2	0.0
$TOPO$	0.0	2.8	-4.3	0.4	-0.6

Table II. Depth–integrated vorticity budgets for experiment MT. The units of the spatially integrated vorticity tendency terms are $m^3\ s^{-2}$.

In the upstream boundary current subregion, BC1, the main balance is between southward advection of planetary vorticity and the diffusion of mean vorticity. However, this Munk–type frictional boundary layer balance, for the model Alaskan Stream, does not entirely apply because the inertial terms are significant. The mean and eddy advection terms are of opposite sign, and both have a magnitude of about half of $PADV$.

Inertial effects are also likely to be important in setting the lateral scale of the boundary current. The frictional boundary layer theory predicts a lateral scale of O(25 km) which is much smaller than the scale of O(100 km) that is obtained. The topography, in particular the width of the Aleutian Trench, may also be important in establishing this length scale.

In subregion BC2, the model Alaskan Stream has separated from the boundary, and dissipation is much less important. There is no clear balance between two terms here, but the advective terms (especially $EADV$) have a much greater relative importance, and $PADV$ is much smaller because the mean flow is nearly zonal in this subregion.

The top and middle layer vorticity budgets given in Tables III and IV indicate that simple two–term balances are obtained in only one or two of the subregions of the middle layer. In the top layer of subregion INT1, the $CURL$ term is balanced by $PADV$ and $MSTR_{1+\frac{1}{2}}$. This implies that the wind curl drives the fluid northward in the top layer and deforms the top interface. This then induces northward advection in the middle layer. The balance in subregion INT1 for the middle layer is essentially the classical vorticity balance between vortex stretching and planetary advection (see Table IV). Harrison and Holland (1981) obtained a similar result within the interior of the bottom layer of a two–layer model.

	Subregions				
Vorticity terms	INT1	INT2	RCIRC	BC1	BC2
$PADV$	-39.5	-25.6	-28.1	22.9	5.0
$MADV$	-0.8	-4.4	-23.7	10.8	-3.9
$EADV$	-0.3	-2.9	3.5	-18.7	-9.2
$MSTR_{1+\frac{1}{2}}$	-18.9	-8.3	-20.6	7.6	7.7
$ESTR_{1+\frac{1}{2}}$	-11.1	4.1	-13.3	14.8	-0.6
$DISS$	-5.9	-15.8	3.1	-48.4	-10.1
$CURL$	73.9	49.8	82.5	11.1	10.1

Table III. Top layer vorticity budgets for experiment MT. The units of the vorticity tendency terms are $m^3\ s^{-2}$.

The balance in the RCIRC subregion of the middle layer resembles that of subregion INT1. Vortex stretching and planetary advection are again the important terms of this layer. In the top layer, there is an additional contribution from $MADV$ to balance the $CURL$ term.

The balances for the top and middle layers in subregion INT2 are much more complex. Dissipation is important in both layers – but of opposite sign in each. This led to a virtual cancellation in the depth–integrated budget and the illusory impression that dissipation was unimportant in INT2. A closer examination of the dissipation term revealed that its importance in INT2 derives from large values adjacent to the eastern wall. These budgets suggest that all the vorticity terms contribute significantly near the head of the Gulf.

For the top layer BC1 subregion, $DISS$ is balanced by $PADV$ and $ESTR_{1+\frac{1}{2}}$. The middle layer displays the classical balance between vortex stretching and planetary advection. The top and middle layer budgets for the BC2 subregion are as difficult to sort out as the depth–integrated budgets, in which no simple balances are apparent.

	Subregions				
Vorticity terms	INT1	INT2	RCIRC	BC1	BC2
$PADV$	-31.2	-17.6	-25.9	17.2	4.1
$MADV$	-0.3	-0.6	-7.3	7.5	-1.0
$EADV$	0.2	0.1	1.4	-1.9	-1.0
$MSTR_{1+\frac{1}{2}}$	18.9	8.3	20.6	-7.6	-7.7
$ESTR_{1+\frac{1}{2}}$	11.1	-4.1	13.3	-14.8	-0.6
$MSTR_{2+\frac{1}{2}}$	-0.0	0.1	-2.5	-0.0	-0.2
$ESTR_{2+\frac{1}{2}}$	-1.8	1.5	-1.9	2.5	0.2
$DISS$	4.6	13.5	2.2	-1.9	5.7

Table IV. Middle layer vorticity budgets for experiment MT. The units of the vorticity tendency terms are $m^3\ s^{-2}$.

The vorticity balances of the bottom layer are not discussed because the residual time derivative term for this layer is comparable to the largest terms. It appears that an averaging period of ten years is insufficient to obtain reliable statistics in a deep layer with topography. However, all the vorticity terms in this layer are very small in comparison with the important terms of the overlying layers. It is apparent, however, that the topographic vortex stretching tendency is an important component of the vorticity balances of this layer.

Thomson (1972) developed a depth–integrated, frictional model for the Alaskan Stream in which the diffusion of anticyclonic vorticity from the coast balances the gain of anticyclonic (planetary) vorticity from the southward movement of water parcels. He suggested that, with the increasingly zonal orientation of the boundary, planetary advection would, at some point, be incapable of balancing dissipation, and that the frictional boundary layer flow would breakdown. He anticipated that the Stream would then separate from the boundary and that other terms in the vorticity equation (e.g., the inertial terms) would become more important.

There are some similarities between this model and the vorticity budgets. The primary balance in the wall–bounded portion of the depth–integrated model Alaskan Stream is between planetary advection and dissipation, as in Thomson's model. However, in contrast to his model, the advective terms are not negligible over the width of the boundary current. Also, in a mean sense, the current separates from the boundary once it is zonally oriented, and the contribution of the dissipation term to the vorticity budget is much reduced there. The inclusion of a no–slip boundary condition at the sidewall is essential in obtaining separation of the boundary current in the model.

4.2 Discussion

It is clear from the foregoing presentation that the limited–area QG model successfully simulates many of the characteristics of the wind–driven circulation of the subpolar gyre of the NE Pacific. The following itemized list summarizes the main points of agreement between observations and the model.

- The spatial distribution of the mean top layer potential vorticity over the gyre is consistent with the analyses of Talley (1988).
- The lateral scale of the model Alaskan Stream is correct.
- The vertical and horizontal coherence of the Stream is maintained over its length, as observed. The level of eddy variability in the top layer is consistent with direct measurements off Kodiak Island.
- Mean flow speeds in the top layer are consistent with current meter measurements from the Stream.
- The observed meandering of the Stream is modelled, at least in a qualitative sense.
- Topographic waves with a baroclinic structure are identified as a potentially significant component of the variability of the Alaskan Stream. Shear at the boundary is important for the generation of these waves.
- Eddies are obtained in the model Alaska Current which bear some of the characteristics of the observed eddies (e.g., the Sitka Eddy). Baroclinic instability is suggested to be the dominant generating mechanism.

There are also points of disagreement between model and observations. These are itemized below, along with possible reasons for the discrepancies.

- The mean transport of the Alaskan Stream appears to be too small (21 Sv vs. 28 Sv estimated by Warren and Owens (1989)). Setting aside the question of uncertainty in the measurement, the model transport may be in error because the wind stress curl over the Gulf may be underestimated by the Hellerman and Rosenstein winds.
- The vertical structure of the mean flow in the model Alaskan Stream is too baroclinic. There is insufficient flow beneath the top layer. This may be partly

due to the coarse vertical resolution.

- Based on current measurements in the Alaskan Stream, it appears that the level of eddy variability below the top layer is too small. This is likely due to excessive lateral friction and to poor vertical resolution. Additional vertical resolution is required to improve the vertical representation of eddy statistics, although it is not clear how much resolution is sufficient.
- The model Alaska Current does not have sufficient horizontal structure. The eddies generated within it are too weak. Excessive lateral friction over the interior is a likely cause of this deficiency.

The problem with the transport indicates that, as mentioned above, the Hellerman and Rosenstein (1983) winds are too weak, perhaps because a constant drag coefficient was used in their calculation. Harrison (1989) has recently recalculated these winds using the drag coefficient formulation proposed by Large and Pond (1981). The latter allows for an increase in the drag coefficient for large wind speeds. His results show an increase in the magnitude of the wind stress curl over the Gulf of Alaska, particularly for the winter months. This suggests that some improvement in the simulation of the transport may be possible by driving the model with Harrison's new wind stresses.

5. Flat–Bottom Experiment

Recent observational studies have suggested that the bottom topography could have an important influence on flow characteristics in the Gulf. Warren and Owens (1985, 1988) attribute the existence of an eastward jet above the Aleutian Rise (49.5°N, 175°W) to the variation in the bottom slope of the Rise. Royer and Emery (1987) proposed that the interaction of the Sverdrup flow with bottom topography leads to a bimodal circulation pattern in the Gulf. However, to date, there has been very little discussion in the literature on the possible influence that the Aleutian Trench, which is one of the most prominent topographic features in the region, might have on the circulation. The Alaskan Stream, which is the western boundary current of the subarctic gyre in the North Pacific, flows above the Trench for a distance of over of 2000 km. Yet it is not clear what control, if any, the Trench maintains on the flow of the Stream. Some evidence for a topographic influence on the Stream was given in Chapter 4, where it was noted that the presence of the Trench supported the existence of baroclinic topographic waves. These waves are generated by lateral shear at the boundary and travel westwards with a phase speed of about 13 km day^{-1}.

In this chapter, the influence of bottom topography on the circulation of the model Alaskan Gyre is investigated in the context of steady wind forcing. Results are presented from an experiment, MF, that is identical in every respect to MT, except for the omission of bottom topographic variations. The characteristics of the model Alaskan Stream in the flat–bottom model are shown to be markedly unrealistic. The Aleutian Trench is found to have an important role in maintaining the horizontal coherence of the Stream. An analysis of the energetics from experiments MT and MF shows that bottom topography very effectively attenuates the eddy energy in the barotropic mode.

5.1 Results

The initial conditions for the flat–bottom experiment, MF, were taken from the end state of MT. An adjustment period of three years elapsed before data from a ten-year integration were stored on tape. Figs. 25a-c show typical instantaneous streamfunction fields from each of the three layers. Some important differences between the results of this experiment and of MT are immediately evident here. Most striking is the difference in the character of the western boundary current representing the Alaskan Stream. The surface expression of the Stream is disrupted by an intense series of cyclonic eddies which occur along the southern flank of the current. This is in sharp contrast to the model Stream from MT which was a narrow, continuous current over its entire length. The eddies in Fig. 25 are surface intensified, vertically coherent, and propagate tangentially along the sloping western boundary with a speed of 3.5 to 4.5 km day^{-1}. Examination of a time history of instantaneous streamfunction maps show that the boundary current eddies are very long–lived features. In fact, they do not dissipate before reaching the sponge layer near the western wall. In MT, the streamfunction field of the bottom layer was very weak, and, over large expanses, the layer was virtually motionless. The situation in MF is quite different. The eddies drive substantial flows in the bottom layer, particularly in the vicinity of the boundary current. The basin–integrated kinetic energy per unit area of the bottom layer, which was so small in MT (see Fig. 11), is now much larger and, in fact, exceeds that of the middle layer.

In the time–averaged streamfunction fields of Figs. 26a–c, the model Alaskan Stream emerges from the field of eddies. One of the principal differences with MT is in the vertical structure of the mean flows. The deep layer displays a cyclonic gyre confined to the western part of the domain which is much more intense than in MT. The deep mean flow on the eastern side of the basin is, however, very weak in both experiments. Off Kodiak Island, top layer particle speeds in the model Alaskan Stream are comparable in the two experiments, viz., about 30 cm s^{-1}. Further downstream, off the Aleutians, particles speeds are weaker in MF with values of

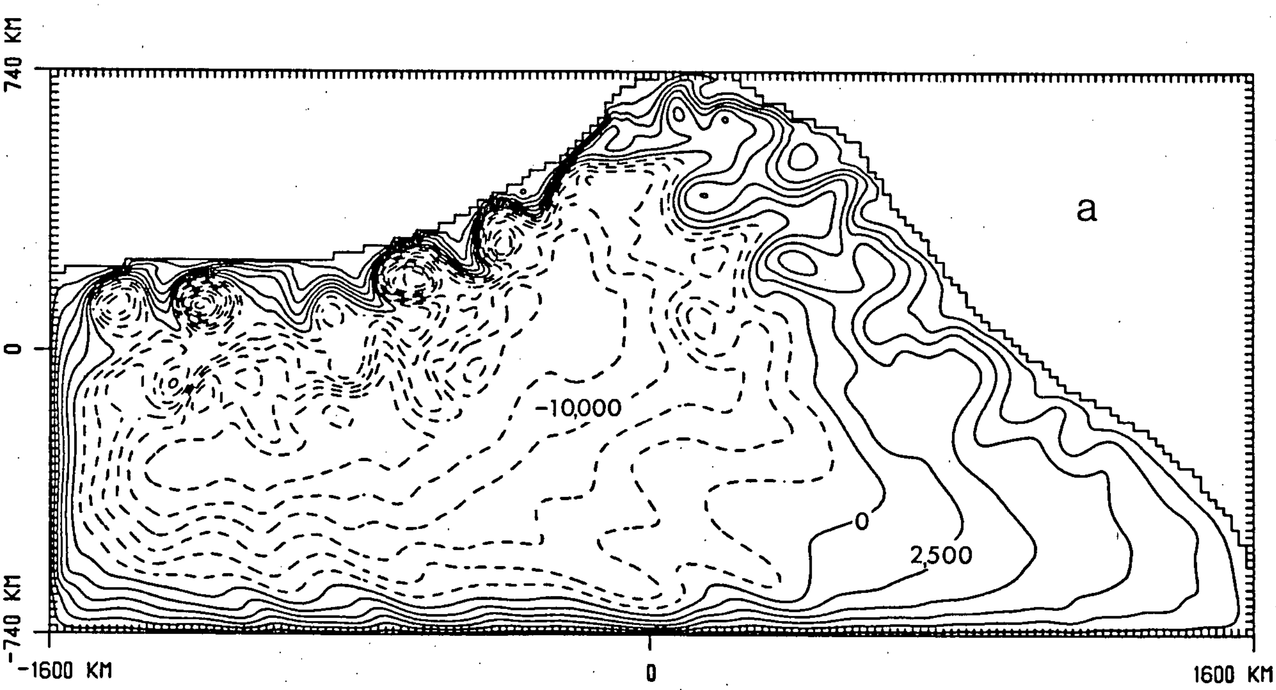

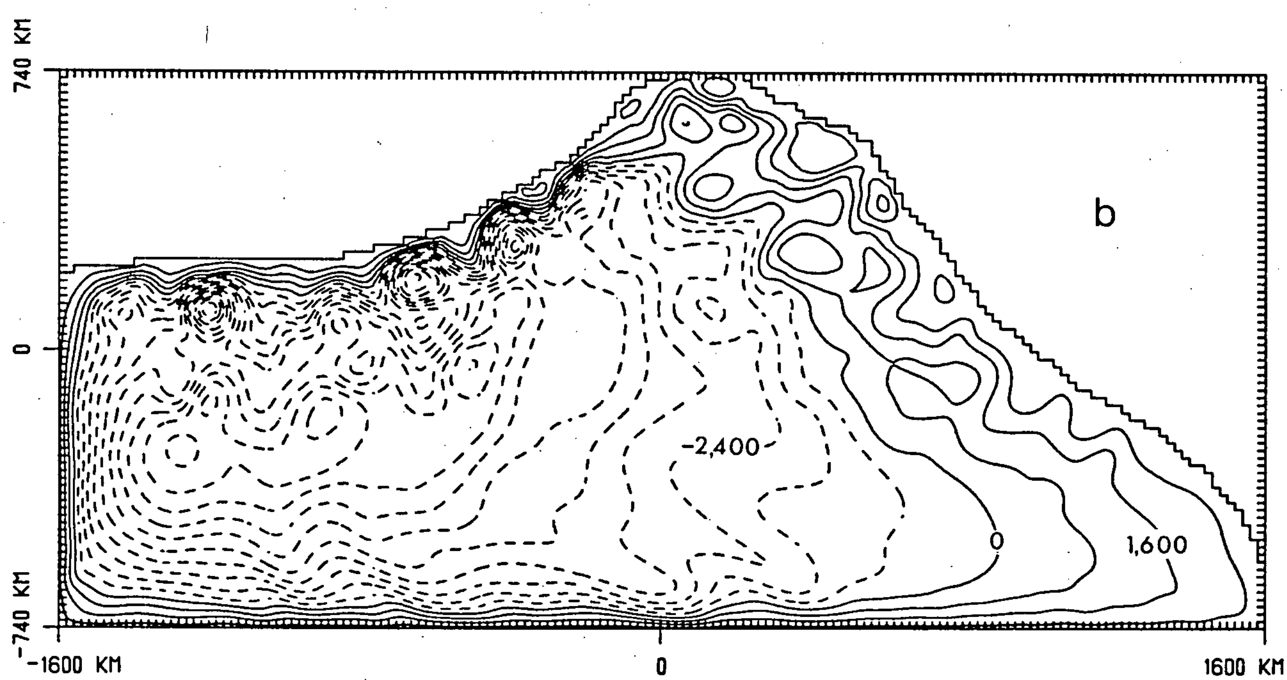

Figure 25. The instantaneous streamfunction fields on Day 1600 from experiment MF for (a) the top layer (CI = 2500 m^2 s^{-1}), (b) the middle layer (CI = 800 m^2 s^{-1}) and (c) the bottom layer (CI = 500 m^2 s^{-1}).

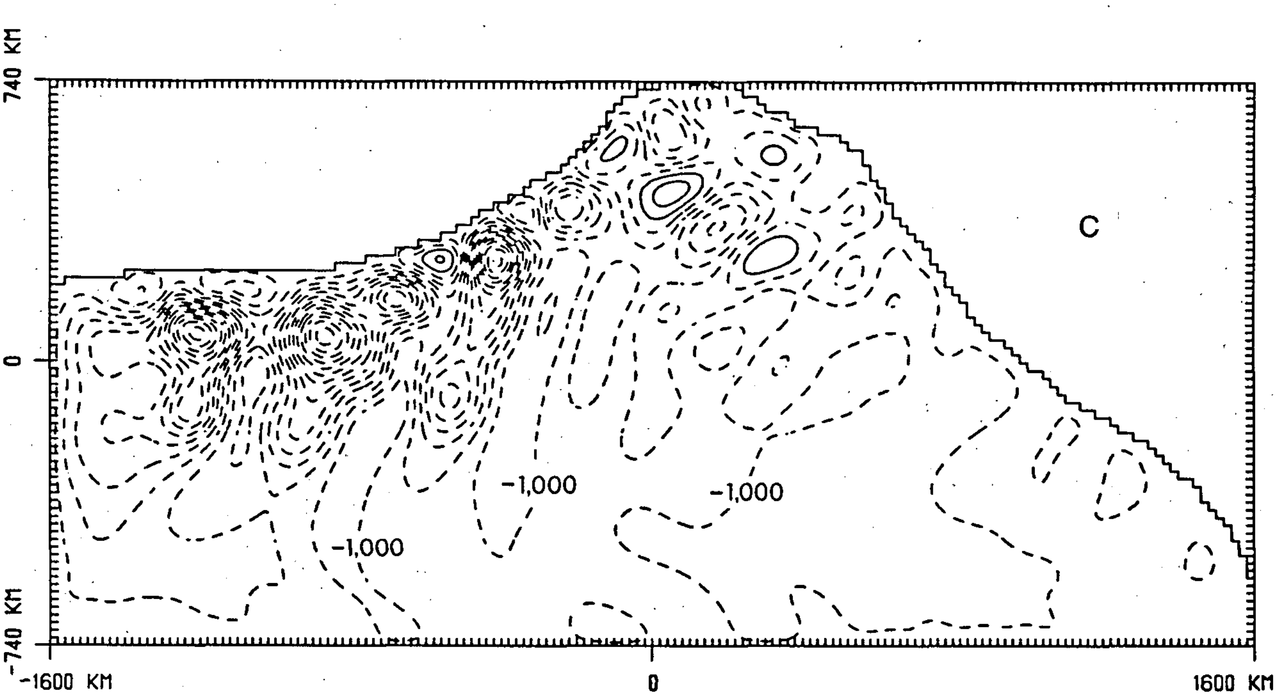

Figure 25 continued.

about 20 cm s^{-1} compared to over 50 cm s^{-1} in MT. In the two experiments, the magnitude of the mean volume transport of the gyres is noticeably similar: 20.7 Sv in MF and 21.2 Sv in MT. The average transport would seem to be determined solely by the Sverdrup transport implied by the wind stress curl forcing.

The greater eddy activity of MF is reflected in the eddy kinetic energy fields (EKE) shown in Figs. 27a–c. In the flat-bottom experiment, the peak EKE are about four times larger than in MT. In the latter, the largest EKE values were found off the portion of the boundary representing the Aleutian Islands and were associated with topographic waves over the Aleutian Trench. These waves are, of course, absent in MF, and the maximum EKE occurs further upstream. The lower

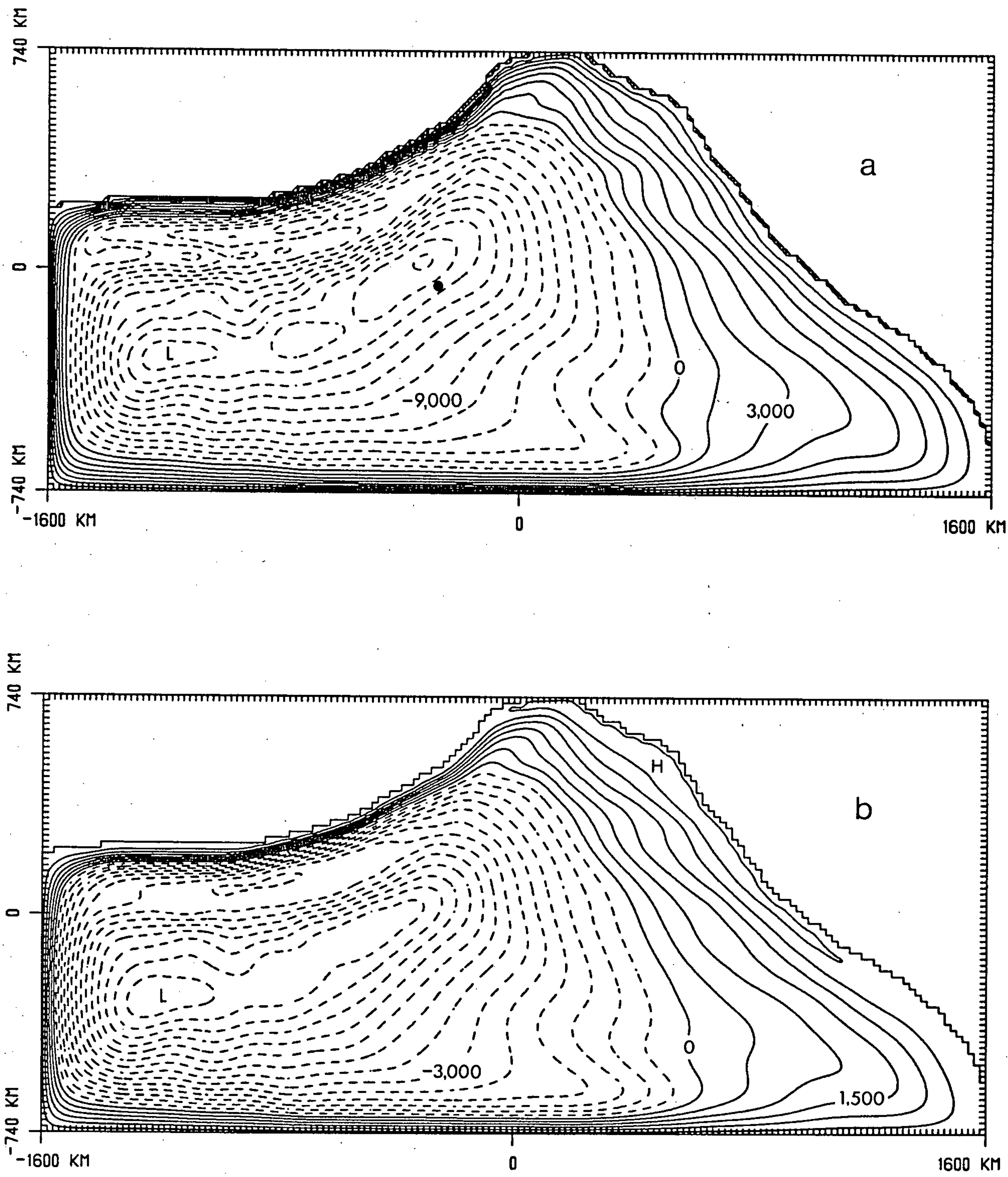

Figure 26. The mean streamfunction fields from experiment MF for (a) the top layer (CI = 1500 $m^2\ s^{-1}$), (b) the middle layer (CI = 500 $m^2\ s^{-1}$) and (c) the bottom layer (CI = 250 $m^2\ s^{-1}$).

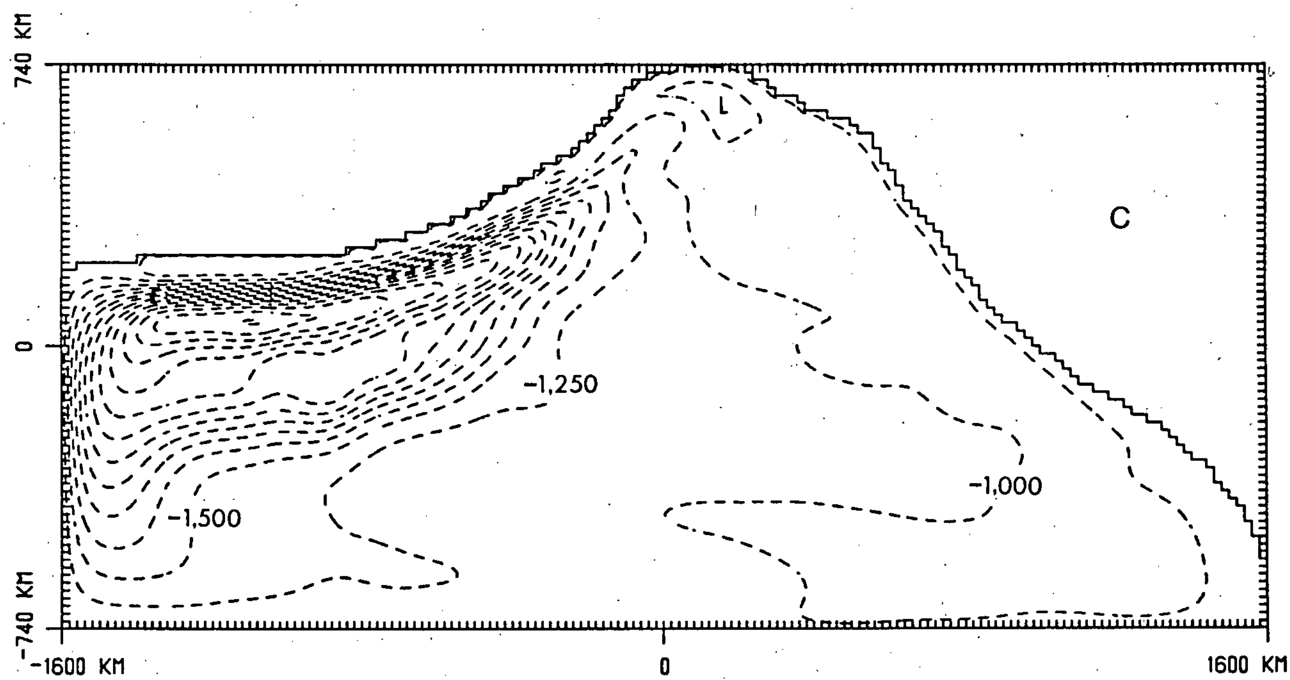

Figure 26 continued.

layers also display increased EKE levels in MF, particularly in the bottom layer where the EKE is increased by one to two orders of magnitude. In the two experiments, the EKE levels over broad interior regions are very low.

For the two experiments the essential difference in the nature of the eddy fields is manifested in Fig. 28, where a comparison is presented of the spectra of the modal streamfunction fluctuations from MT and MF. The most energetic signal in the flat–bottom experiment has a period of about 100 days and is principally in the barotropic mode. The spectral peak at this period is attributable to the mesoscale eddies, evident in Figs. 25a–c. Spectra obtained from other varied locations throughout the model domain also display a large peak at this period. This spectral peak

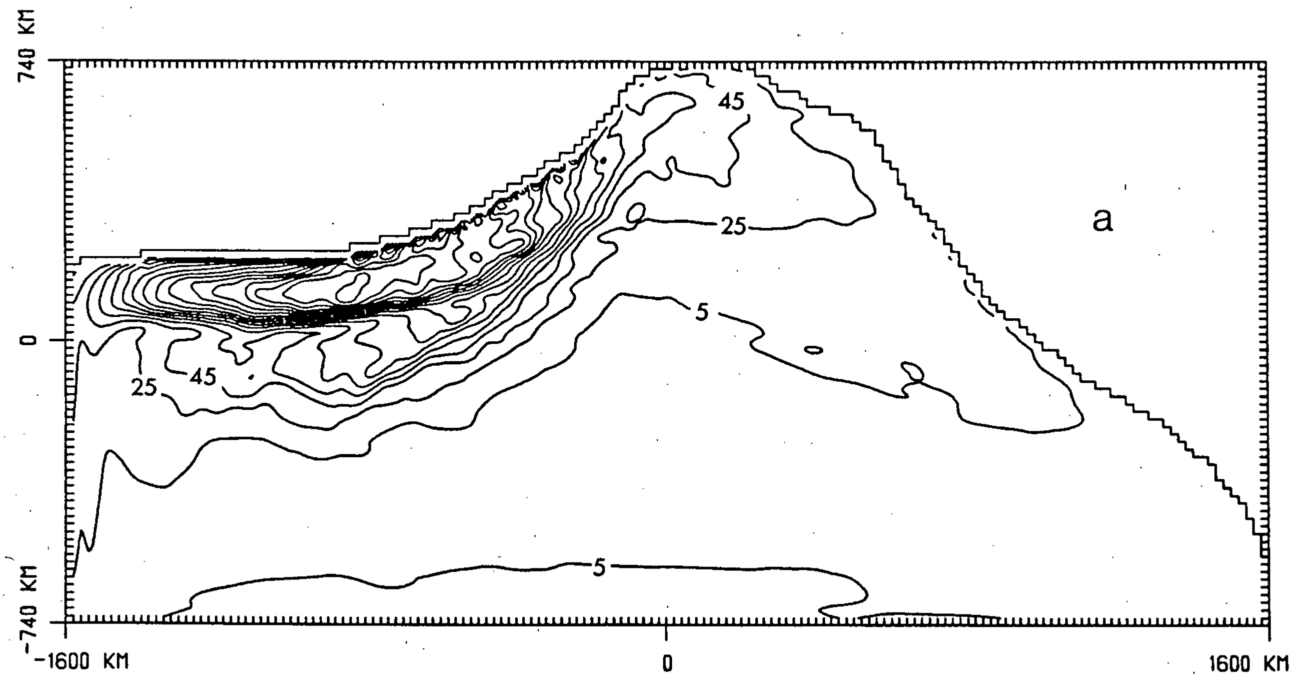

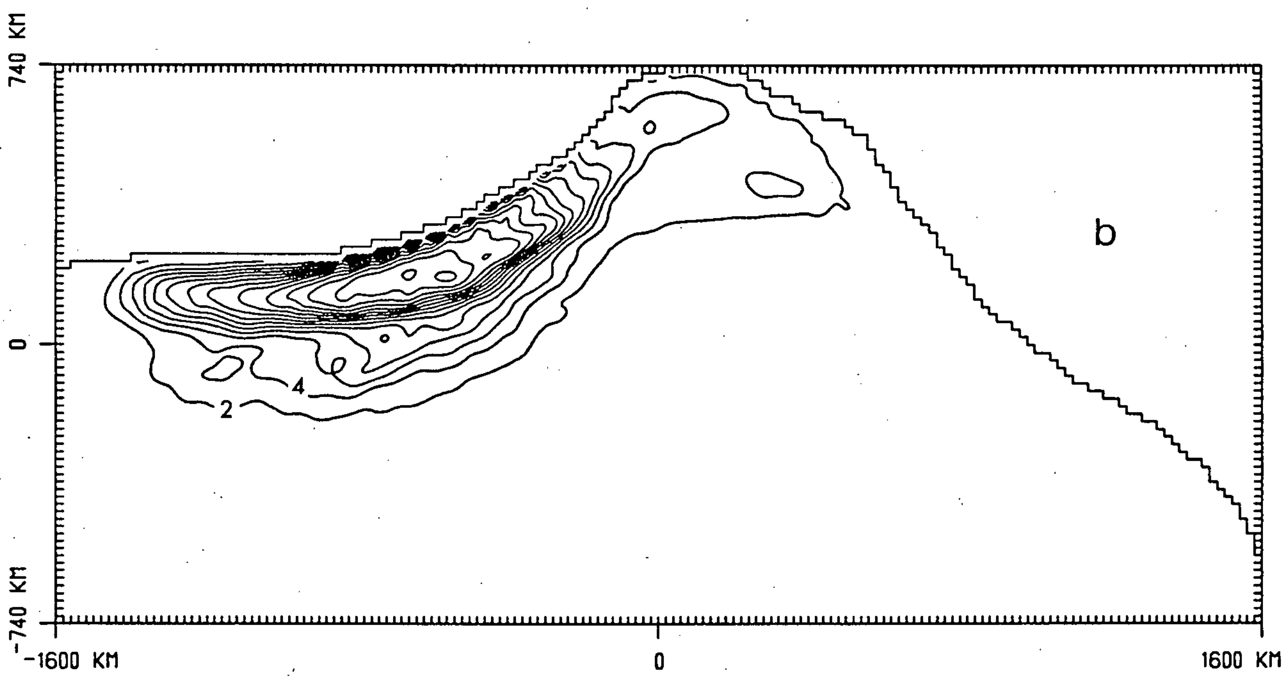

Figure 27. The eddy kinetic energy fields from experiment MF for (a) the top layer (CI = 20 cm^2 s^{-2}), (b) the middle layer (CI = 2 cm^2 s^{-2}) and (c) the bottom layer (CI = 1 cm^2 s^{-2}).

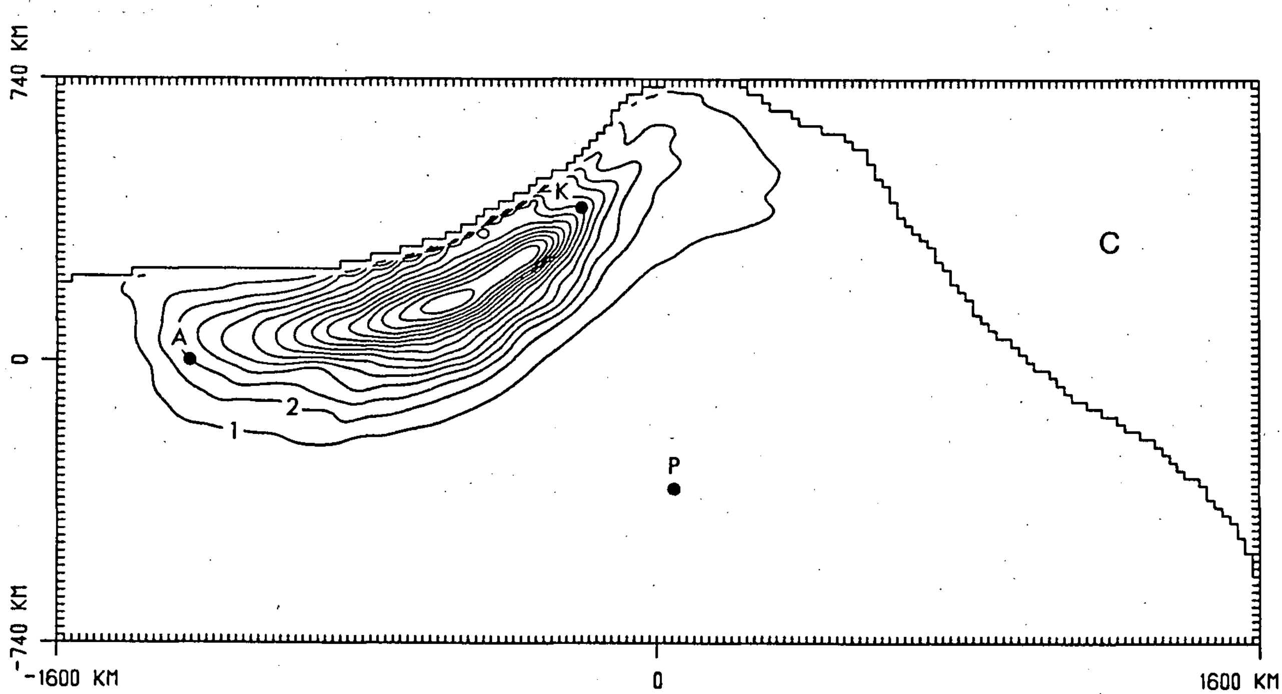

Figure 27 continued.

is consistent with other flat–bottom eddy–resolving experiments; e.g. the dominant mesoscale eddy period in the models of Holland (1978) and Cox (1985) is 50–60 days. The difference in the mean vertical shear and in environment parameters, such as the stratification and beta, probably accounts for the difference in the dominant eddy period of these models and the one obtained here. The empirical orthogonal function (eof) analysis presented in Chapter 6 shows that the 100 day signal is due to barotropic wave propagation along the boundary. The barotropic mode spectrum from MF shown in Fig. 28 tapers off rapidly at higher and lower frequencies. Although none of the spectra examined from MF showed a significant peak at periods shorter than about 100 days, in regions near the head of the Gulf the spectra indicated the existence of fluctuations with an interannual time scale in the baroclinic modes.

The spectra from MT are in sharp contrast to those of MF with the fluctuations predominantly in the first baroclinic mode and of much lower frequency. Due to the band averaging, the ten–year time series used to compute the spectra in MT is of insufficient length to resolve the low frequency end of the spectrum. It does appear that fluctuations with periods in excess of one year contain most of the energy. In none of the spectra examined from MT is there anything resembling the 100 day mesoscale eddy peak found in MF. Also, throughout the domain, the barotropic mode fluctuations are consistently less energetic than those of the first baroclinic mode.

A comparison of results from MF with observations of the Alaskan Stream immediately shows that the horizontal structure of the model boundary current is markedly unrealistic. Observations of dynamic topography have consistently shown that the structure of the Stream is very stable. The picture which emerges from these data is of a continuous current extending from near the head of the Gulf for some 2000 km out along the Aleutian Island arc. Although the Stream is occasionally subject to lateral perturbations (Reed et al., 1980) and also possibly contains topographic waves, there has been no evidence of the intense mesoscale eddy activity which characterizes the boundary current of MF (e.g. Fig. 26a). Furthermore, this is not likely a consequence of poor spatial sampling. For example, hydrographic sections reported in Royer and Emery (1987) were closely spaced and designed with the intention of revealing the eddy field of the Alaskan Stream. However, the authors found that "One oceanic feature missing from the dynamic topography in the NE Pacific in August 1981 is the mesoscale eddy structure that is common to most other parts of the world's oceans. "

As stated in Chapter 4, the boundary current structure of MT is consistent with

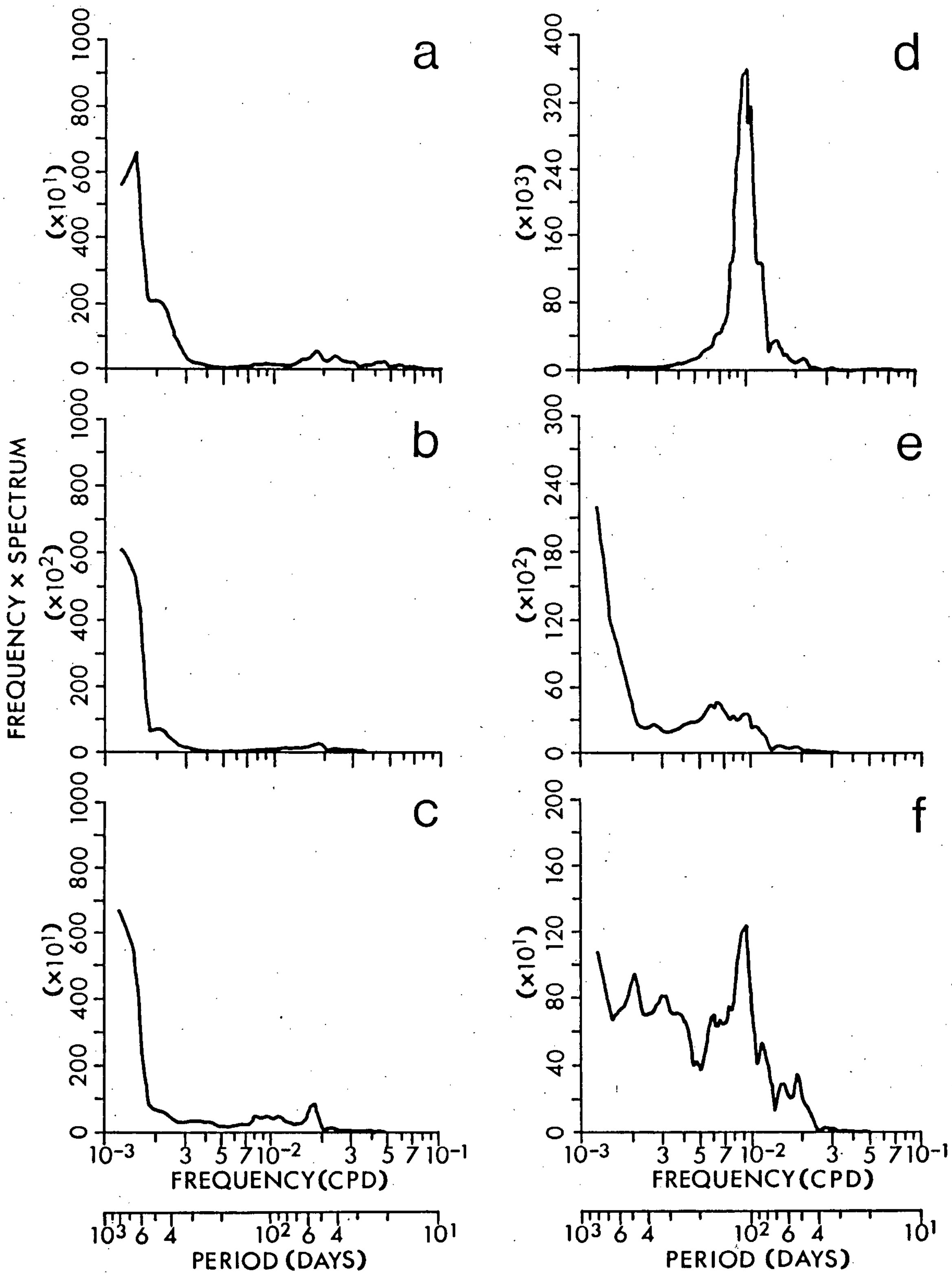

Figure 28. Variance–preserving autospectra of modal streamfunction fluctuations from experiment MT from a location near the center of the domain (marked by the bold dot in Fig. 26a): (a) the barotropic mode, (b) the first baroclinic mode and (c) the second baroclinic mode. The corresponding spectra from MF are shown in (d–f). Note that the spectra have different vertical scales. Units are cpd $\times \left(\frac{m^4\ s^{-2}}{cpd}\right)$.

the observations in several respects. Therefore, the bottom topography, particularly the Aleution Trench, appears to provide an important constraint on the motion of the Stream. The presence of the Trench creates a large gradient in mean potential vorticity along the western boundary. This gradient inhibits lateral motions and stabilizes perturbations of the boundary current. In the model, the influence of the bottom topography upon the flow in layers which are not in direct contact with it enters through the interface displacements. During the spin–up phase of the experiments, the interfaces are distorted from their initially prescribed states and, consequently, an important component of the mean potential vorticity fields of the upper layers becomes established.

5.1.1 Vorticity Budgets

The vorticity budgets for MF, which are given in Tables V–VIII, indicate the nature of the eddy processes and the downward transfer of vorticity occurring during the experiment. As in MT, the depth–integrated budgets for subregions INT1 and INT2 show the usual Sverdrup balance between the advection of planetary vorticity and the wind stress curl over the basin interior. The RCIRC region is also characterized by a Sverdrup balance, however, eddy advection is also of significance (14% of CURL). This latter term contributes mostly in proximity to subregion BC1.

	Subregions				
Vorticity terms	INT1	INT2	RCIRC	BC1	BC2
PADV	-71.9	-42.0	-80.3	44.6	10.4
MADV	-0.1	-4.1	-9.2	4.4	2.1
EADV	0.1	-5.9	11.3	-55.1	-8.6
DISS	-1.8	-0.4	0.4	-13.3	-12.5
CURL	73.9	49.8	82.5	11.1	10.1
BFRIC	-0.2	1.6	-4.2	9.1	-1.0

Table V. Depth–integrated vorticity budgets for experiment MF. The units of the vorticity tendency terms are m^3 s^{-2}.

The most significant departure from the depth–integrated vorticity budgets of MT occurs in subregion BC1, where EADV is a much larger term, and the dominant balance here is between the advection of planetary and eddy vorticity. The importance of dissipation is not evident in the depth–integrated budget of BC1 since there is a partial cancellation of this term in the summation over layers.

An examination of the layer vorticity budgets shows that, on the eastern side of the basin, there is little difference between MF and MT. In subregion INT1, CURL drives PADV in the top layer and mean vortex stretching of the upper interface. This interfacial stretching induces PADV in the middle layer. The vortex stretching of the lower interface is small so that all the vorticity tendency terms in the lower layer are small. This accounts for the very weak mean flows found in the bottom layer on the eastern side of the basin (Fig. 26c). In subregion INT2, CURL is balanced by PADV and DISS. The stretching terms for the lower interface are again small, resulting in very weak bottom layer flows.

	Subregions				
Vorticity terms	INT1	INT2	RCIRC	BC1	BC2
$PADV$	-36.5	-21.9	-21.6	14.5	2.2
$MADV$	-0.1	-3.8	-3.3	-1.7	2.0
$EADV$	-0.3	-5.2	29.8	-73.7	-12.5
$MSTR_{1+\frac{1}{2}}$	-24.0	0.9	21.5	9.3	3.9
$ESTR_{1+\frac{1}{2}}$	-4.9	-0.2	-133.3	95.9	20.1
$DISS$	-4.6	-18.5	1.2	-55.1	-25.3
$CURL$	73.9	49.8	82.5	11.1	10.1

Table VI. Top layer vorticity budgets for experiment MF. The units of the vorticity tendency terms are m^3 s^{-2}.

In contrast to this, significant deep flows are driven by downward eddy fluxes in the subregion RCIRC. The top layer is characterized by a balance between CURL and eddy vortex stretching. Eddy advection is also significant (36% of CURL). The main balance in the middle layer of RCIRC is between eddy vortex stretching of the upper and lower interfaces. Thus, vorticity fluxes, downward through the middle layer, into the bottom layer, where the vortex stretching of the lower interface is balanced by PADV and EADV.

In the top layer of subregion BC1, the essential balance is between eddy advection and eddy vortex stretching, with an important contribution from DISS. The eddy stretching of the upper and lower interfaces gives the main vorticity balances of the middle layer in the boundary current subregion of MF. In the bottom layer, the stretching of the overlying interface is balanced mainly by DISS, but EADV and PADV are also significant terms. The layer vorticity balances of subregion BC2 are quite similar to those of subregion BC1.

	Subregions				
Vorticity terms	INT1	INT2	RCIRC	BC1	BC2
$PADV$	-31.6	-16.2	-9.1	12.4	2.6
$MADV$	-3.2	-0.4	-1.4	2.2	0.1
$EADV$	0.1	0.1	5.0	-7.0	-1.1
$MSTR_{1+\frac{1}{2}}$	24.0	-0.9	-21.5	-9.3	-3.9
$ESTR_{1+\frac{1}{2}}$	4.9	0.2	133.3	-95.9	-20.1
$MSTR_{2+\frac{1}{2}}$	-0.6	2.1	24.2	2.5	2.3
$ESTR_{2+\frac{1}{2}}$	-1.8	2.1	-127.0	98.2	20.5
$DISS$	2.6	11.2	0.8	-2.5	0.4

Table VII. Middle layer vorticity budgets for experiment MF. The units of the vorticity tendency terms are $m^3\ s^{-2}$.

From a vorticity viewpoint, it is apparent that the main difference between MF and MT lies in the greater importance of eddy processes in subregions RCIRC, BC1 and BC2. In MF, eddy advection in the top layer is effective at driving deep flows and eddies in the lower layers. The middle layer, while supporting some advection of planetary vorticity, appears mainly as a conduit to the bottom layer. The bot-

	Subregions				
Vorticity terms	INT1	INT2	RCIRC	BC1	BC2
$PADV$	-3.8	-3.9	-73.4	-17.8	-5.7
$MADV$	-0.0	0.0	-4.4	3.9	0.0
$EADV$	0.3	-0.8	-23.5	25.6	5.0
$MSTR_{2+\frac{1}{2}}$	0.6	-2.1	-24.2	-2.5	-2.3
$ESTR_{2+\frac{1}{2}}$	1.8	-2.1	127.0	-98.2	-20.5
$DISS$	0.3	7.7	-2.3	44.3	13.2

Table VIII. Bottom layer vorticity budgets for experiment MF. The units of the vorticity tendency terms are $m^3\ s^{-2}$.

tom layer is much more active in MF and is driven by eddy vortex stretching of the interface. Since the no–slip condition is imposed along the coast, dissipation must be most significant in a frictional sublayer of the boundary current adjacent to the boundary. Subregion BC1 encompasses this inner boundary layer and, also, an inertial boundary layer which includes most of the boundary current.

5.1.2 Energy Budgets

While the vorticity budget analysis readily discloses the nature of the eddy variability in MF, energy budgets are necessary to understand the essential modification to the solution that arises with the introduction of topography. The energy budgets for MT and MF are given in Figs. 29a and b. Considering the latter first, we see that the wind stress curl primarily drives the baroclinic modes. Lateral friction and, to a lesser extent, sponge layer friction dissipate much of the baroclinic energy. There is also a significant nonlinear transfer of energy from the baroclinic modes to the barotropic mode. This transfer is the main source of energy for the barotropic mode. The kinetic energies of the barotropic and first baroclinic modes are comparable. Bottom friction acts preferentially upon the barotropic mode to dissipate energy at a modest rate.

The energy budget of MT shows that the topography has a profound effect

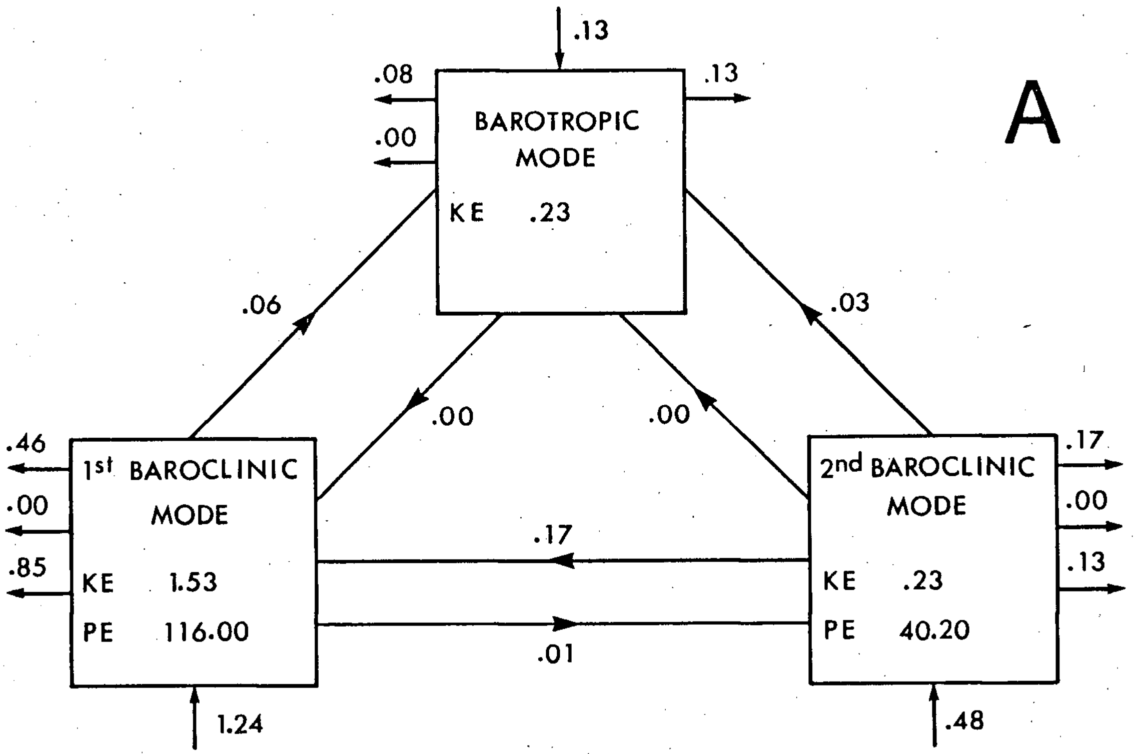

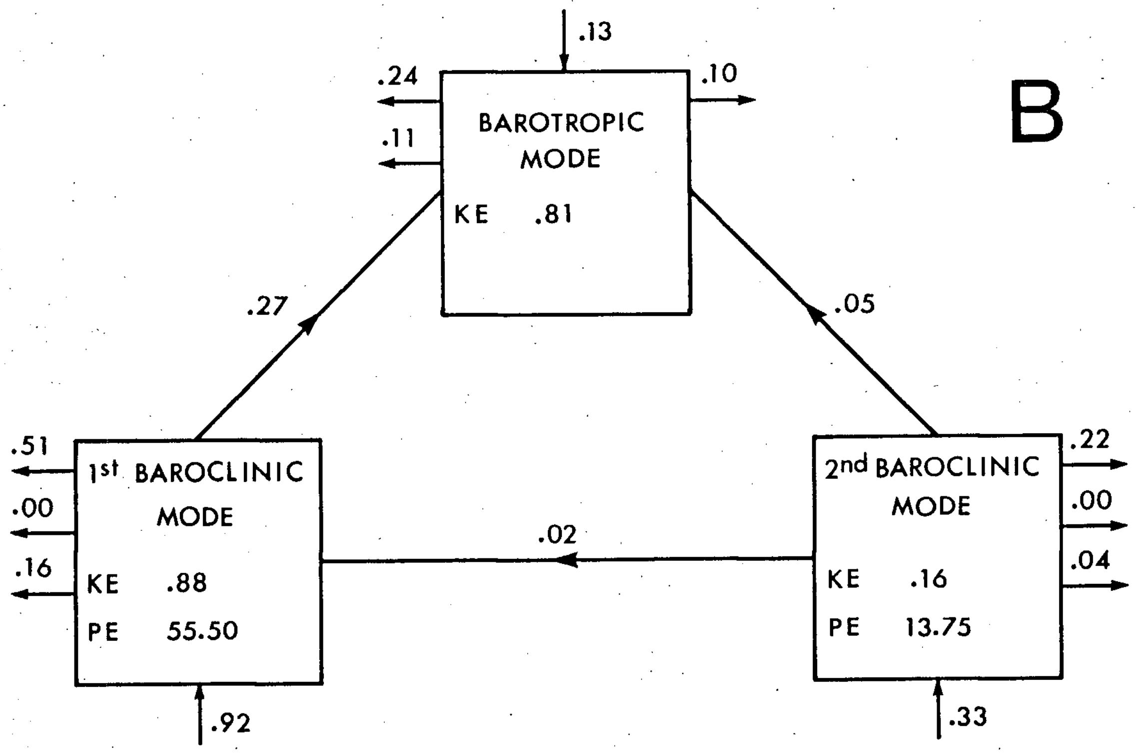

Figure 29. Modal energy budgets for (a) MT and (b) MF. The kinetic (KE) and potential (PE) energies of each mode are in 1×10^3 J m^{-2}. The energy transfer terms are in 1×10^{-3} J m^{-2} s^{-1}. Refer to Fig. 9 for the meaning of the various transfer terms in this figure.

on the energy transfers. The most significant difference with MF is the sharply reduced transfer to the barotropic mode from the baroclinic modes. The efficiency of the transfer from the wind stress curl to the baroclinic modes is also enhanced by the presence of topography. Since barotropic motion is inhibited in MT, the rate of energy loss to bottom friction is also reduced. In contrast, the sponge layer dissipation is increased by a factor of about four in MT. Finally, while the topography very effectively alters the nonlinear transfer between modes, the intermodal energy transfer rate due to the topographic interaction term is negligible.

The barotropic eddies, which are evident in MF, arise, in part, through the release of baroclinic energy to barotropic kinetic energy via baroclinic instability of the mean flow. The topography stabilizes the boundary current and inhibits baroclinic instability, as reflected in the large decrease of the nonlinear energy transfer in MT. Since this leaves the baroclinic modes with a larger mean amplitude at the surface, the efficiency of the forcing to these modes increases. The kinetic energy of the barotropic mode has both a mean and eddy contribution. It is the latter component which increases in MF. The former remains approximately constant in the two experiments, since the barotropic mean flow is essentially determined by the Sverdrup balance. As the mean amplitude of the barotropic mode does not change significantly with the inclusion of topography, there is little change in the efficiency of the wind forcing of this mode.

5.2 Discussion

A few process studies of the influence of bottom topography on stratified quasi–geostrophic turbulence have appeared in the literature and these provide a background for comparison with the energy budgets of MT and MF. Rhines (1977) conducted experiments of free–decaying turbulence in a two–layer doubly periodic domain and found that the principal effect of topography is to reduce the rate of energy loss from the baroclinic mode to the barotropic mode. Thus topography was found to be very effective at inhibiting the process of barotropization, i.e. the cascade of energy to the gravest mode. Treguier and Hua (1989) examined the energy transfers in free–decaying turbulence and showed that, in a flat–bottom configuration, the nonlinear interaction terms transfer energy that is initially in the baroclinic modes to the barotropic mode. This is similar to the situation obtained in experiment MF. With the inclusion of a rough bottom topography in free–decaying turbulence, Treguier and Hua found that the flow remained much more baroclinic. This was not achieved through a reduction of the rate of energy transfer via nonlinear interactions, as in MT, but rather through a topographic energy transfer in the opposite direction, from the barotropic mode to the first baroclinic mode, in contrast to MT where the topographic interaction energy transfer is negligible.

Treguier and Hua also presented results from experiments in which a model with three modes is forced by a stochastic wind in which the time dependence is represented by a Markovian process with an integral time scale of 20 days. In these experiments, the primary energy pathway, in the flat–bottom case, is from the wind to large–scale ($>$ 500 km) barotropic motions and then to dissipation by bottom friction. A secondary pathway is from the wind to the first baroclinic mode, then to small scale ($<$ 500 km) barotropic motions via nonlinear interactions, and finally to dissipation by bottom friction. The introduction of topography leads to a new pathway for the energy: the wind again puts energy mainly into large–scale barotropic motions but topography causes a transfer to the barotropic small scales where most of the energy is dissipated. In their model, the nonlinear transfer from the baroclinic to barotropic motions is reduced slightly in the presence of topography. The efficiency of the wind forcing diminishes somewhat with topography because the smaller scale barotropic motions are correlated more poorly with the wind field.

Additional experimentation is undoubtedly necessary to fully understand the differences between the results of Treguier and Hua with those presented above.

It seems likely, however, that the different time scales of the forcing may be very important. From linear studies (e.g., Veronis and Stommel, 1956) it is known that a low frequency or steady wind will excite mainly the baroclinic modes, whereas a high frequency wind, such as that employed by Treguier and Hua, preferentially excites the barotropic mode. Since the winds are steady in MT and MF, this may explain why the energy transfer from the wind is principally to the baroclinic modes rather than to the barotropic mode, as Treguier and Hua obtained.

As in the present study, these authors found that the intermodal topographic energy transfers are negligible. This is a departure from the free-decaying turbulence case and is also likely due to the presence of forcing. They found that the wind produces a positive correlation between the first two modes at the surface so that the flow is not free to establish the correlation between modes at the bottom. The same situation occurred in MT; fluctuations of the first two modes are correlated at the surface, but they are out of phase at the bottom, thereby preventing the constructive interference which is necessary for an efficient topographic energy transfer. It will be shown in Chapter 7 that, for a smoothed topography, this process is of much greater importance.

6. The Seasonal Cycle

The influence of seasonal variations in the wind field on the oceanic circulation in the Gulf of Alaska is not well established. It is known that there is a very large and significant seasonal cycle to the wind stress curl. For example, Rienecker and Ehret (1988) examined the COADS data and found that seasonal variations account for about 30% of the variance in the wind stress curl over the NE Pacific. However, it is uncertain whether the ocean circulation displays a large seasonal response to this forcing. Reed et al. (1980) found that there was no evidence for a seasonal variation in the baroclinic transport of the Alaskan Stream. Royer (1981) reconsidered the matter and concluded that the data indicated a modest annual signal (about 13% of the mean) in the baroclinic transport. In contrast to this, the primitive equation numerical models of Huang (1979) and Hsieh (1987) displayed a very pronounced annual cycle in the barotropic transport. In these numerical experiments the model Alaskan Gyre virtually disappears during the summer months and reappears at full strength in the fall months. Since variations in the baroclinic transport are thought to be representative of variations in the barotropic transport (Warren and Owens, 1988), the relation between observations of seasonal variability of the gyre circulation and these numerical experiments is problematic.

In this chapter, the seasonal cycle of the wind forcing is incorporated into the numerical model to investigate the influence of this annual oscillation on the oceanic circulation. The results presented above indicate that the barotropic response of the model is very sensitive to the inclusion of topography. Thus two seasonally forced experiments have been run: experiment SF is a flat–bottom model with seasonal forcing, while experiment ST is an identical experiment, save for the inclusion of the topography. The results presented below show that the nature of the seasonal variability of the Alaskan Gyre is profoundly influenced by the inclusion of variable topography. These experiments point to the necessity of including variations in the bottom depth to obtain a realistic simulation of the seasonal cycle of the NE Pacific circulation.

6.1 Results

For the two seasonally forced experiments, the forcing is prescribed from wind stress curl fields derived from the Hellerman and Rosenstein (1983) normal monthly wind stress data. The monthly data were temporally interpolated at each model time step. The same cycle is repeated year after year for the duration of the experiment. On Figs. 30a–d the mean monthly wind fields for the months of January, April, July and October clearly shows the strong annual cycle of the curl field. The cyclonic curl is maximum during the months of October and November and is weakest in August. During the summer months, the zero contour of the curl field shifts northward by some 500 km, to about 50° N. Thus, in experiments ST and SF, the southern part of the domain is forced by an anticylonic wind stress curl during summer. The wind stress curl computations of Rienecker and Ehret (1988), using the COADS data, show a very similar northward shift of the zero curl contour during summer.

The respective initial conditions for experiments ST and SF were the end states of the two steadily forced experiments, MT and MF. An adjustment time of 10 and 6 years, respectively, was allowed for the model to come to equilibrium with the forcing. After this initial period, the two experiments were integrated for ten years during which streamfunction fields were stored at 4 day intervals. Monthly means were formed by averaging together individual months from successive years. The ten-year monthly means are very similar to monthly means computed from the first five years of the integration and thus indicate that the averages are sufficiently stable.

6.1.1 Barotropic Response

Much of the literature devoted to the study of the ocean response at the annual

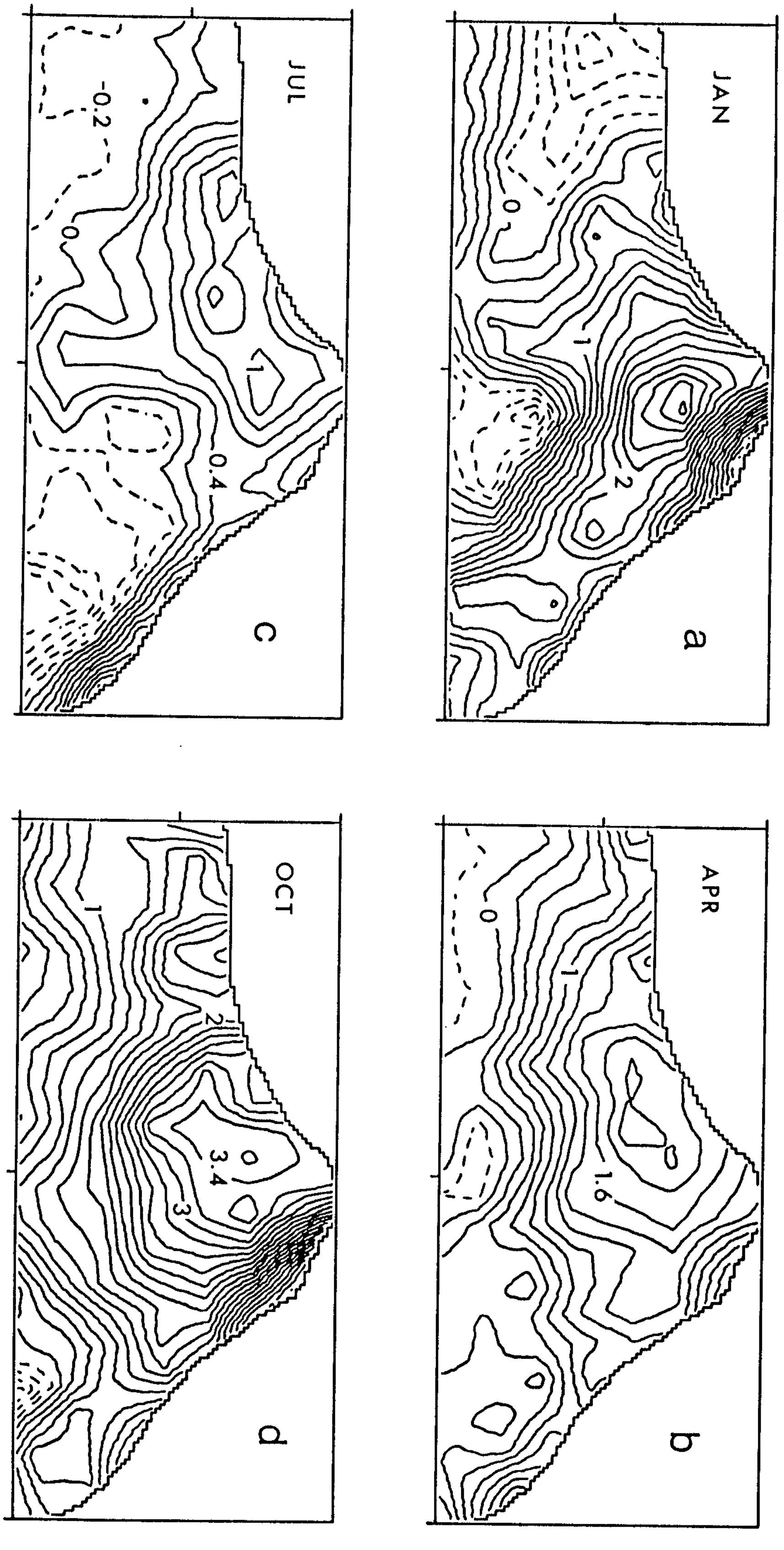

Figure 30. Climatological monthly mean wind stress curl fields interpolated onto the model grid; (a) the January field, (b) April, (c) July and (d) October. The contour interval is 0.2×10^{-7} N m^{-3}. Solid line are for positive contour values while dashed line are for negative contours.

frequency has focused on the determination of seasonal variations in the volume transport. For that reason, the following discussion pertains in large measure to the response of the barotropic mode of the model. Several studies have suggested that an important component of the oceanic response to seasonal wind forcing is the generation of first baroclinic mode annual Rossby waves which propagate into the ocean interior from the eastern boundary (eg. White and Saur (1981), Cummins et al. (1986)). It is important to note that such a response is not possible in the present model since the region under consideration is north of the critical latitude for annual Rossby waves in the North Pacific.

Before consideration is given to the monthly averages, it is worth making a comment on the first and second order statistics of the flow. These fields (i.e. mean streamfunction, eddy kinetic and potential energy) were calculated for the ten-year records of ST and SF and were found to be very similar in both magnitude and spatial distribution to ones from the respective experiments with steady forcing. The one exception to this is that the eddy potential energy fields from ST do not show the maximum found in the southwest part of the domain in MT (Fig. 19). This difference is due to a long adjustment to equilibrium that was not complete before flow statistics were computed for MT. In any case, the comparison between steadily forced and seasonally forced experiments indicates that measures of flow variability, such as EKE or EPE, depend much more on the intrinsic turbulence of the fluid than upon low frequency, deterministic variations in the forcing field. In addtion, the modal energy budgets for experiments SF and ST (not shown) are very similar to the budgets of the respective steadily forced cases. Thus, the energy budgets are also insensitive to the inclusion of low frequency forcing.

A comparison between the monthly means of experiments ST and SF is presented in Figs. 31a–h. Four months of each are included to show the progression of the annual cycle. The time sequence from ST shows that there is a weakening of the intensity of the gyre from April to July. This is followed by a reintensification in the fall months. The amplitude of the transport variation (one half of the peak-to-peak difference) is about 2.5 Sv or about 13% of the total mean transport. The cyclonic gyre which is found adjacent to the western boundary, in the January frame, shifts progressively westward during the first half of the year, so that, by July, it is some 150-250 km from the eastern boundary. In the wake of this westward shift, a series of eddies of alternating rotation appear along the eastern boundary. These eddies first emerge during the spring months and remain until the cyclonic Alaskan Gyre has shifted to the east, in the fall.

Two additional facets of the monthly transport fields are worth mentioning. First, the flow in proximity of the southern boundary remains cyclonic during the entire model year in spite of the anticyclonic forcing present there during the summer months. Secondly, the boundary current maintains its integrity throughout the entire model year. The most apparent seasonal variation associated with the model Alaskan Stream is that its point of origin shifts southwestward along the boundary during the summer months.

The seasonal variation of volume transport in the flat bottom case, SF, is substantially different than in ST. Most significantly, the amplitude of the seasonal cycle is much larger in SF, with the amplitude of the seasonal variation in volume transport being now 75–80% of the mean. The maximum transport occurs in October and reaches some 35 Sv. In the summer months of July and August the gyre is weak and barely discernable amid the series of cyclonic eddies that arise in the boundary current. There is also a much greater westward shift of the gyre (cf the April field with that of January.) The appearance during the summer months of a weak anticyclonic gyre near the southern boundary in direct response to the anticyclonic forcing there.

To further illustrate the seasonal variability, time series of the volume transport

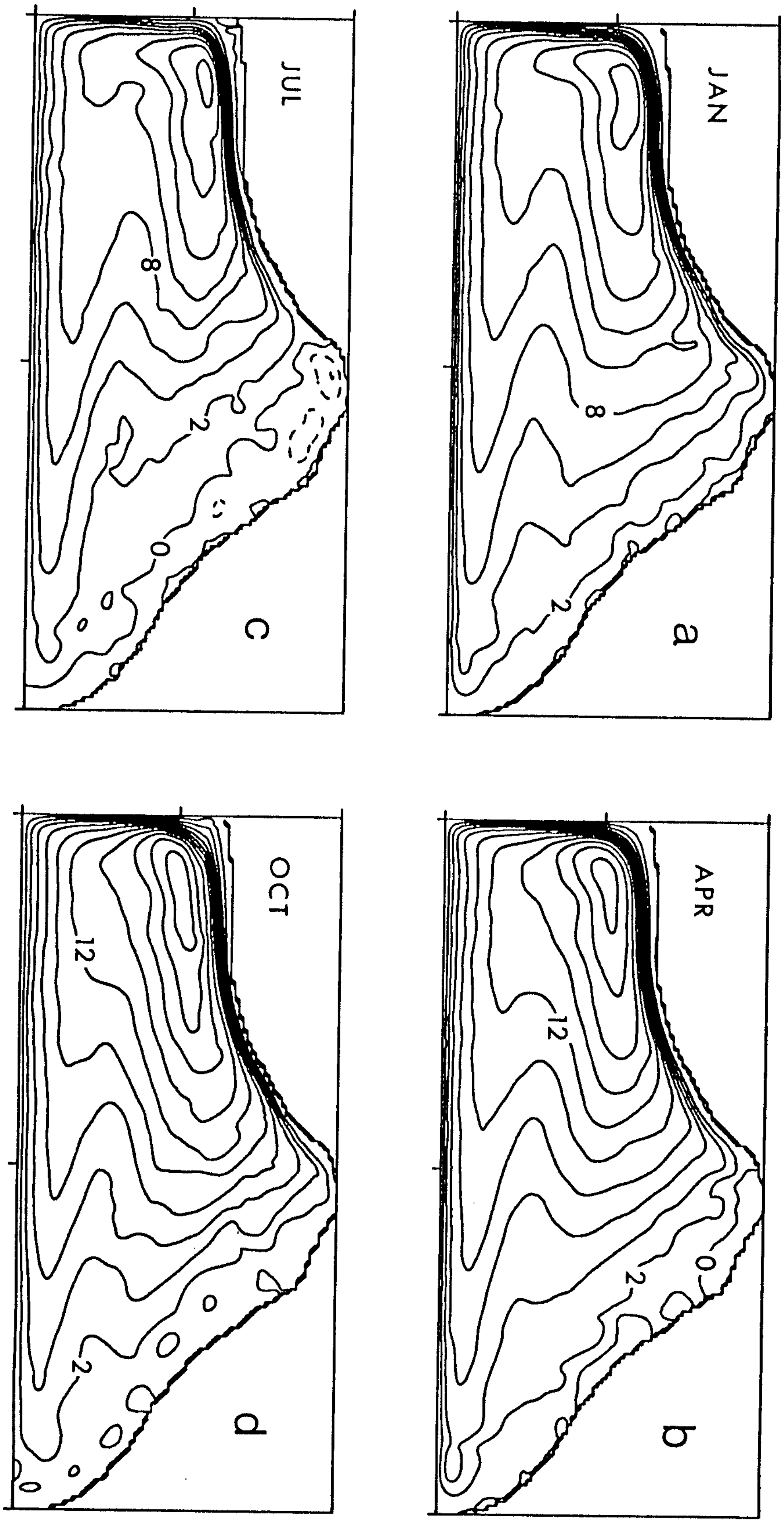

Figure 31. Transport streamfunction fields from experiments ST (a–d) and SF (e–h) for the months of January, April, July and October. (CI = 2×10^6 m^3 s^{-1}.)

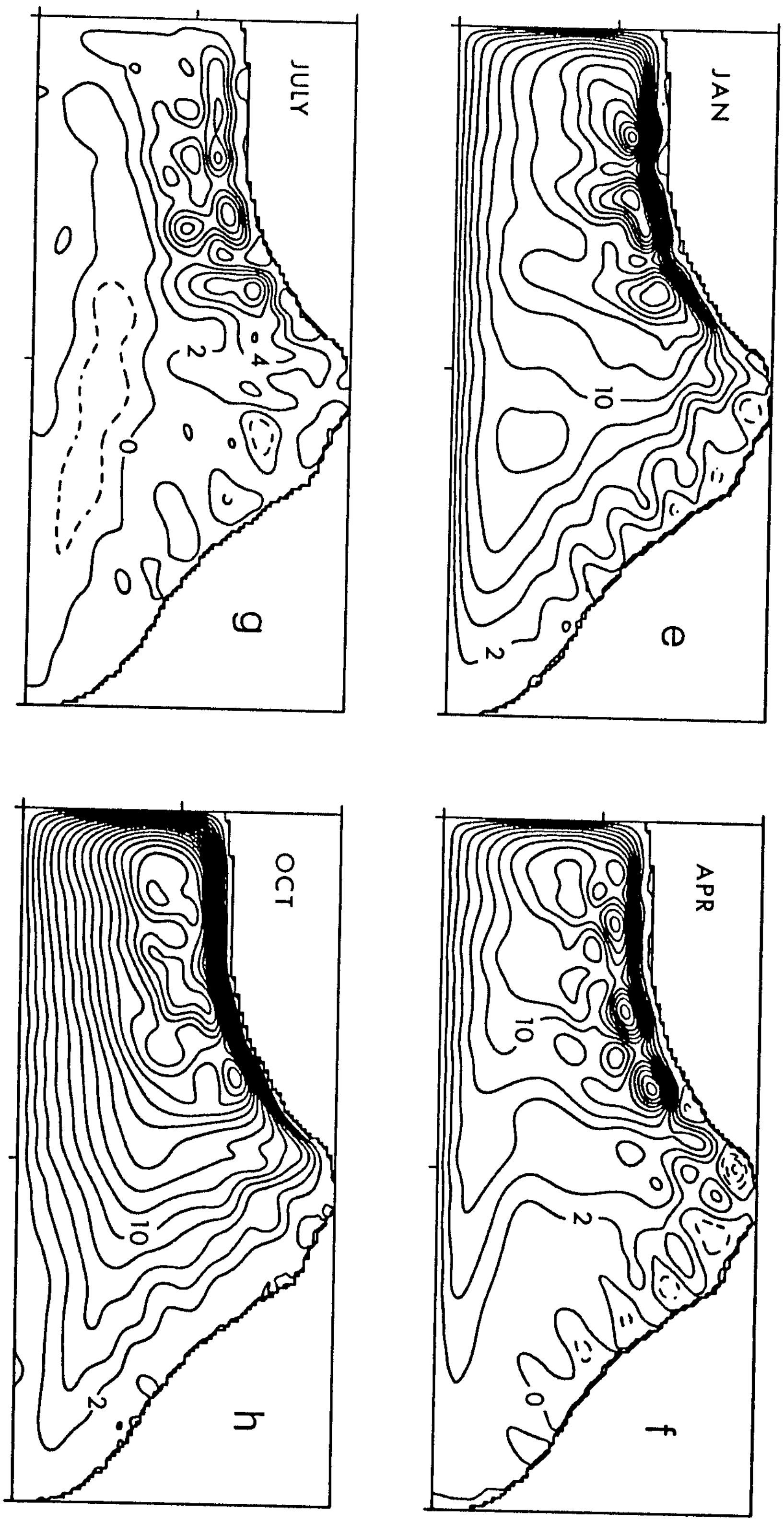

Figure 31 continued.

are shown in Fig. 32a–b. The transport between the boundary and certain points within the domain is plotted here as a function of time. (The uppermost time series gives the magnitude of the maximum volume transport occurring in the domain. The location of the point of maximum transport will, of course, vary with time.) In ST, a relatively modest variation in the gyre transport occurs. The maximum transport is almost identical to the Aleutian Rise transport. Except for the time series taken from a point in the boundary current (near Kodiak Island), the time series show a very regular repetition from one year to the next. The Kodiak Island time series shows much greater variability due to the passage of perturbations and lateral meanders in the model Alaskan Stream.

The time series from SF show much larger transport variations and also major changes in the gyre intensity occurring on comparatively short time scales. The annual cycle is generally discernable but there is considerable interannual variablity as well. On the top panel, the maximum transport fluctuates about a mean of 40 Sv, because the point of maximum transport invariably occurs within the centre of a strong cyclonic eddy. This accounts for the major difference between this time series and that for the Aleutian Rise. The latter is the most representative of the overall gyre intensity in both experiments.

Power spectra of modal streamfunction fluctuations were computed for ST and SF. A comparison of spectra for the two experiments at a point located in the model Alaska Current is shown in Fig. 33. For the ST spectra, a peak at the annual harmonic is present in each mode, over much of the domain. The first baroclinic mode spectra also indicate the presence of motions with longer interannual time scales as well as several higher harmonics (i.e. at the semiannual and quarterly frequencies.) Spectra computed from locations off the Aleutian Islands in the model Alaskan Stream (not shown) contain the high frequency topographic wave signature present in MT and described in Chapter 4. The barotropic mode spectra from SF

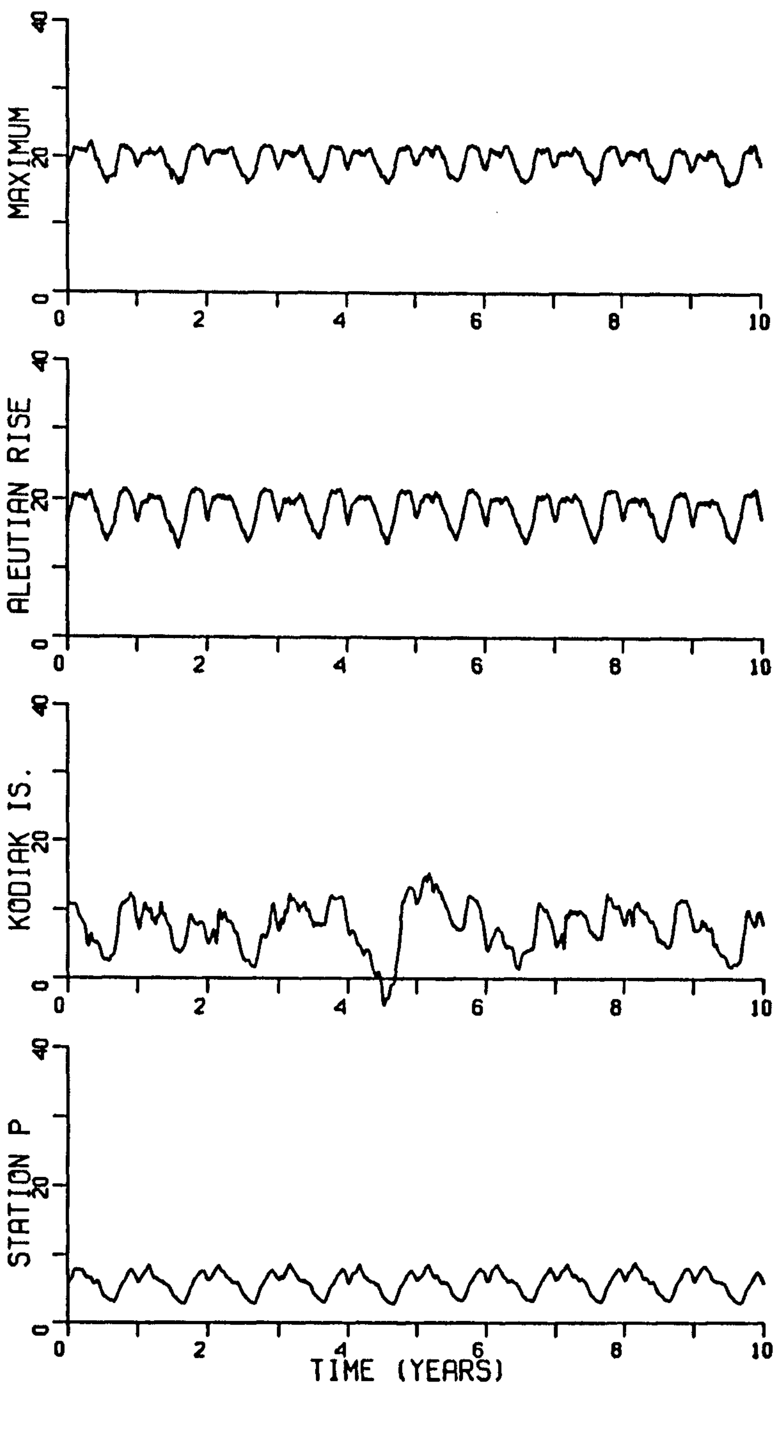

Figure 32. Time series of volume transport between selected locations in the model domain and the boundary for (a) experiment ST and (b) experiment SF. Positive values are for cyclonic transport. The time series labelled 'maximum' gives the variation of the maximum transport found within the domain with respect to the boundary. The location at which this maximum occurs is time-dependent. The 'Aleutian Rise', 'Kodiak Island' and 'Station P' time series are taken from fixed points marked **A**, **K** and **P** respectively on Fig. 27c.

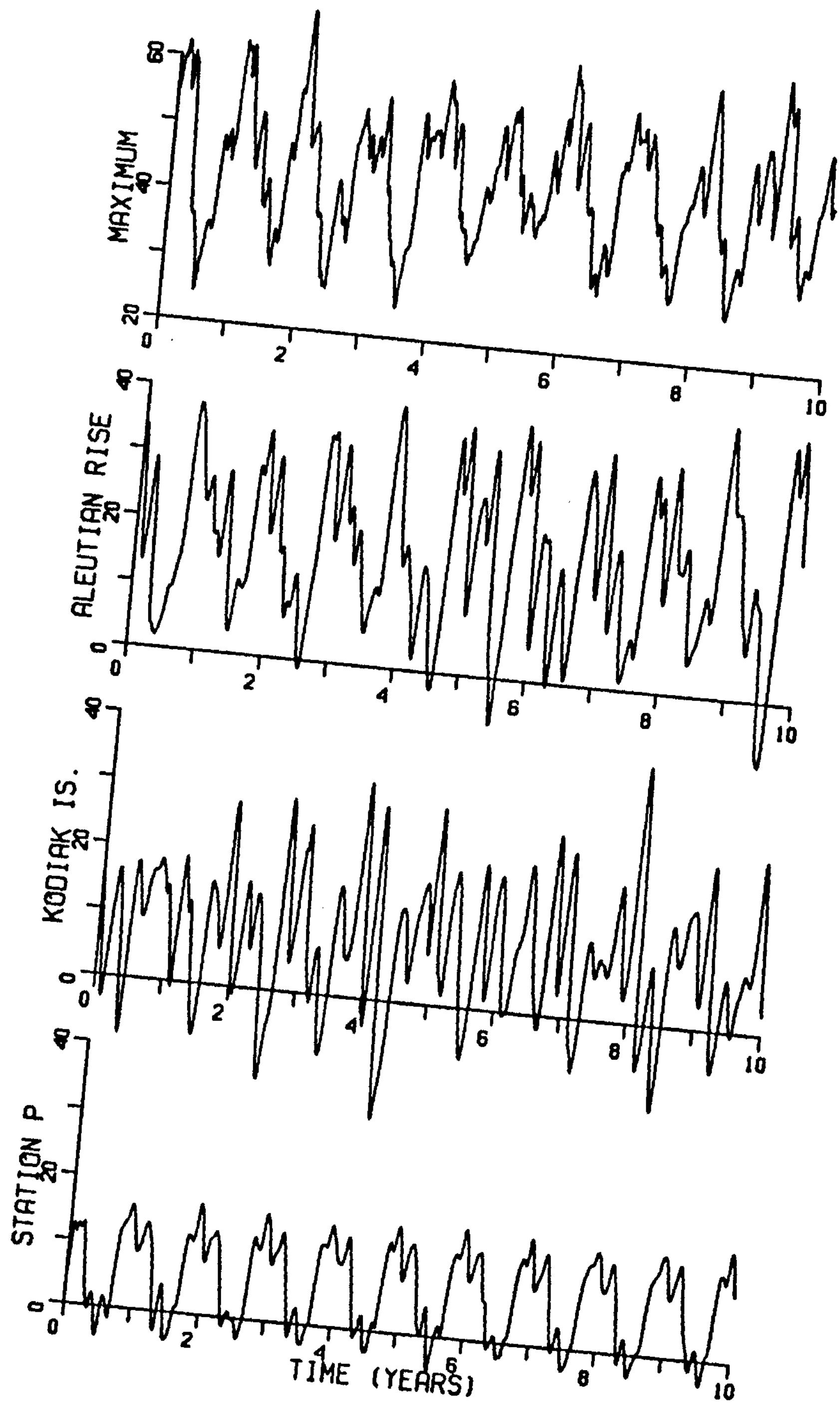

Figure 32 continued.

also has a peak at the annual frequency and at higher harmonics. Over most of the domain, the barotropic mode is the most energetic and dominates over the baroclinic modes. The barotropic mode here is much larger than in ST. In addition to the annual harmonic, there is the ubiquitous peak at the mesoscale eddy period (about 100 days). This is the counterpart to the spectral peak from MF shown in Fig. 28d and it is present in spectra from the three modes. Higher harmonics, such as the quarterly cycle, are often obscured by the eddy peak.

6.1.2 Eof Analysis

The application of an empirical orthogonal function (eof) analysis to the seasonally forced experiments is a particularly useful way of revealing the different spatial modes of variability in the solution. The technique is applied to the modal eddy streamfunction fields, $\phi'_m(\mathbf{x},t)$, of experiments ST and SF. In this analysis, the $\phi'_m(\mathbf{x},t)$ are expanded in a series of orthogonal basis functions, $e^n_m(\mathbf{x})$, such that

$$\phi'_m(\mathbf{x},t) = \sum_{n=1}^{N} a^n_m(t)\; e^n_m(\mathbf{x}) \tag{6.1}$$

The $e^n_m(\mathbf{x})$ are solutions of the eigenvector problem,

$$\sum_i R^m_{i,j} e^n_m(\mathbf{x}_i) = \lambda^n_m\; e^n_m(\mathbf{x}_j), \tag{6.2}$$

where the spatial covariance matrix, $R^m_{i,j}$, is given by

$$R^m_{i,j} = \overline{\phi'_m(\mathbf{x}_i,t)\,\phi'_m(\mathbf{x}_j,t)}. \tag{6.3}$$

The overbar indicates a time average, which in our calculation is done over ten years. It may be shown that the ratio of an individual eigenvalue, λ^n_m, to the sum of eigenvalues gives the percentage of the total variance accounted for by the associated eof. The time–dependent amplitude of each eof, $a^n_m(t)$, is obtained from

$$a^n_m(t) = \sum_i \phi'_m(\mathbf{x}_i,t)\, e^n_m(\mathbf{x}_i). \tag{6.4}$$

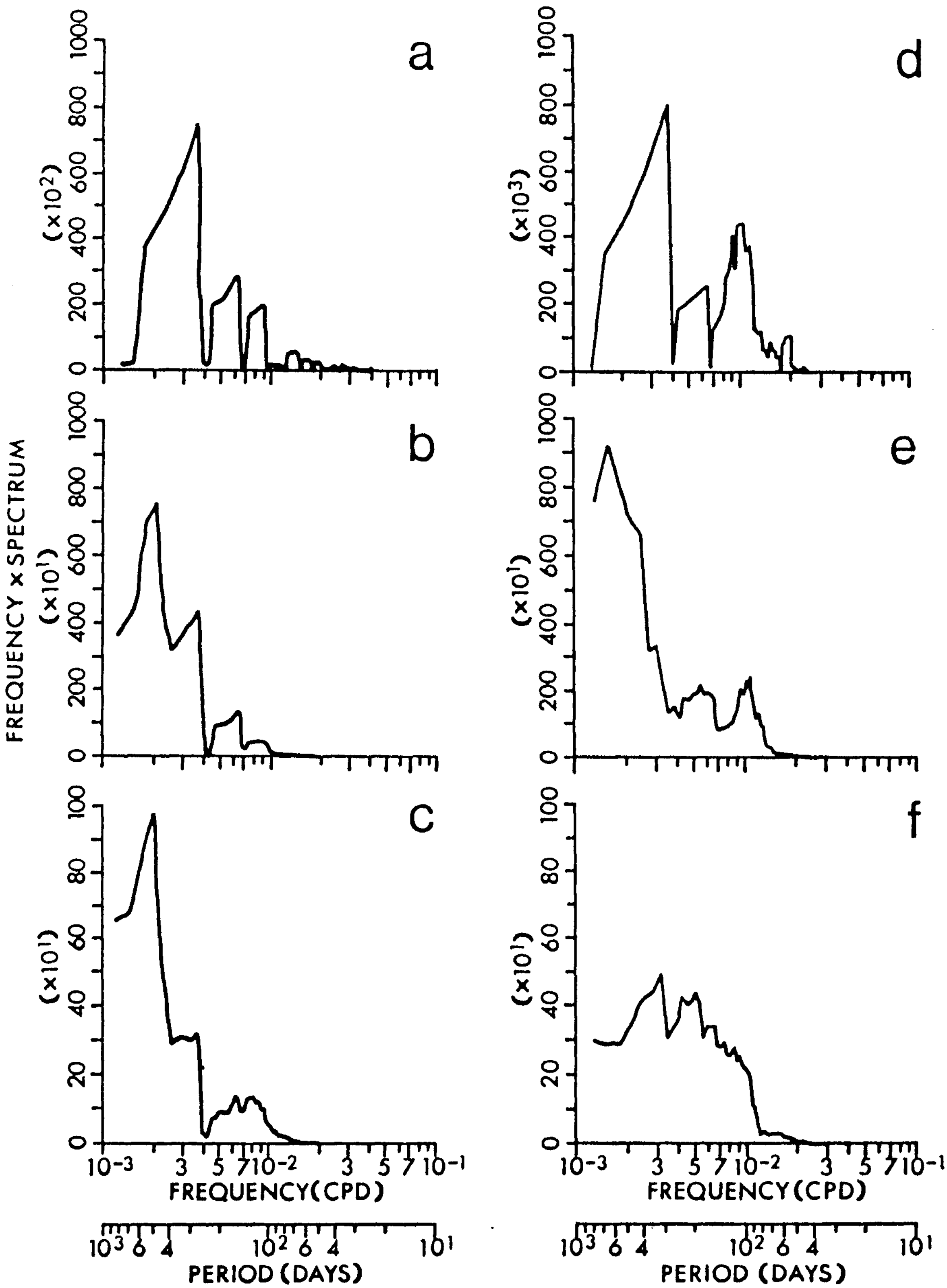

Figure 33. Variance–preserving autospectra of modal streamfunction fluctuations at a point near the domain center (marked by the bold dot in Fig. 26a) from experiment ST: (a) the barotropic mode, (b) the first baroclinic mode and (c) the second baroclinic mode. The corresponding spectra from SF are shown in (d–f). Note that the barotropic mode spectra have different vertical scales. Units are cpd $\times$ $\left(\frac{\mathrm{m}^4\ \mathrm{s}^{-2}}{\mathrm{cpd}}\right)$.

The computation of the eofs was done first with the grid subsampled at an 80 km interval in the x and y directions, and then at a 100 km interval. The most significant eofs differed very little between the two calculations indicating a sufficient resolution for our purposes. Only results from the 80 km case for the barotropic and first baroclinic modes are considered below. The eofs from the second baroclinic mode are omitted since they exhibit smaller scale structures which are difficult to interpret. Also, for this higher mode, much of the variance is spread over a considerably larger number of eofs.

The eofs are constructed from 10–year time series with 900 points in time and 511 points in space (80 km resolution). From these sample sizes, the significance of the eofs may be estimated by the application of a dominant–variance rule (Rule N), given in Preisendorfer and Mobley (1988, page 199). This analysis indicates that eofs accounting for less than 0.6% of the variance are not significant at the 100% confidence level. The variances of all the eofs discussed below are well above this significance level.

The five most significant eofs of the barotropic mode from experiment SF are first shown in Fig. 34, with eof no. 1 accounting for about half of the variance of the barotropic mode. The accompanying time series plot shows that this eof oscillates at the annual frequency. The spatial pattern of the eof describes a cyclonic basin–wide circulation in fall–winter, and a reversed anticyclonic circulation in spring–summer. As such, this represents a periodic weakening and intensification of the mean cyclonic gyre.

The next two eofs (2 and 3) must be considered together since they describe the same mode of motion. The eof analysis here has isolated the westward propagation of barotropic Rossby waves along the Aleutian Arc western boundary. These two eofs account for 18% of the variability in SF. Phase propagation can be inferred from the spatial patterns and the time series which both show a phase shift of 90°

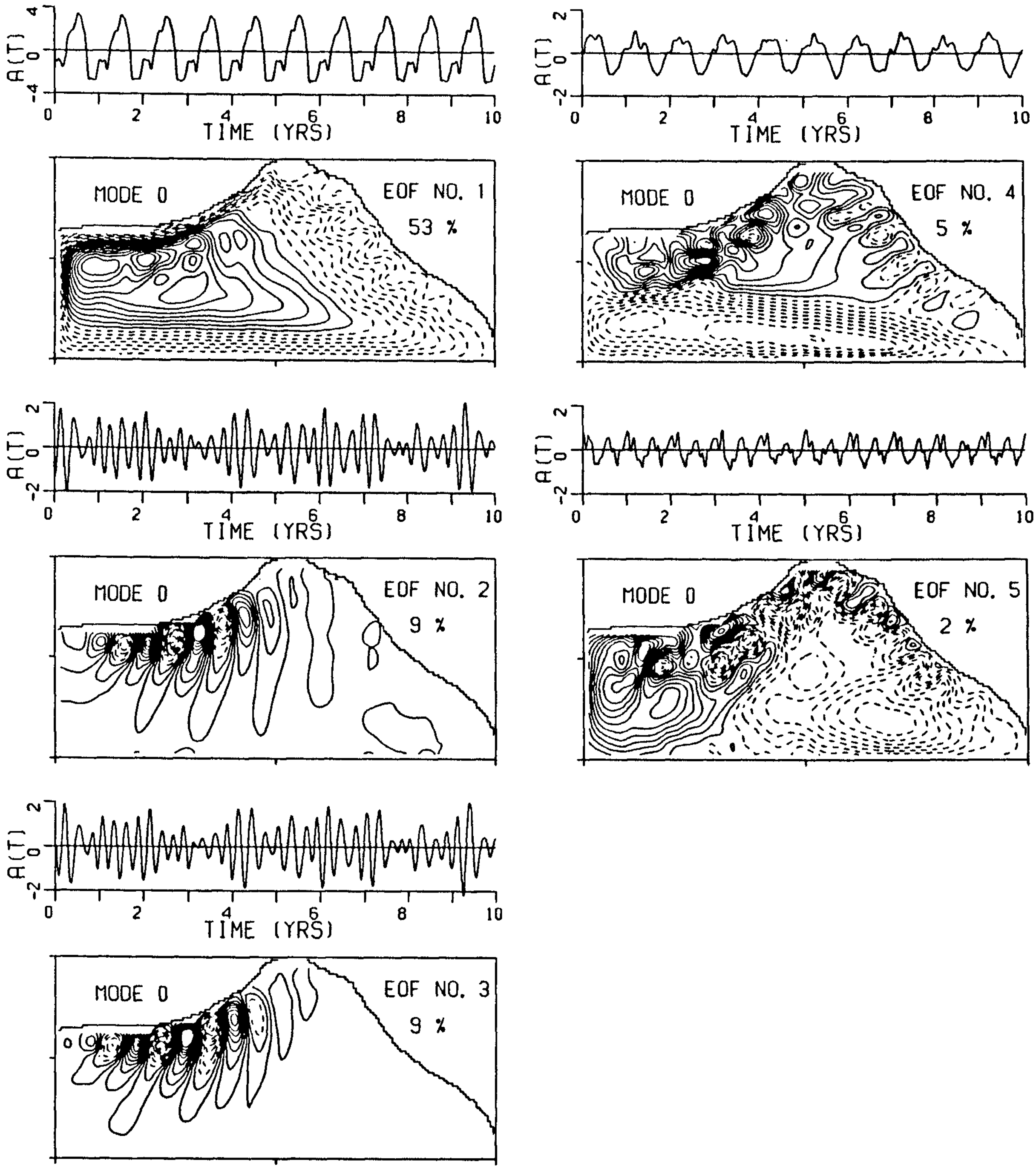

Figure 34. The five most significant eofs of the barotropic mode fluctuations from experiment SF. The percentage value indicates the fraction of the total variance explained by the eof. The time series for these eofs and those that follow are in units of 10^4 m^2 s^{-1}.

between the two eofs. The approximate wavelength and period of the waves is 330 km and 100 days respectively. This closely satisfies the dispersion relation for zonally propagating barotropic Rossby waves, $\omega = -\beta k^{-1}$. The inferred phase speed is 3.3 km day^{-1}. It is clear from the dominant period of the time series that eofs 2 and 3 on Fig. 34 are associated with the mesoscale eddy peak that is prominent in the spectra discussed above. An eof analysis of experiment MF showed that a similar pair of eofs describing barotropic Rossby wave propagation were also present in that experiment. However, in MF, there is no seasonal variability. Consequently the wave propagation eofs account for a larger fraction (40%) of the total variance of that experiment.

Eofs four and five on Fig. 34 account for only a small portion of the variance, 5% and 2% respectively. They primarily represent changes in the position of the gyre. The fourth one shows a north–south oscillation of the gyre at the annual frequency, while the fifth one displays an east–west oscillation at mainly the semiannual frequency.

Next, the five most significant eofs of the first baroclinic mode from SF are shown in Fig. 35. Here, the variance is spread over a much larger number of eofs with the first five eofs accounting for only 30% of the variance. The three most significant, responsible for about a fifth of the variability, describe the propagation of eddies with a period of about 100 days along the western boundary. This corresponds clearly, with the baroclinic component, to the mesoscale eddy peak in the frequency spectra. Eof 4 has a dominant period of one year and shows an eddy field with a wavelength of 250–300 km along the eastern boundary. This likely corresponds to the generation of eddies in the wake of a westward shift of the eastern extent of the cyclonic gyre during the summer months.

Interestingly, this sequence of baroclinic mode eofs does not show the occurrence of any gyre scale baroclinic circulation corresponding to the dominant eof of the

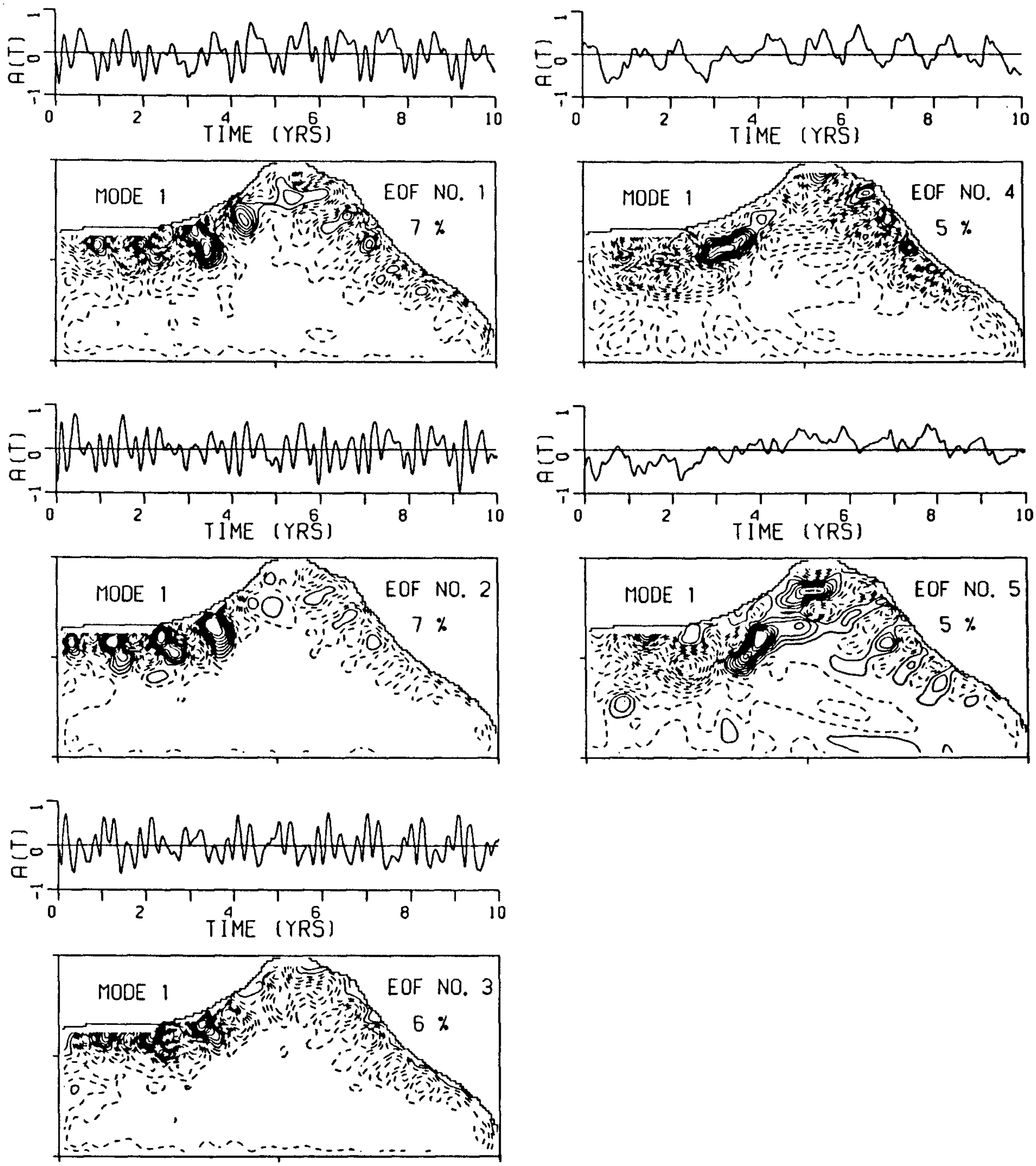

Figure 35. The five most significant eofs of the first baroclinic mode fluctuations from experiment SF.

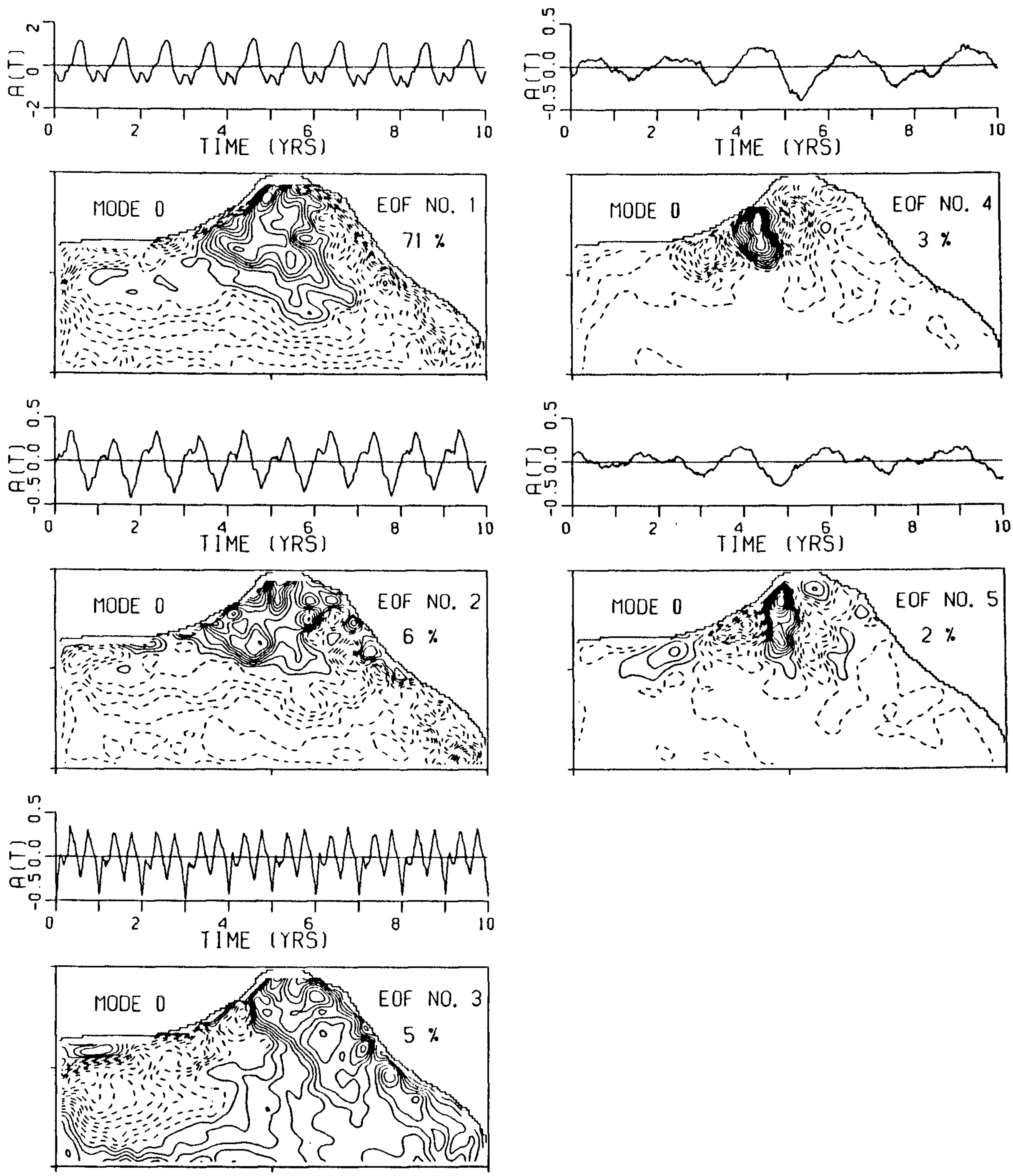

Figure 36. The five most significant eofs of the barotropic mode fluctuations from experiment ST.

barotropic mode. The periodic intensification and weakening of the model Alaskan Gyre is a phenomenon associated with the barotropic mode. This is understandable, since baroclinic Rossby waves of annual period are not among the permissible modes of motion in the Gulf of Alaska.

The eofs computed from ST reveal some of the modifications to the variability of the model when bottom topography is included. Fig. 36 shows the five most energetic eofs of the barotropic mode. The first eof corresponds in some sense to the most significant barotropic mode eof from SF, and also describes an intensification and weakening of the gyre at the annual frequency. Although this eof accounts for over 70% of the variability of this mode, the amplitude of the annual harmonic is smaller by approximately a factor of 3 than its counterpart from SF. This was as expected since, as stated earlier, the annual cycle in the barotropic transport is much weaker in ST.

Eofs two and three account for 6% and 5% of the variance and describe north–south and east–west oscillations of the gyre at the annual frequency and semiannual frequency respectively. As such they are smaller amplitude counterparts to barotropic mode eofs four and five from SF. The fourth and fifth eofs describe a signal propagating around the head of the Gulf with a wavelength of about 600 km and a period of roughly two years. Since the longest period of the wind forcing is one year, this signal must be generated through a nonlinear interaction. It is also coupled, possibly through the topographic interaction term (eqn. 3.16), to a similar oscillation of the first baroclinic mode.

Lastly, the five most significant first baroclinic mode eofs of ST are shown in Fig. 37. Here the variance in the baroclinic modes is again spread over a larger number of eofs than in the barotropic mode. The first five eofs account for about 50% of the variance compared to 87% for the barotropic mode. The most significant of these, accounting for 16% of the variance, is characterized by a series of alternating highs and lows along the eastern boundary oscillating at the annual frequency. The second and third eofs, which together account for a quarter of the variance of the first baroclinic mode, appear to be the baroclinic component to the propagating, interannual period signal found in the fourth and fifth eofs of the barotropic mode.

6.2 Discussion

The results presented above demonstrate that the inclusion of bottom topography leads to very significant modifications in the response of the circulation model to steady and seasonal forcing. In the experiments with steady forcing, topography causes a redistribution of energy among the vertical modes. Specifically, topography inhibits the transfer of energy to the barotropic mode so that fluctuations are now predominantly in the first baroclinic mode. One consequence is the elimination the most energetic signal in the flat–bottom solution, namely the mesoscale eddies with a time scale of 100 days associated with barotropic Rossby wave propagation. Topography also appears to introduce new modes of low frequency interannual variability as illustrated by eofs 2 and 3 of Fig. 37.

With the introduction of seasonal forcing, the flat–bottom model responds with very substantial seasonal variations in the intensity of the barotropic circulation. In this case, the gyre collapses in the summer months with the southern region of the domain developing anticyclonic motion in direct response to the local forcing. The inclusion of topography leads to a severe attenuation of this annual oscillation. The influence of the seasonal forcing on the depth–integrated flow is reduced to a modest cycle in the eastern extent of the gyre and an oscillation in the point of origin of the Alaskan Stream.

In experiment ST, as in experiment MT, the time–averaged flow of the top two layers over the interior is in a nontopographic Sverdrup balance. Thus, over the interior, the vorticity tendency associated with northward transport in these two layers balances the wind stress curl. Because, the bottom layer contributes very little

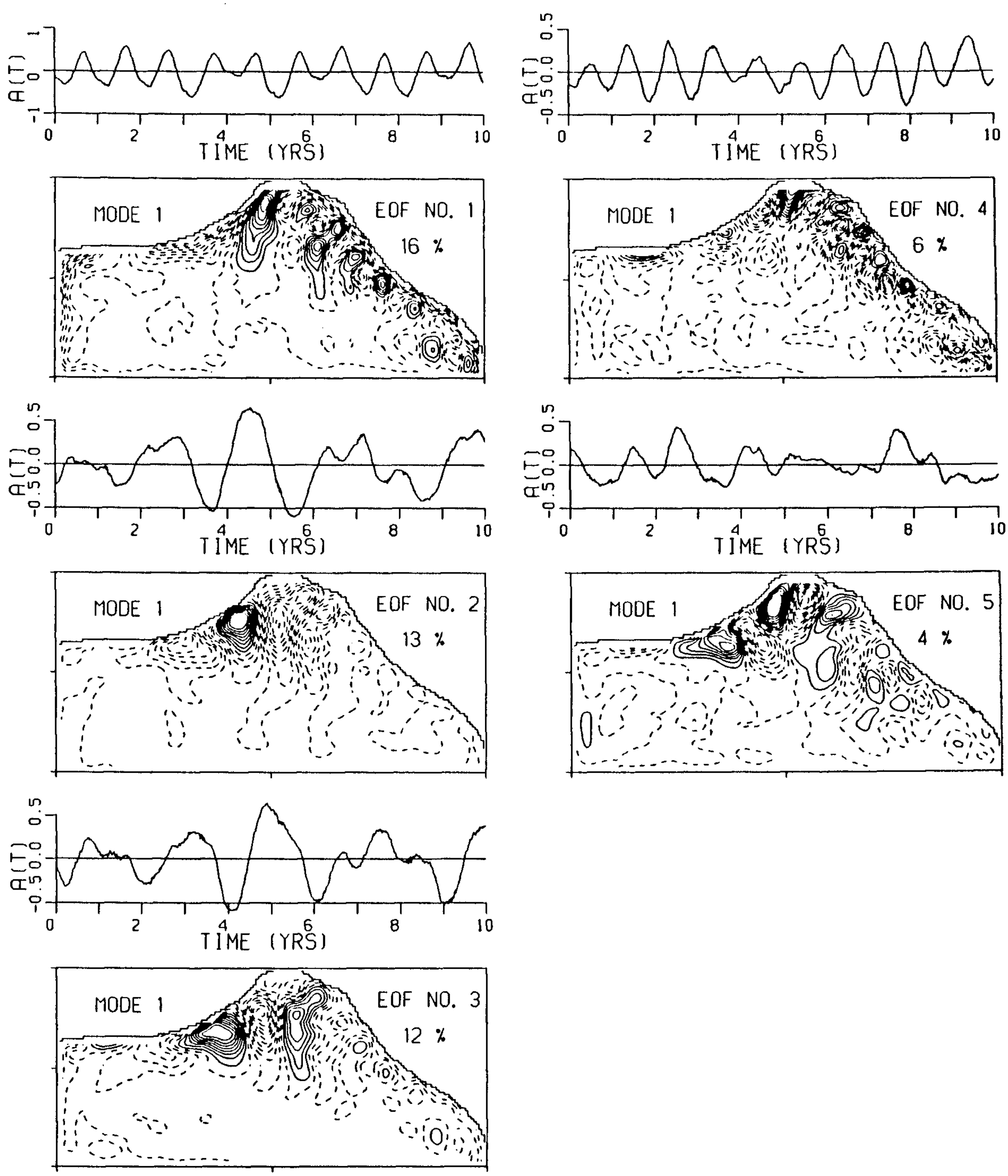

Figure 37. The five most significant eofs of the first baroclinic mode fluctuations from experiment ST.

to the mean transport, the depth–integrated time–averaged interior flow is not much affected by the topography. However, it is clear that the *instantaneous* flow in experiment ST is not in a nontopographic Sverdrup balance with the forcing. As Anderson and Corry (1985) point out, this result is useful for interpreting the weak response to seasonal forcing when topography is present. They show that the Sverdrup balance is established in response to changes in the wind forcing, through the passage of a baroclinic Rossby wave originating from the eastern boundary. The nontopographic Sverdrup balance will not be established if the period of the forcing is much shorter than the time required for the wave to travel well into the interior. Then, in lieu of a time–dependent nontopographic Sverdrup balance, the flow responds as a homogeneous fluid, which is strongly modified by the topography. Since the time required for the passage of the baroclinic wave is of the order of ten years, the annual time scale of the forcing in experiment ST is too short for the establishment of the nontopographic Sverdrup balance over the interior.

Considered in the light of available observations, the seasonal cycle of the model with topography appears to be more realistic than that of the flat–bottom model. Hydrographic data collected from Line P (Tabata, 1989) or from sections across the Alaskan Stream (Reed, 1984) fail to show substantial seasonal variations in the baroclinic transport of the gyre. Current meter data from the Alaskan Stream (Warren and Owens, 1985) do not show any marked seasonality either. Royer (1981) estimated that the seasonal variation in the baroclinic transport of the Stream relative to the 1500 db level was about 13% of the mean with the maximum in March and the minimum in August. Although the seasonal variation in the barotropic transport has not been estimated from field data, it seems likely that estimates of seasonal variations in the baroclinic transport relative to the 1500 db level are representative. Reed et al. (1980) found that the use of deeper reference levels simply augments the volume estimate. A consistent result was obtained by Warren and Owens (1988), who find that the Alaskan Stream extends down to the sea floor without flow reversals at depth. So it seems reasonable to suppose a relative modest seasonal cycle of the order of perhaps 15% in the gyre transport, with the maximum occurring in March–April and the minimum in August–September. This is consistent with the amplitude and phase of the transport variation found in ST, but not in SF.

From hydrographic sections taken over the NE Pacific during July and August of 1981, Royer and Emery (1987) found that a major change in the location of the Alaskan Gyre had occurred. The gyre center was shifted westward by some 700 km and, east of 145°W, there was a cessation of the usual northward flow of the Alaska Current. These unusual conditions are believed to have persisted for at least one or two months. Because this situation has been observed only infrequently (the only other known instance was in the summer of 1958), this anomalous behaviour of the subarctic gyre is usually referred to as 'interannual variability' of the circulation. The nature and causes of these changes is largely a matter of speculation at present.

Reed (1984) suggested that the anomalous conditions were the result of unusually weak wind stress curl forcing over the Gulf region in the three months or so prior to the time of his observations. Royer and Emery (1987) dispute this explanation and offer an alternative one. They suggest that an interaction of the flow with a group of seamounts found near 51°N and 145°W occurs. The latitudinal position of the N. Pacific Current, which feeds into the northward flowing Alaska Current, is the controlling factor in this scheme. If the westward flowing N. Pacific Current is located sufficiently far north, the seamounts are thought to deflect it such that the northward flow of the Alaska Current lies now to the west of the seamount region. In the more usual case the N. Pacific Current flows further south and is not deflected, so that northward flow occurs to the east of the seamount region.

The present series of experiments do not permit definitive statements on the nature of the interannual variability of the subarctic gyre. However, the east–west seasonal excursions of the eastern boundary of the model gyre in experiment ST are suggestive of the interannual variability found in the observations. Thus it seems plausible that these interannual variations are simply an amplification of the regular seasonal variations. The east–west shifts in the eastern boundary of the model gyre are the result of variations in the integrated strength of the wind stress curl over the Gulf. Therefore our results are at least consistent with Reed's hypothesis that the large interannual shifts in the gyre position arise from an anomalously weak wind stress curl field over the Gulf.

The present results appear to have important implications for future modelling studies of the Gulf of Alaska. The numerical studies of Huang (1979) and Hsieh (1987) both show variations in the position and intensity of the Alaskan Gyre in response to seasonal forcing which are very similar to the solution of SF. This is much as expected since Huang's model is a flat–bottom one and Hsieh's model retains only some shelf topography and is essentially flat–bottomed over the interior. It is useful to recall that the major feature of the topography of the NE Pacific is a progressive shoaling of the bottom to the northeast. The resolution of such a feature in a primitive equation model, such the one of Cox (1984) used by Hsieh, presents a very substantial demand on the vertical resolution. This model includes topography in step–like fashion and the bottom is constrained to lie at an interface between two levels. Thus a large number of vertical levels are required to properly resolve a steadily sloping bottom. In Hsieh's model, there are five levels which are spaced unevenly throughout the water column. The bottom layer is over 3 km thick, so there is no resolution of bottom topography beyond the continental shelf. The failure to resolve variations in the bottom depth may well account for the dramatic changes in the gyre circulation that he obtained. The experimental results examined above unambiguously demonstrate the importance of bottom bathmetry to the vertical structure of the numerical solution and to the seasonal response, in the context of a QG model. The limitations of the present model warrant further experimentation in the context of a more general primitive equation model to completely assess the topographic influence. This will likely require much greater vertical resolution than in previous models.

7. Additional Experiments

The experiments considered in this chapter are intended to examine the sensitivity of the solution, described in Chapter 4, to some of the finer details of the model. While the results presented herein do not constitute a complete parameter sensitivity study, they do give some indication of changes to the reference solution that can be expected with a change in the model parameters. The results of three experiments are presented. In the first experiment, MT–BH, the Laplacian friction is replaced with biharmonic friction, in order to examine the effect of a scale–selective parameterization of the sub–grid scale on the model response. The second experiment, MT–SL, is designed to test the effect of a variation in the strength of the sponge layer friction. The third and final experiment, MT–ST, uses a smoothed field of bottom topography. The comparison of this experiment with MT allows a preliminary investigation into the influence of small scale bathymetry on the process of barotropization. The three experiments described below are all forced with the same steady wind stress curl field (Fig. 10) as in MT. The end state of MT is the initial condition for each of the three experiments. In each case, an adjustment time of a few years elapsed before data for a ten–year period were stored on tape. The description of the experimental results in this chapter is not as complete as in chapters 4 and 5, but rather focuses on the salient differences in the solutions.

7.1 Biharmonic Friction

Experiment MT–BH is identical to MT, but with biharmonic friction ($p = 6$ in equation 3.1) used to parameterize the subgrid scales and to absorb grid–scale variance. The viscosity coefficient, A_H, was set to -2×10^{10} m^4 s^{-1}. As a spatial filter, biharmonic friction rolls off more sharply near the grid scale than Laplacian friction, while leaving larger scales less damped. As a result, it is reasonable to expect greater eddy activity with the biharmonic operator. This is confirmed in MT–BH. A map of the instantaneous top layer streamfunction from Day 724 of experiment MT–BH is shown in Fig. 38. A comparison with a similar map from MT (e.g., Fig. 12a) demonstrates that, over the Alaska Current region, the streamfunction field now has considerably greater spatial structure, with more frequent occurrence of ring-like features within the Alaska Current. The spatial characteristics of the Alaskan Stream, however, do not show any marked change from MT. The Stream remains a narrow continuous current, constrained by the Aleutian Trench, and perturbed by topographic waves. The modal energy transfers (Fig. 39) tell essentially the same story as they do in MT; there are no qualitative differences, between the two experiments, in the nature of the energy transfers.

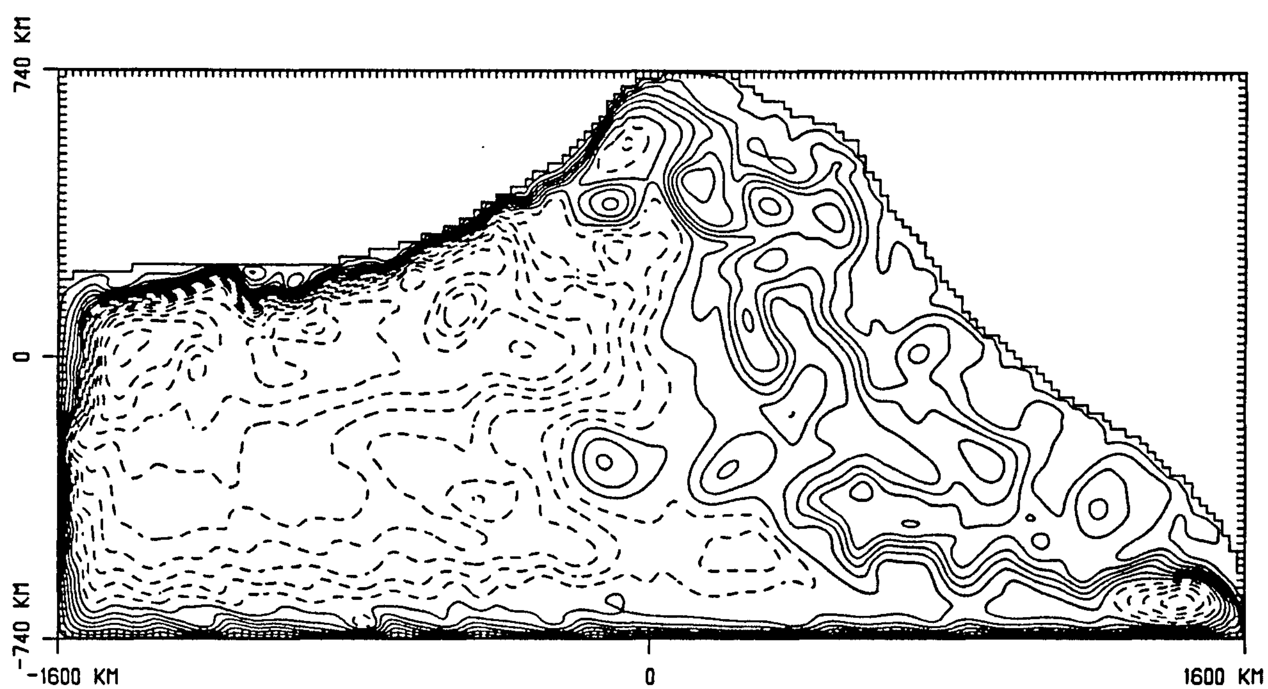

Figure 38. The instantaneous top layer streamfunction field on Day 724 from MT–BH (CI=3000 m^2 s^{-1}).

The gyre transport and mean particle speeds in MT–BH are very similar to those of MT, suggesting that the Sverdrup flow implied by the wind stress curl forcing is the dominant factor establishing these quantities. One obvious difference between the two experiments is in the behaviour of the artificial current along the southern boundary. In MT–BH, this current overshoots its point of entry into the interior and interacts with the eastern boundary. This produces an unrealistic barotropic cell in the southeastern corner of the domain. This cell resembles the recirculation cell found in certain idealized eddy–resolving circulation models (e.g., Cessi et al. (1987)). Apart from the barotropic cell in the SE corner, the flow in the bottom layer is very weak, as in MT.

The greater overall variability in MT–BH is reflected in the EKE field shown in Fig. 40. Although the magnitude of the EKE in MT–BH is higher than in MT, the spatial pattern is similar, except in the southeast corner, near the artificial boundary. Over the Alaskan stream and the Alaska Current region, the EKE levels are larger by a factor of about two. Off Kodiak Island, the maximum EKE level, interpolated to 300 m depth is 120 cm^2 s^{-2}, compared to 55 cm^2 s^{-2} in MT. Observations obtain a value of 80 cm^2 s^{-2}, suggesting that fluctuations in the boundary current in MT–BH may be somewhat too energetic.

7.2 Weak Sponge Layer

The sponge layer is used to provide a sink for the vorticity near the artificial western wall. There is, however, the potential problem that the solution to the east of the layer may be sensitive to the details of the sponge layer friction. To verify whether this is the case, an experiment, MT–SL, was conducted with the sponge layer friction reduced by a factor of four from its previous value in the other experiments, to 0.25×10^{-7} s^{-1}. The configuration of MT–SL is otherwise identical to MT. The top layer EKE field from MT–SL is shown in Fig. 41. Over interior regions and, in fact, almost right up to the edge of the sponge layer, the EKE levels and spatial

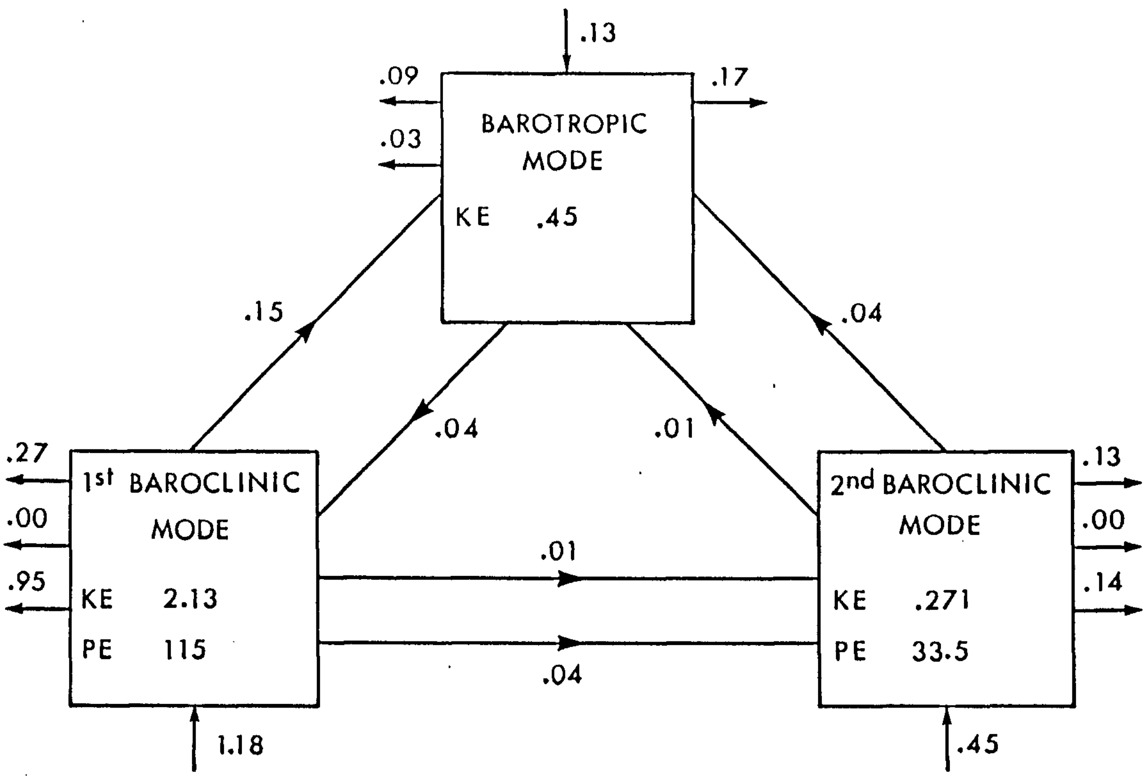

Figure 39. Modal energy budget from experiment MT-BH. The kinetic (KE) and potential (PE) energies of each mode are in 10^3 J m^{-2}. The energy transfer terms are in 10^{-3} J m^{-2} s^{-1}. Refer to Fig. 9 for the meaning of the various energy transfer terms in this figure.

pattern are very similar to MT. This is also true for the EKE fields of the middle and bottom layers (not shown). As might be expected, the regions near the western and southern walls have much higher levels of EKE than in MT. In these regions, eddies are required to dissipate the vorticity of fluid parcels before they reenter the interior. It may be concluded from MT-SL, that, in the regions of interest, the flow is not very sensitive to the strength of the sponge layer.

7.3 Smoothed Topography

In Chapter 5, it was shown that the presence of bottom topography inhibited

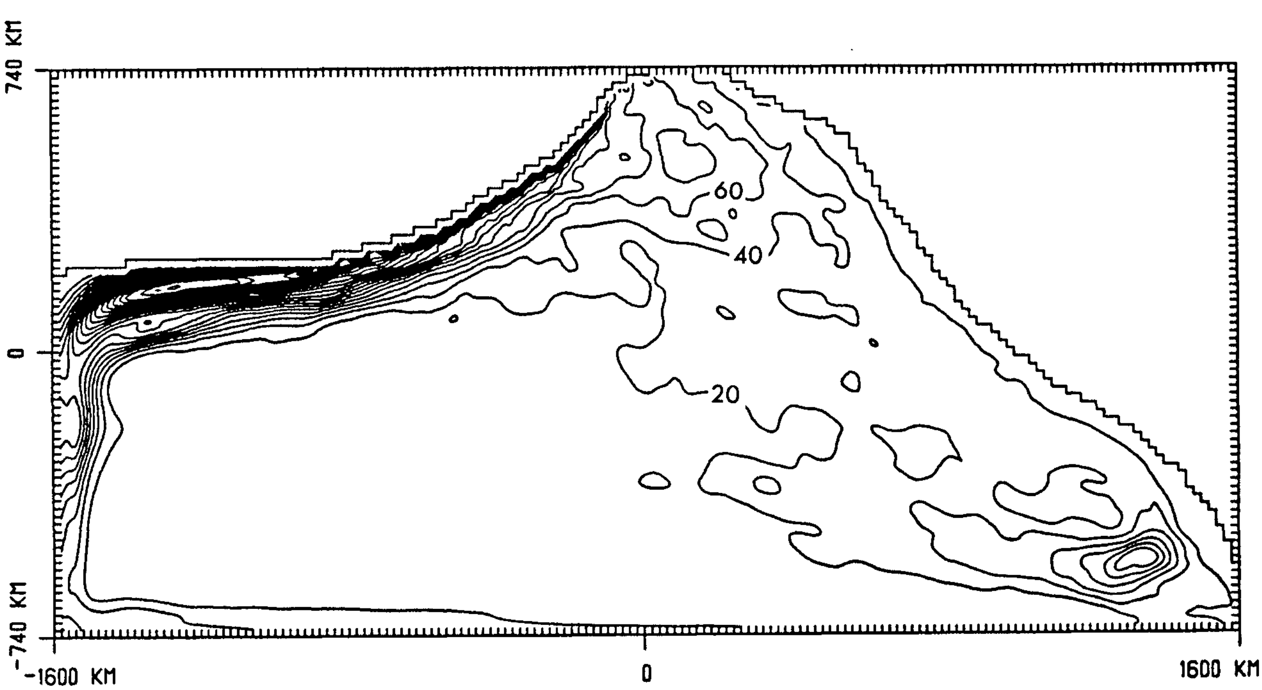

Figure 40. The top layer eddy kinetic energy field from experiment MT-BH. (CI=20 $cm^2\ s^{-2}$.)

the energy cascade to the gravest vertical mode, i.e., the process of barotropization. This was achieved through a reduction of the energy transfer rate due to nonlinear interactions between the barotropic and baroclinic modes. The topography that was found to inhibit this energy transfer has both large scale slopes and small scale roughness. This fact raises an interesting question: is it the small scale roughness or the mean slopes or the two together that effectively inhibit the nonlinear energy transfer? Previous numerical studies of geostrophic turbulence over topography (eg. Treguier and Hua, 1989) have mostly focused on the effects of small scale roughness. In this section, the results of a single experiment, MT-ST, are considered in which only large scale slopes in bathymetry are included. Comparison with experiment MT

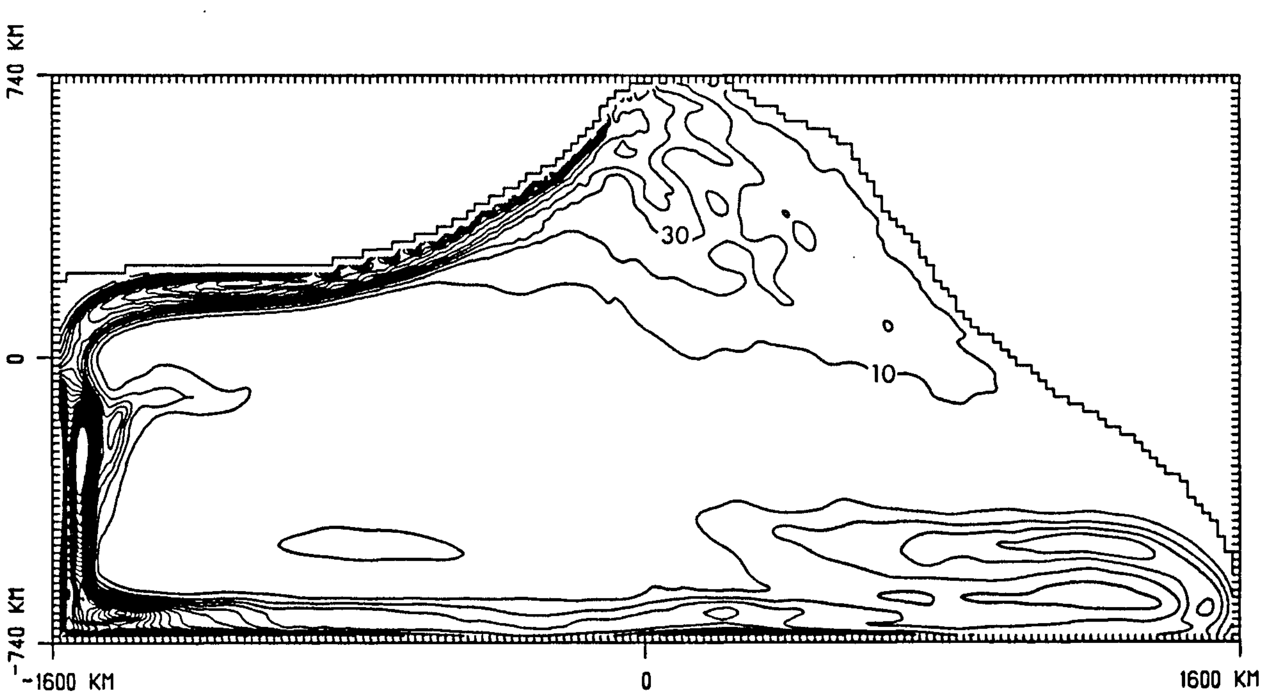

Figure 41. The top layer eddy kinetic energy field from experiment MT-SL (CI=10 cm^2 s^{-2}.)

indicates some of the effects of the small scale topography.

For experiment MT-ST, the topography was smoothed by repeated passes of a digital filter over the bathymetric data (Shapiro, 1970). The resulting field of smoothed topography is shown in Fig. 42. Only the largest scale bathymetric features remain after the smoothing. This includes a shoaling bottom to the northeast and a widened shelf associated with the Aleutian Trench. The presence of seamounts and small scale topography has been almost completely eliminated, with the exception of a highly smoothed version of the large seamount chain, located in the vicinity of 54°N, 150°W off the Aleutian Peninsula.

The new modal energy transfer diagram is shown in Fig. 43. The amount of

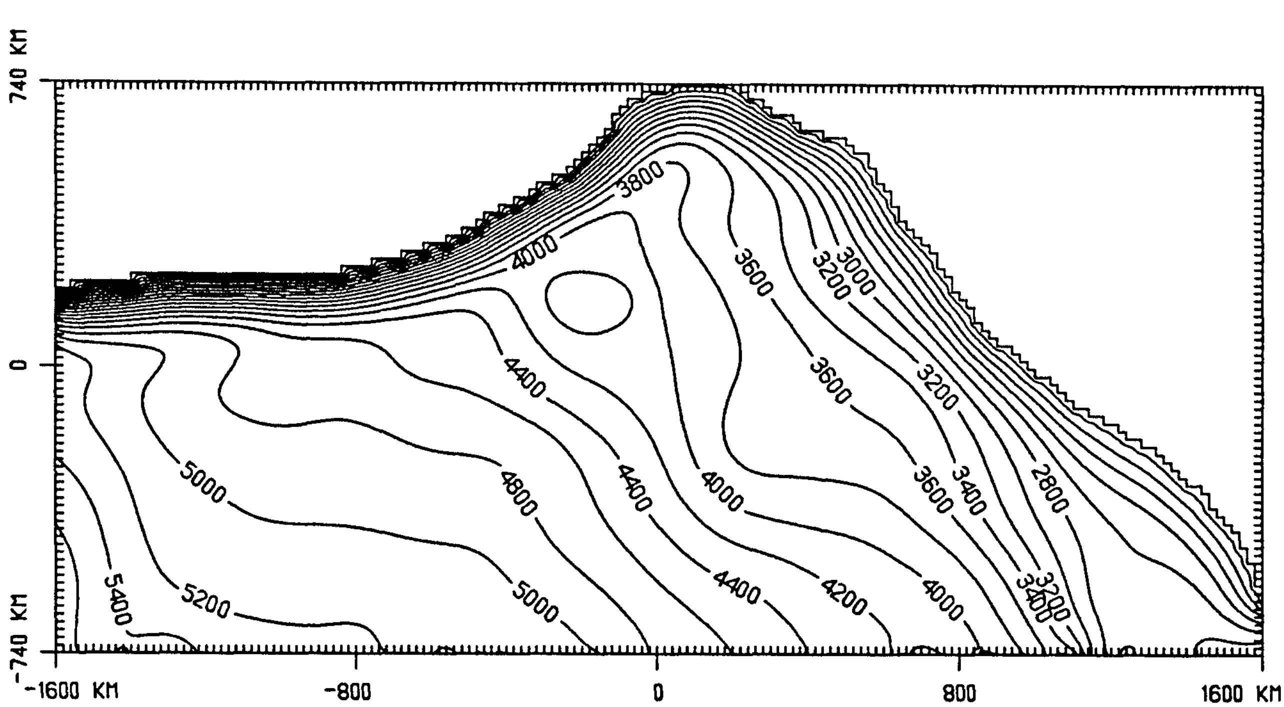

Figure 42. Map of the smoothed bottom topography used in experiment MT–ST. The contour interval is 200 m (different from that of Fig. 8).

barotropic and baroclinic energy is about the same as for MT (Fig. 29a), indicating that the process of barotropization has again been inhibited by the presence of the topography. However, the mechanism through which this is achieved differs in an important way from MT. The nonlinear interaction term between the first baroclinic mode and the barotropic mode has not radically decreased, as in MT, but rather the topographic interaction term between these two modes produces a significant energy transfer in a sense opposite to the main nonlinear transfer.

Instantaneous streamfunction maps for the top and botom layers of MT–ST on Day 724 are shown in Figs. 44a and b. An important feature here is the occurrence of barotropic topographic waves of significant amplitude propagating along the

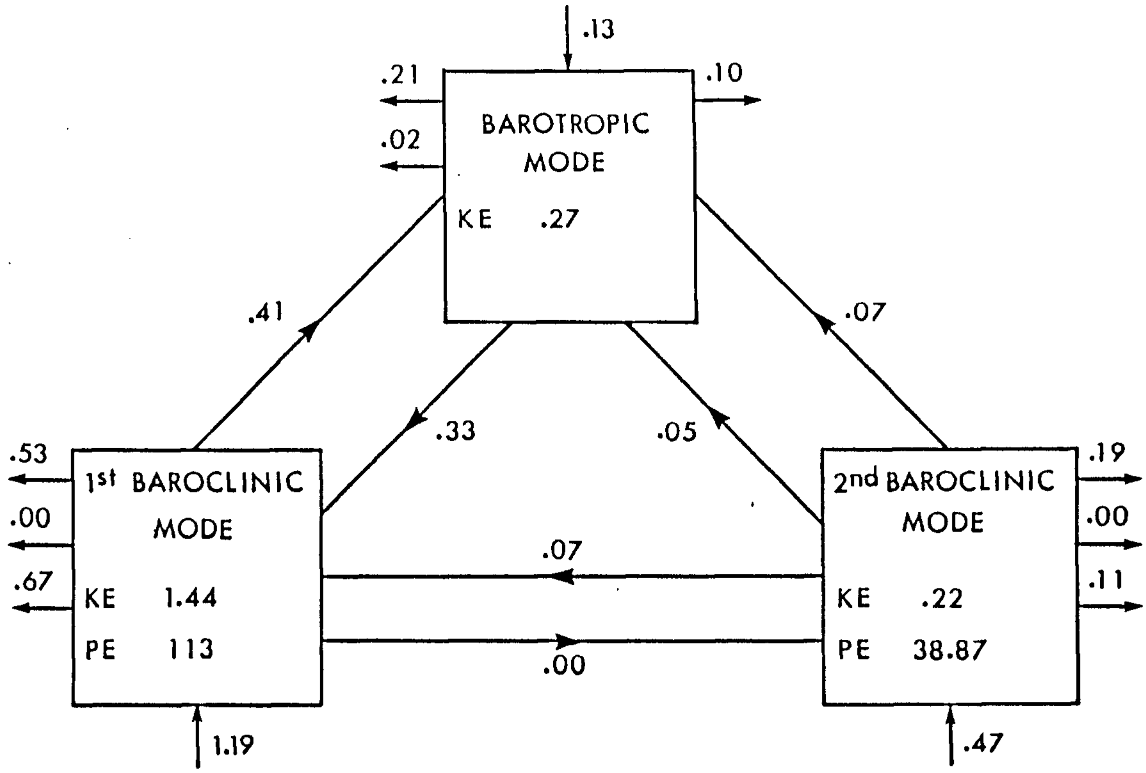

Figure 43. Modal energy budget from experiment MT–ST. The kinetic (KE) and potential (PE) energies of each mode are in 10^3 J m^{-2}. The energy transfer terms are in 10^{-3} J m^{-2} s^{-1}. Refer to Fig. 9 for the meaning of the various energy transfer terms in this figure.

Aleutian Trench. An eof analysis (not shown) indicates that these waves account for a significant fraction (17%) of the variance in the barotropic mode. The increased nonlinear energy transfer from the baroclinic to barotropic mode is, in part, a reflection of the generation of these waves. Evidently the widened shelf of Fig. 42 is not as effective in inhibiting the instability of the overlying flow as the narrow shelf of Fig. 8. This calculation suggests that an accurate representation of the Aleutian Trench in necessary to obtain a correct simulation of the Alaskan Stream.

The magnitude of the nonlinear interaction term between the first two modes has actually increased in MT–ST over the flat–bottom case (MF, Fig. 29b). This

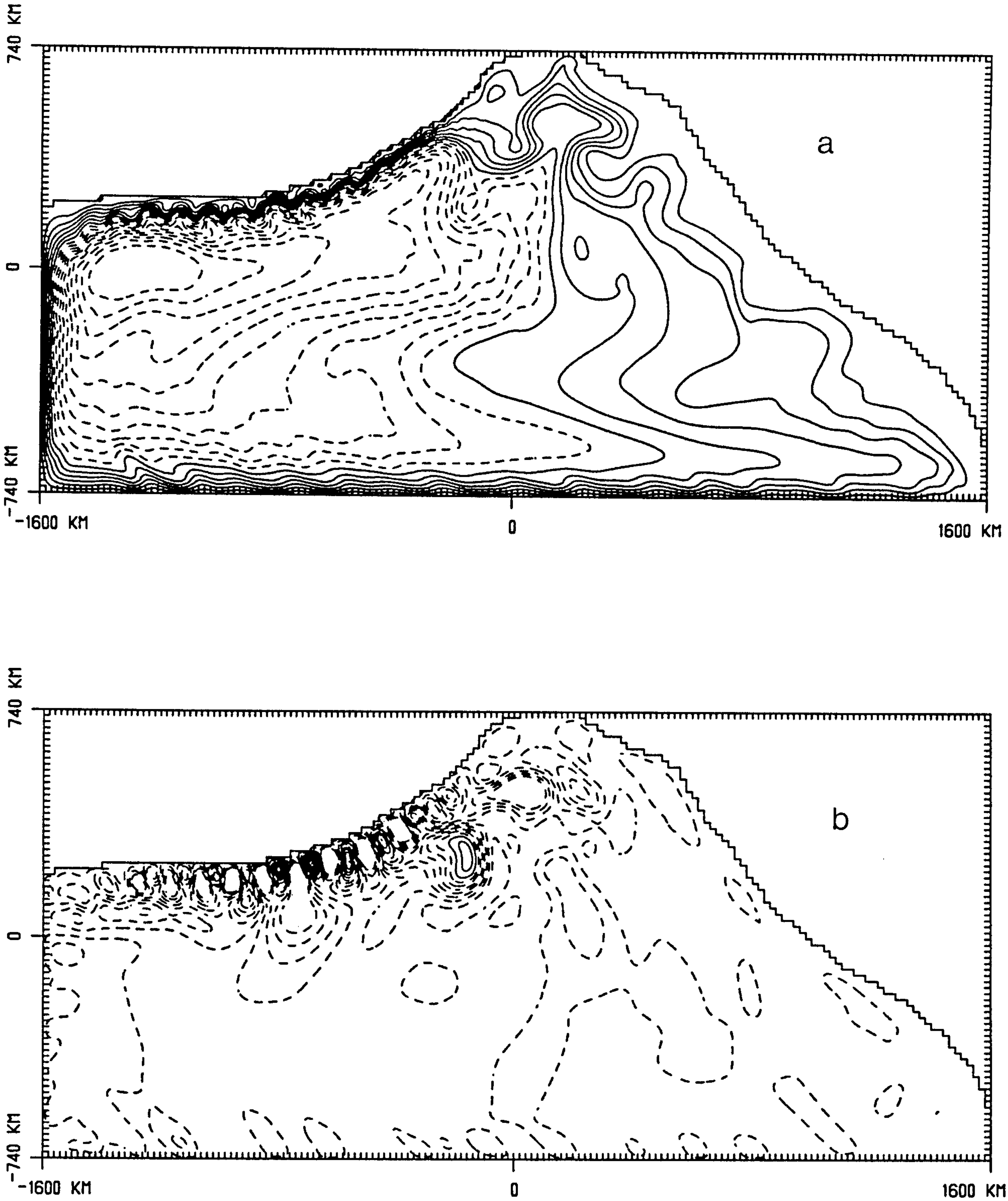

Figure 44. Instantaneous streamfunction fields on Day 724 from experiment MT–ST for (a) the top layer (CI = 3000 $m^2\ s^{-1}$) and (b) the bottom layer (CI = 200 $m^2\ s^{-1}$).

is deceptive, however, since the energy content of the first baroclinic mode is much larger than in MF. If the energy transfer rates in MT–ST and MF are scaled by the respective energy in the first baroclinic mode, then it is clear that there is a reduction in the rate of energy transfer to the barotropic mode in MT–ST. The smoothed topography of MT–ST also inhibits the nonlinear transfer to the gravest mode, although not to the same extent as the rough bottom topography of MT.

The reason for the increased importance of the topographic interaction term in MT–ST is not clear. One possibility is that it is a consequence of an enhancement of a topographically–induced positive correlation between fluctuations of the barotropic and first baroclinic mode, in the bottom layer. Such a correlation is necessary for this term to assume any significance. It may be that the correlation at the bottom is more readily established with only large–scale slopes present. Some evidence for this is found in the coherence and phase diagrams for MT and MT–ST, presented in Fig. 45. The phase shift of 180° found at a period of about 40 days in MT–ST reflects the positive correlation. The vertical structure of the two modes is of opposite sign in the bottom layer, hence a phase shift of 180° in the modal streamfunction fluctuations implies that the two modes are in phase in the bottom layer. This positive correlation, which permits a constructive interference between the two modes, is not obtained in the coherence diagram for MT.

7.4 Summary

The experiments considered in this chapter have disclosed some aspects of the sensitivity of the model. As expected, the replacement of Laplacian with biharmonic friction leads to an increase in the time–averaged kinetic and potential energies, without altering the fundamental nature of the energy exchanges. With the biharmonic operator, the Alaska Current displays considerably more mesoscale structure, while the flow pattern of the Alaskan Stream is not changed. In this respect, the use of biharmonic friction may well move the model towards greater realism in the represen-

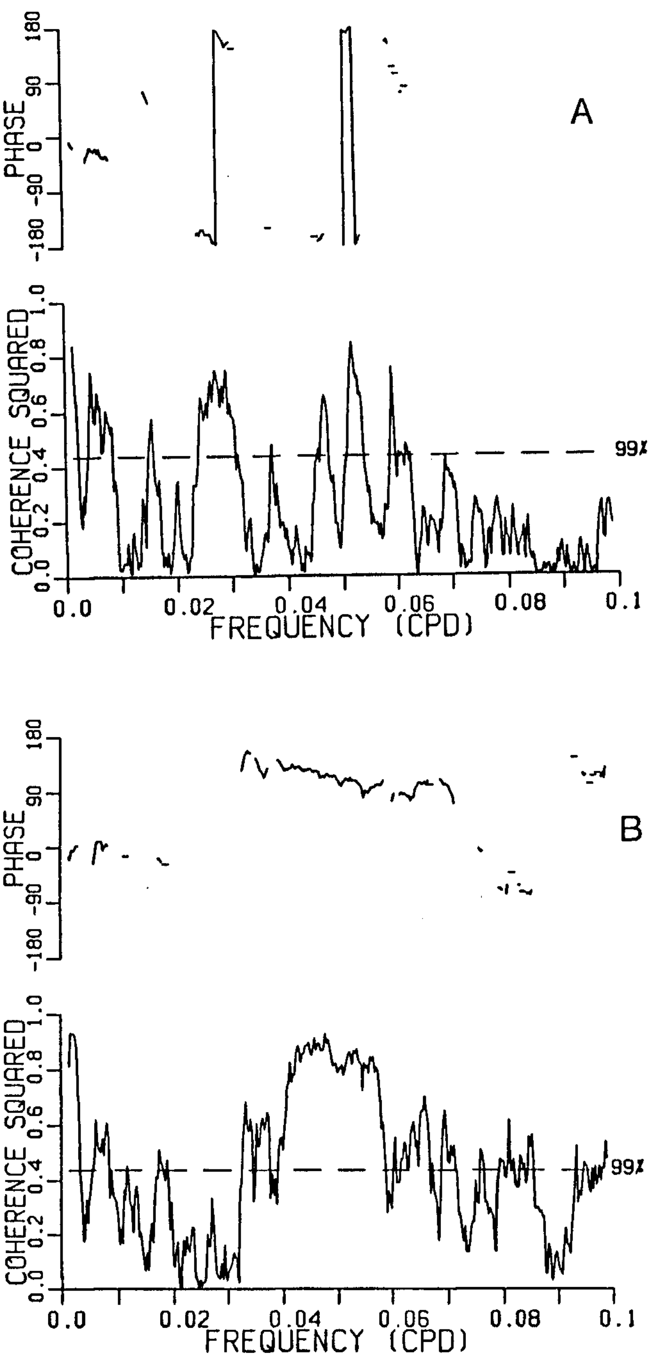

Figure 45. Coherence squared and phase between streamfunction fluctuations in the barotropic and baroclinic modes at a location near the center of the domain (marked by the bold dot on Fig. 26c) for (a) MT–ST and (b) MT. Positive phase implies that the barotropic mode fluctuations are leading. The dashed horizontal line indicates the 99% significance level for coherence.

tation of the gyre. Recent satellite imagery (Gower, 1989) have revealed considerable structure in the sea surface topography on the eastern side of the Gulf of Alaska.

The sensitivity to the sponge layer friction was also investigated. It is reassuring to see that, away from the artificial boundaries, the numerical solution is quite insensitive to the strength of this friction.

A final experiment was conducted to examine sensitivity to small-scale topographic roughness by integrating the model with a highly smoothed topography. Since the realistic topography is rough, this calculation is mainly of geophysical fluid dynamic interest. The calculation shows that the process of barotropization is still arrested by the presence of topography. However, the baroclinicity of the flow is maintained by a different mechanism than with rough bottom topography.

8. Conclusions

The purpose of this work has been to develop an eddy–resolving numerical model of the NE Pacific Ocean in order to study the circulation and dynamics of the region. The comparison of a benchmark calculation with the available observations demonstrated that the model successfully simulates many of the characteristics of the Alaskan Gyre. Mean flow properties and the different forms of transient motion which are specific to this gyre are modelled, at least in a qualitative sense. The intercomparison with observations also points to some of the deficiencies of the model, particularly with respect to the vertical distribution of the mean flow and eddy statistics in the Alaskan Stream and also to the estimation of the barotropic transport.

The role of bottom topography in maintaining the baroclinic structure of the circulation obtained in the benchmark calculation was also investigated. It was shown that the principal effect of topography on the energetics is to reduce the rate of energy transfer to the barotropic mode via nonlinear interactions. It was also shown that the inclusion of bottom topography is necessary for the model to yield a seasonal response that is consistent with observations. This result was used to explain the anomalously large seasonal response of some previous model studies. Some additional sensitivity experiments were also reported.

The model that has been considered above must be regarded as a first step towards a more complete model. While it is useful for the study of the climatological circulation of the NE Pacific, it falls well short of being a model with true predictive capabilities. Furthermore, it was judged inadequate to investigate one of the most interesting phenomena of the region, namely the interannual variability of the Alaskan Gyre. This is due to the use of artificial closed boundaries. The interaction of the gyre with the surrounding ocean is likely to be important for modelling the interannual variability. Thus it is important to avoid the use of closed boundaries.

One possible approach involves using a coarse resolution model of the entire North Pacific to provide inflow/outflow boundary conditions to a fine resolution regional model of the NE Pacific. The latter would be forced by both local winds and by the boundary conditions. Modelling of the interannual variability really amounts to the prediction (hindcasting) of individual events, such as the gyre shift observed in the spring–summer of 1981. Thus it would be essential to use the actual year–by–year winds to force both the fine and coarse resolution models.

In the course of comparing the model response to observations, it became obvious that flow statistics over certain regions of the model could not be verified because the necessary data have never been collected. This is particularly true of the Alaska Current, which is a very poorly observed current system. For example, no direct current measurements have yet been obtained from it. Thus the barotropic component of the flow in this region can only be guessed. Perhaps the most important recommendation for field work is that long term Eulerian current measurements of the Alaska Current be obtained. The model results indicate that, on the eastern side of the basin, there is essentially no mean flow in the abyssal layer and that the Sverdrup flow is confined to the upper layers of the water column. This result does not depend on the inclusion of bottom topography. It will be very interesting to see if this flow distribution is obtained from field data.

References

Anderson, D.L.T. and R.A. Corry, 1985: Ocean response to low frequency forcing with application to the seasonal variation in the Florida Straits – Gulf Stream transport. *Prog. Oceanog.*, **14**, 7–40.

Arakawa, A., 1966: Computational design for long-term numerical integrations of the equations of atmospheric motion. *J. Comput. Phys.*, **1**, 119–143.

Asselin, R.A.,1972: Frequency filter for time integrations. *Mon. Wea. Rev.*, **100**, 487–490.

Barnier, B., 1986: Testing a sponge layer in a two-layer quasi-geostrophic model. Ocean Modelling (unpublished manuscript) No. 71, 9–13.

Bengtsson, L., and C. Temperton, 1979: Difference approximations to quasi-geostrophic models p. 338–378. *Numerical Methods Used In Atmospheric Models Vol. II.* Garp Publication Series No. 17, WMO/ICSU Joint Organizing Committee, 499 pp.

Blandford, R., 1971: Boundary conditions in homogenous ocean models. *Deep-Sea Res.*, **18**, 739–751.

Cessi, P., G. Ierley, and W. Young, 1987: A model of the inertial recirculation driven by potential vorticity anomalies. *J. Phys. Ocean.*, **17**, 1640–1652.

Cox, M.D., 1984: A primitive equation, 3–dimensional model of the ocean. GFDL Ocean Group Tech. Rep. No. 1, GFDL/Princeton University.

Cox, M.D., 1985: An eddy resolving numerical model of the ventilated thermocline. *J. Phys. Oceangr.*, **15**, 1312–1324.

Cummins, P.F., L.A. Mysak, and K. Hamilton, 1986: Generation of annual Rossby waves in the North Pacific by the wind stress curl. *J. Phys. Oceangr.*, **16**, 1179–1189.

Emery, W.J., 1983: On the geographical variability of the upper level mean and eddy fields in the North Atlantic and North Pacific. *J. Phys. Oceangr.*, **13**, 269–291.

Emery, W.J., and K. Hamilton, 1985: Atmospheric forcing of interannual variability in the northeast Pacific Ocean, connections with El-Niño. *J. Geophys. Res.*, **90**, 857–868.

Flierl, G.R., 1978: Models of vertical structure and the calibration of two-layer models. *Dyn. Atmos. Oceans*, **2**, 341–381.

Fu, L., 1983: On the wave number spectrum of oceanic mesoscale variability observed by the SEASAT altimeter. *J. Geophys. Res.*, **88**, 4331–4341.

Glaser, J.I., 1970: Numerical solution of waveguide scattering problems by finite difference Green's functions. *IEEE Trans. on Microwave Theory and Techniques*, **MTT-18**, 436–443.

Gower, J.F.R., 1989: Geosat altimeter observations of the distribution and movement of sea–surface height anomalies in the north–east Pacific. Proceedings of the Oceans'89 conference, Seattle, Washington, September 18–21, 1989

Hamilton, K., 1985: A study of the variability of the return migration route of Fraser River sockeye salmon *(Oncorhynchus nerka)*. Can. J. Zool., **63**, 1930–1943.

Hamilton, K., and L.A. Mysak, 1986: Possible effects of the Sitka eddy on sockeye *(Oncorhynchus nerka)* and pink *(Oncorhynchus gorbuscha)* migration off southeast Alaska. *Can. J. Fish. Aquat. Sci.*, **43**, 498–504.

Harrison, D.E., 1989: On climatological monthly mean wind stress and wind stress curl fields over the world ocean. *J. Climate*, **2**, 57–70.

Harrison, D.E. and W.R. Holland, 1981: Regional eddy vorticity transport and the equilibrium vorticity budgets of a numerical model ocean circulation. *J. Phys. Oceangr.*, **11**, 190–208.

Hellerman, S. and M. Rosenstein, 1983: Normal monthly wind stress over the world ocean with error estimates. *J. Phys. Oceangr.*, **13**, 1093–1104.

Hockney, R.W., 1970: The potential calculation and some applications. *Methods in Computational Physics*, **9**, 135-211.

Holland, W.R., 1978: The role of mesoscale eddies in the general circulation of the ocean - numerical experiments using a wind-driven quasi-geostrophic model. *J. Phys. Oceangr.*, **8**, 363–392.

Holland, W.R., 1986: Quasi-geostrophic modelling of eddy-resolving ocean circulation. *Advanced Physical Oceanographic Numerical Modelling*, J.J. O'Brien Ed., D. Reidel Publishing Company, 203–231.

Holland, W.R., 1987: A numerical model study of the wind-driven response of the Eastern North Pacific to realistic wind forcing. In proceedings of the 19th general assembly of IUGG, Vancouver, Canada, August 9-22. Abstracts Vol. 3, p. 1005.

Holland, W.R., and P.B. Rhines, 1980: An example of eddy induced ocean circulation. *J. Phys. Oceangr.*, **10**, 1010–1031.

Hsieh, W.W., 1987: A numerical study of the seasonal cycle and its perturbations in the northeast Pacific Ocean. *Atmos. Ocean*, **25**, 375–386.

Huang, J.C.K., 1978: Numerical simulation studies of oceanic anomalies in the North Pacific Basin: the ocean model and the long-term mean state. *J. Phys. Oceangr.*, **8**, 755–778.

Huang, J.C.K., 1979: Numerical simulation studies of oceanic anomalies in the North Pacific Basin: II. Seasonally varying motions and structures. *J. Phys. Oceangr.*, **9**, 37–56.

Hurlburt, H.E. and J. Dana Thompson, 1984: Preliminary results from a numerical study of the New England Seamount Chain influence on the Gulf Stream. *Predictability of Fluid Motions (La Jolla Institute - 1983)*,G. Holloway and B. West Eds., American Institute of Physics, New York, 489–503.

Large, W.G. and S. Pond, 1981: Open ocean momentum flux measurements in moderate to strong winds. *J. Phys. Ocean.*, **11**, 324–336.

McWilliams, J.C., 1977: A note on a consistent quasigeostrophic model in a multiply-connected domain. *Dyn. Atmos. Oceans*, **1**, 427–441.

McWilliams, J.C., W.R. Holland and J.H.S. Chow, 1978: A description of numerical Antarctic Circumpolar Currents. *Dyn. Atmos. Oceans*, **2**, 213–291.

Mysak, L.A., 1982: Barotropic instability of flow along a trench. *Geophys. Astrophys. Fluid Dynam.*, **19**, 1–33.

Mysak, L.A., 1985: On the interannual variability of eddies in the northeast Pacific Ocean. *El-Niño north: Niño effects in the eastern subarctic Pacific Ocean*, W.S. Wooster Ed., University of Washington, Sea Grant publication, 97–106.

Mysak, L.A., 1986: El-Niño, interannual variability and fisheries in the northeast Pacific Ocean. *Can. J. Fish. Aquat. Sci.*, **43**, 464–497.

Pedlosky, J., 1979: *Geophysical Fluid Dynamics*. Springer-Verlag, New York, 624 pp.

Preisendorfer, R.W. and C.D. Mobley, 1988: *Principal Component Analysis in Meteorology and Oceanography*. Elsevier, 426pp.

Reed, R.K., 1984: Flow of the Alaskan Stream and its variations. *Deep-Sea Res.*, **31**, 369–386.

Reed, R.K., and J.D. Schumacher, 1984: Additional current measurements in the Alaskan Stream near Kodiak Island. *J. Phys. Oceangr.*, **14**, 1239–1246.

Reed, R.K., R.D. Muench and J.D. Schumacher, 1980: On the baroclinic transport of the Alaskan Stream near Kodiak Island. *Deep-Sea Res.*, **27**, 509–523.

Reed, R.K., J.D. Schumacher and J.P. Blaha, 1981: Eulerian measurements in the Alaskan Stream near Kodiak Island. *J. Phys. Oceangr.*, **11**, 1591–1595.

Rhines, P.B., 1977: The dynamics of unsteady currents. The Sea, Vol. 6, Wiley Interscience, 189–318.

Rienecker, M.M. and L.L. Ehret, 1988: Wind stress curl variability over the North Pacific from the Comprehensive Ocean–Atmosphere Data Set. *J. Geophys. Res.*, **93**, 5069–5077.

Roache, P.J., 1973: *Computational Fluid Dynamics*. Hermosa Publishers, Albuquerque, N.M., 446 pp.

Royer, T.C., 1981: Baroclinic transport in the Gulf of Alaska. Part I. Seasonal variations of the Alaska Current. *J. Mar. Res.*, **39**, 239–250.

Royer, T.C., and W.J. Emery, 1987: Circulation in the Gulf of Alaska, 1981. *Deep-Sea Res.*, **34**, 1361–1377.

Schmitz, W.J., and W.R. Holland, 1982: A preliminary comparison of selected numerical eddy-resolving general circulation experiments with observations. *J. Mar. Res.*, **40**, 75–117.

Schmitz, W.J. and W.R. Holland, 1986: Observed and modelled mesoscale variability near the Gulf Stream and Kuroshio extension. *J. Geophys. Res.*, **91**, 9624–9638.

Schumacher, J.D. and R.K. Reed, 1983: Interannual variability in the abiotic environment of the Bering Sea and the Gulf of Alaska. *From year to year - interannual variability of the environment and fisheries of the Gulf of Alaska and eastern Bering Sea*, W.S. Wooster, Ed., University of Washington, Sea Grant publication, 111–133.

Shapiro, R., 1970: Smoothing, filtering, and boundary effects. *Rev. Geophys. and Space Phys.*, **8**, 359–387.

Snyder, J.P., 1982: *Map projections used by the U.S. Geological Survey*, 2nd ed. Geological Survey Bulletin, No. 1532.

Stewart, R.W., 1989: The no–slip constraint and ocean models. *Atmos. Ocean*, **27**, (in press).

Swartztrauber, P.N., 1984: Fast Poisson solvers. *Studies in Numerical analysis*, G.N. Golub Ed., MAA Studies in Mathematics, **24**. The Mathematical Association of America, 319–370.

Swaters, G.E. and L.A. Mysak, 1985: Topographically induced baroclinic eddies near a coastline, with application to the northeast Pacific. *J. Phys. Oceangr.*, **15**, 1470–1485.

Tabata, S. 1976: Evidence of a westward–flowing 'Subarctic Countercurrent' in the North Pacific Ocean. *J. Fish. Res. Board Can.*, **33**, 2168–2196.

Tabata, S., 1982: The anticyclonic, baroclinic eddy off Sitka, Alaska, in the northeast Pacific. *J. Phys. Oceangr.*, **12**, 1260–1282.

Tabata, S., 1983: Commentary: interannual variability in the abiotic environment of the Bering Sea and the Gulf of Alaska. *From Year to Year – interannual variability of the environment and fisheries of the Gulf of Alaska and eastern Bering Sea*, W.S. Wooster Ed., University of Washington, Sea Grant publication, 139–145.

Tabata, S., 1989: Annual and interannual variability of baroclinic transports across Line P in the northeast Pacific Ocean. *Deep-Sea Res.*, (submitted).

Talley, L.D., 1988: Potential vorticity distribution in the North Pacific. *J. Phys. Oceangr.*, **18**. 89–106.

Thom, A., 1928: An investigation of fluid flow in two dimensions. Aerospace Research Center, R. and M., No. 1194, United Kingdom.

Thomson, K.A., 1986: On the geographical variability of oceanic mesoscale motions. Ph.D. Thesis, University of British Columbia, Vancouver, B.C.

Thomson, R.E., 1972: On the Alaskan Stream. *J. Phys. Oceangr.*, **2**, 363–371.

Treguier and Hua, 1989: Influence of bottom topography on stratified quasi-geostrophic turbulence in the ocean. *Geophys. Astrophys. Fluid Dynamics*, **43**, 265–305.

Veronis, G. and H. Stommel, 1956: The action of variable wind stresses on a stratified ocean. *J. Mar. Res.*, **15**, 43–75.

Warren, B.A., 1983: Why is no deep water formed in the North Pacific *J. Mar. Res.*, **41**, 327–347.

Warren, B.A., W.B. Owens, 1985: Some preliminary results concerning deep northern-boundary currents in the North Pacific. *Prog. Oceanogr.*, **14**, 537–551.

Warren, B.A., W.B. Owens, 1988: Deep currents in the central subarctic Pacific Ocean. *J. Phys. Oceanogr.*, **18**, 529–551.

White,W.B. and J.F.T. Saur, 1981: A source of annual baroclinic waves in the eastern subtropical North Pacific. *J. Phys. Oceangr.*, **11**, 1452–1462.

Willmott, A.J. and L.A. Mysak, 1980: Atmospherically forced eddies in the northeast Pacific. *J. Phys. Oceangr.*, **10**, 1769–1791.

Wooster, W.S. [ed.], 1983: *From year to year - interannual variability of the environment and fisheries of the Gulf of Alaska and eastern Bering Sea.* University of Washington, Sea Grant publication, 208 pp.

Wyrtki, K., L. Magaard, and J. Hager, 1976: Eddy energy in the oceans. *J. Geophys. Res.*, **81**, 2641–2646.

Appendix A

Capacitance Matrix Algorithm

The solution to a finite difference Helmholtz or Poisson equation can be obtained through iterative methods such as relaxation, or through direct methods such as the FACR(l) algorithm (Schwartztrauber, 1984). The direct methods are usually preferred since they are much more efficient than the iterative methods and do not require the specification of a convergence criterion. However, they are not as generally applicable as iterative methods; in particular, they are most frequently constructed to solve the Helmholtz equation in rectangular domains. The capacitance matrix method (Hockney 1970) is a technique for extending the usefulness of direct solvers to nonrectangular domains. The major computational burden of the method is the requirement that the direct solver must be called twice in a program to obtain the solution. In addition, a large capacitance matrix must be stored. Nevertheless, this is usually much more efficient than resorting to an iterative solver. A simple algorithm is presented here for the application of the technique to the Helmholtz equation with Dirichlet boundary conditions. The formulation of the method in a continuous domain is first presented, followed by a brief discussion of its implementation in the finite difference context.

We wish to obtain a field, $\phi(x,y)$, which satisfies

$$(\nabla^2 - \lambda^2)\phi = \theta(x,y) \tag{A.1}$$

where θ is a given forcing function, in a domain Ω with the boundary condition $\phi = \phi_B$ on $\partial\Omega$, the contour bounding Ω (Fig. 19). x and y are the usual Cartesian coordinates, defined over Ω. Although ϕ_B is constant along $\partial\Omega$ for a closed domain QG model, this condition is not in general required to apply the technique given below.

Let Ω be embedded in a rectangular domain Ω_1 with boundary $\partial\Omega_1$. Some portion of the contours $\partial\Omega$ and $\partial\Omega_1$ may coincide, as in Fig. 19, but this is not necessary. The portion of the $\partial\Omega$ contour which does not coincide with $\partial\Omega_1$ is denoted by $\partial\Omega'$; the area between $\partial\Omega$ and $\partial\Omega_1$ is denoted by Ω'. Also let $\tilde{s}$ be a coordinate along the contour $\partial\Omega'$.

We obtain first a field, ϕ_1, which satisfies

$$(\nabla^2 - \lambda^2)\phi_1 = \theta_1 \tag{A.2}$$

in the regular domain Ω_1. The boundary condition is $\phi_1 = \phi_B$ on $\partial\Omega_1$. The forcing $\theta_1 = \theta$ in Ω, but is arbitrary in Ω' and on $\partial\Omega'$, and may be taken as zero there. Formally, we may write the solution to (A.2) as

$$\phi_1 = \int\int_{\Omega_1} G(x,y\,;\,x_\circ,y_\circ)\,\theta_1\,(x_\circ,y_\circ)dx_\circ\,dy_\circ + \int_{\partial\Omega_1} \phi_1\,\nabla G\cdot\mathbf{n}\;dl_\circ, \tag{A.3}$$

where $\mathbf{n}$ is a unit vector, normal to $\partial\Omega_1$, and $l_\circ$ is a coordinate along this curve. The Green's function, G, satisfies

$$(\nabla^2 - \lambda^2)\;G = \delta(x - x_\circ)\,\delta(y - y_\circ) \tag{A.4}$$

in the domain Ω_1 with δ the Dirac delta function and $G = 0$ on $\partial\Omega_1$.

The function ϕ_1 will not in general have $\phi_1 = \phi_B$ on $\partial\Omega'$. The essence of the capacitance matrix method is to modify θ_1, the right hand side of (A.2), on $\partial\Omega'$ so that the solution to the Helmholtz operator in Ω_1 has the value ϕ_B on $\partial\Omega'$ and hence is our desired solution in Ω. To make this more explicit, let the function modifying θ_1 be denoted by $\Theta(\tilde{s})$ where Θ is nonzero only on $\partial\Omega'$. Now consider a function $\mu(x,y)$ which satisfies

$$(\nabla^2 - \lambda^2)\mu = \theta_1 + \Theta \tag{A.5}$$

in Ω_1, with $\mu = \phi_B$ on $\partial\Omega_1$. If $\Theta(\tilde{s})$ is chosen such that the solution to (A.5) has $\mu = \phi_B$ on $\partial\Omega'$, then $\phi(x,y) = \mu(x,y)$ in the domain Ω, and the solution to (A.1) is found.

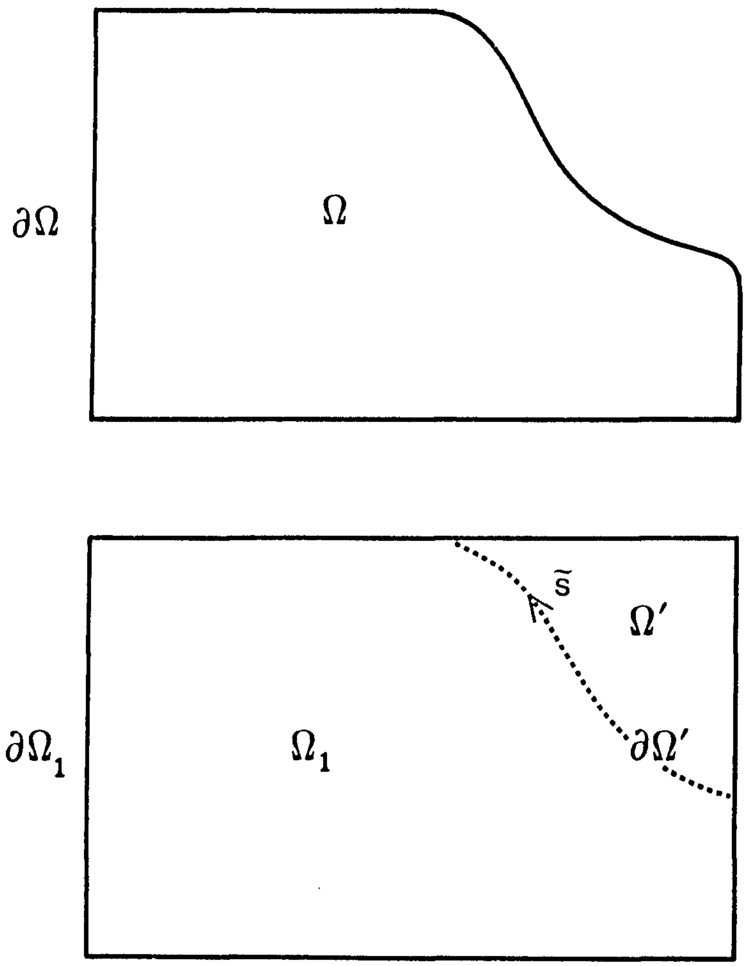

Figure 46. Domain geometry for the capacitance matrix method. The domain Ω is embedded in the rectangular domain Ω_1. The curve $\partial\Omega'$ is the 'irregular' part of $\partial\Omega$, which is the boundary of Ω. The coordinate along $\partial\Omega'$ is $\tilde{s}$.

To determine $\Theta(\tilde{s})$ we use (A.3) and (A.4) to write the solution to (A.5) as

$$\mu(x,y) = \phi_1 + \int_{\partial\Omega'} \Theta(\tilde{s}_o)\, G(x,y;\, \tilde{s}_o)\, d\tilde{s}_o. \tag{A.6}$$

We now require that $\mu = \phi_B$ on $\partial\Omega'$ so that (A.6) reduces to

$$\phi_B = \phi_1(\tilde{s}) + \int_{\partial\Omega'} \Theta(\tilde{s}_o)\, G(x,y;\, \tilde{s}_o)\, d\tilde{s}_o, \tag{A.7}$$

which is an integral equation that determines Θ.

It is straightforward to apply this technique to a finite difference form of (A.1) on a uniform mesh. The curve $\partial\Omega'$ passes through a set of grid points referred to as the irregular boundary points. The numerical algorithm first requires that a direct solver be applied to obtain the ϕ_1 field of (A.2), in the rectangle, given the forcing field θ_1. Next the modifying function Θ is obtained from the values of ϕ_1 along $\partial\Omega'$ by using a discretized version of (A.7). The direct solver is employed a second time to solve (A.5) and the required solution is obtained.

For a finite difference mesh, (A.7) can be written in matrix form as

$$\phi_B = \phi_1 + \Delta s^2 \ \mathbf{G} \cdot \Theta, \tag{A.8}$$

where Δs is the grid interval, and Θ, ϕ_1 and ϕ_B are now column vectors of length M, where M is the number of irregular boundary points. The vector Θ contains the correction to the forcing at the irregular boundary points, the vector ϕ_1 contains the value of the ϕ_1 field at these points, and the vector ϕ_B, the boundary values, also at the same points.

The finite difference Green's function, $\mathbf{G}$, is an $M \times M$ matrix. It is determined in the following manner. A delta function source of strength Δs^{-2} is placed at one irregular grid point and the solution to (A.4) is obtained in the rectangle to yield the response at all the irregular boundary points. The determined response forms one row of $\mathbf{G}$; successive rows are obtained in the same way by moving the location of the unit source along the irregular boundary, until the matrix is filled. Glaser (1970) showed numerically that the finite difference Green's function for the Helmholtz equation is a convergent approximation as $\Delta s \to 0$.

By rearranging (A.8), the vector Θ is found from

$$\Theta = \Delta s^{-2} \mathbf{C} \ (\phi_B - \phi_1) \tag{A.9}$$

where $\mathbf{C} = \mathbf{G}^{-1}$ is the capacitance matrix. Provided that the geometry and the Helmholtz constant, λ, do not change, the capacitance matrix has to be determined only once, at the outset of the integration. For a QG model with N layers, it is necessary to construct and store N such matrices, one for each mode.

Appendix B

Effects of Horizontal Resolution

As stated in Chapter 4, the layer depths and density differences were chosen to yield Rossby radii of 17.2 and 9.6 km, for the first and second internal modes, which compares well with the observed values. Since the horizontal scale of motions in the baroclinic modes is of the order of the Rossby radii, the problem of horizontal resolution inevitably arises. Specifically, given the parameters chosen for this study, is a resolution of 20 km sufficient? Due to limited computational resources, it was not possible to test directly whether the 20 km resolution was adequate by running, say, a 10 km model and then comparing with a 20 km case. The problem was, nevertheless, examined in the context of a box model. While this approach does not rigorously prove that 20 km is sufficient, it does give some indication of the adequacy of this resolution.

Two integrations were conducted in a square (1000 km $\times$ 1000 km) domain, QGBOX1 and QGBOX2 with a horizontal resolution of 20 km and 10 km, respectively. In both cases, the choice of parameters, i.e. layer depths and density differences, is identical to the ones used in the experiments discussed above (Table I). The horizontal Laplacian friction coefficient is held constant at 200 $m^2\ s^{-1}$, a point that is discussed at greater length below. The forcing is a steady, zonally–constant wind stress curl designed to drive a single, anticyclonic gyre.

The two models were integrated to stationarity and their statistical properties compared to test whether the finer resolution in QGBOX2 leads to any significant differences. The mean top layer streamfunction and eddy kinetic energy fields of the two experiments are shown in Figs. 47 and 48. The comparison between the two cases shows that the overall pattern and amplitude of the statistical fields are very similar. The global modal energy budgets, given in Fig. 49, reinforce this impression. The most notable difference of doubling the resolution is a 15% reduction in the rate

A

B

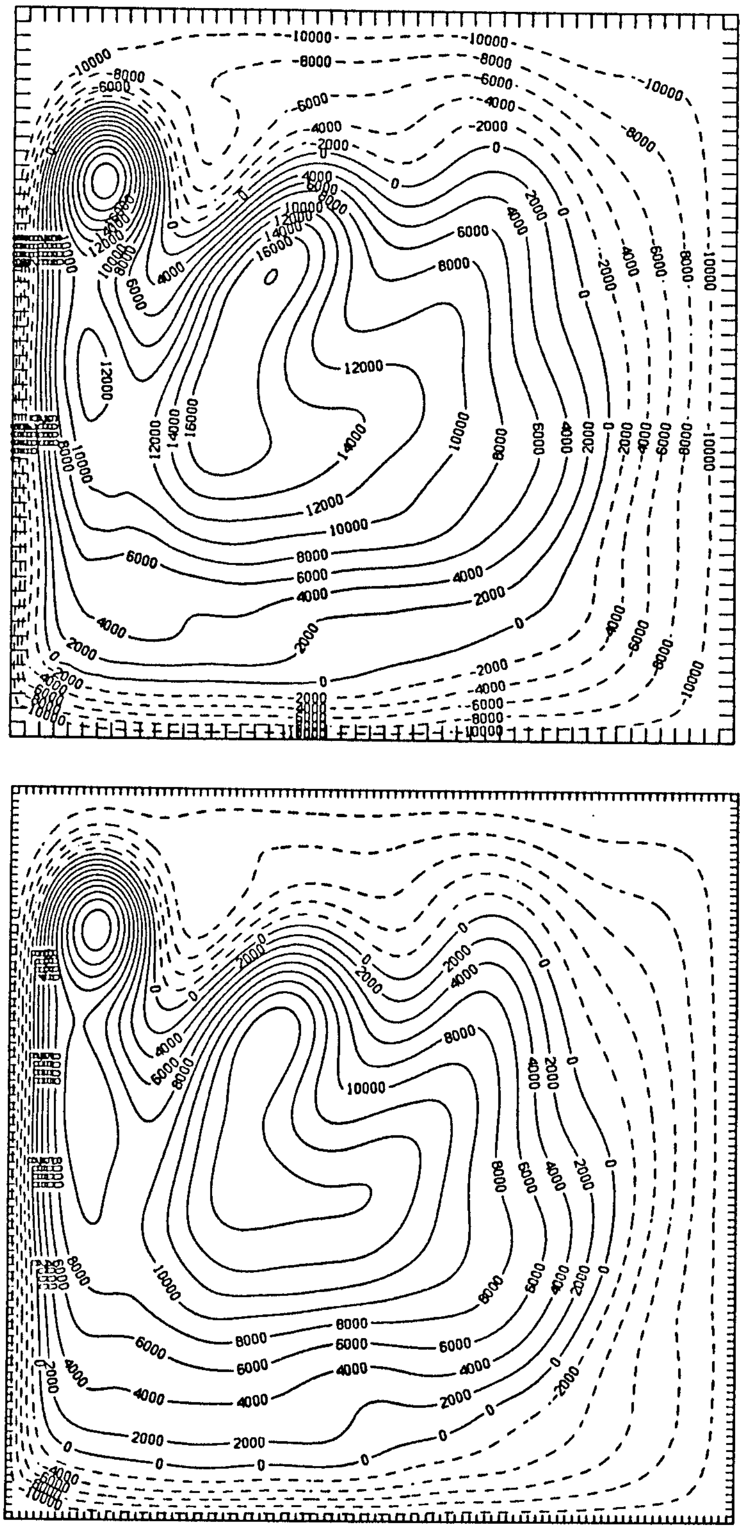

Figure 47. The mean top layer streamfunction fields for (a) QGBOX1 and (b) QGBOX2. (CI=2000 m^2 s^{-1}).

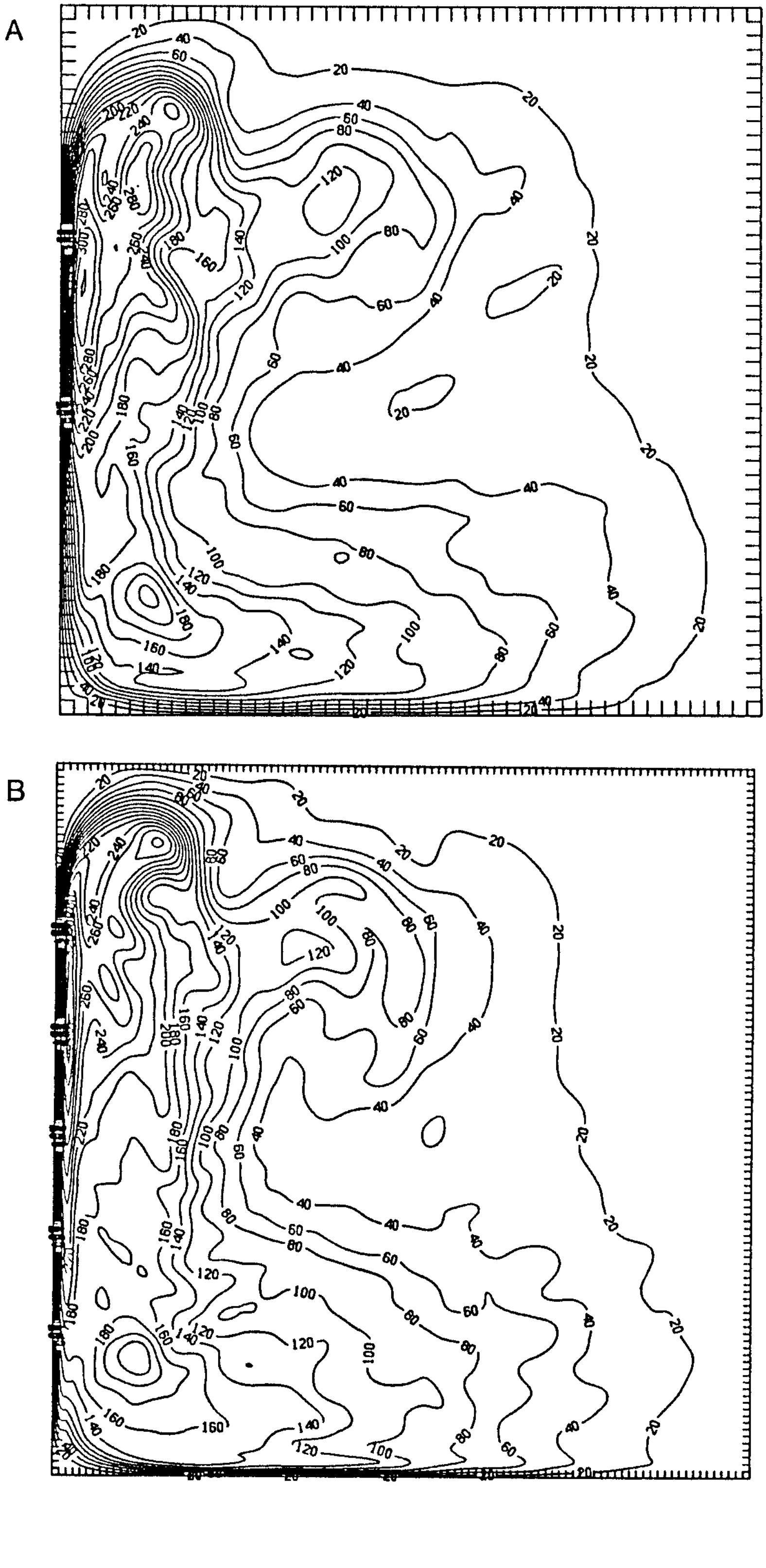

Figure 48. The top layer eddy kinetic energy fields for (a) QGBOX1 and (b) QGBOX2. (CI=20 $cm^2\ s^{-2}$).

of nonlinear energy transfer to the barotropic mode and a corresponding reduction in the kinetic energy of this mode. The energy in the baroclinic modes is virtually unaffected.

The rate of energy transfer to the barotropic mode should be the most sensitive to the change in resolution because of the nature of the process of barotropization. Rhines (1977) showed that, for motions with a scale smaller than the first internal deformation radius, adjacent layers will not be strongly coupled. Once the motion reaches this scale, the vortex stretching is comparable to the relative vorticity and the motion becomes coupled in the vertical, with an ensuing transfer of energy to the barotropic mode. Since the coupling of motion in the vertical is defined by a scale that is close to the resolution of the model, it is not surprising to see that this process is slightly affected by a change in resolution.

The comparison presented here shows that increasing the resolution leads mainly to a small quantitative difference in the rate of barotropization, without any qualitative changes in the nature of the solution. By increasing the horizontal resolution it is possible to allow a smaller coefficient of horizontal friction; the only limitation being that the Munk boundary layer has to be resolved. It may be expected that there will be significant increase in the variability of the flow field (as measured, for example, by the EKE field) associated with a reduction in the horizontal viscosity. It is also conceivable that, in the limit of very high horizontal resolution and vanishing friction, new structures will begin to emerge in the flow field which are not permitted with the present choice of parameters. However, the comparison of box model experiments suggests that, within the range of parameters considered in this study, a horizontal resolution of 20 km is adequate.

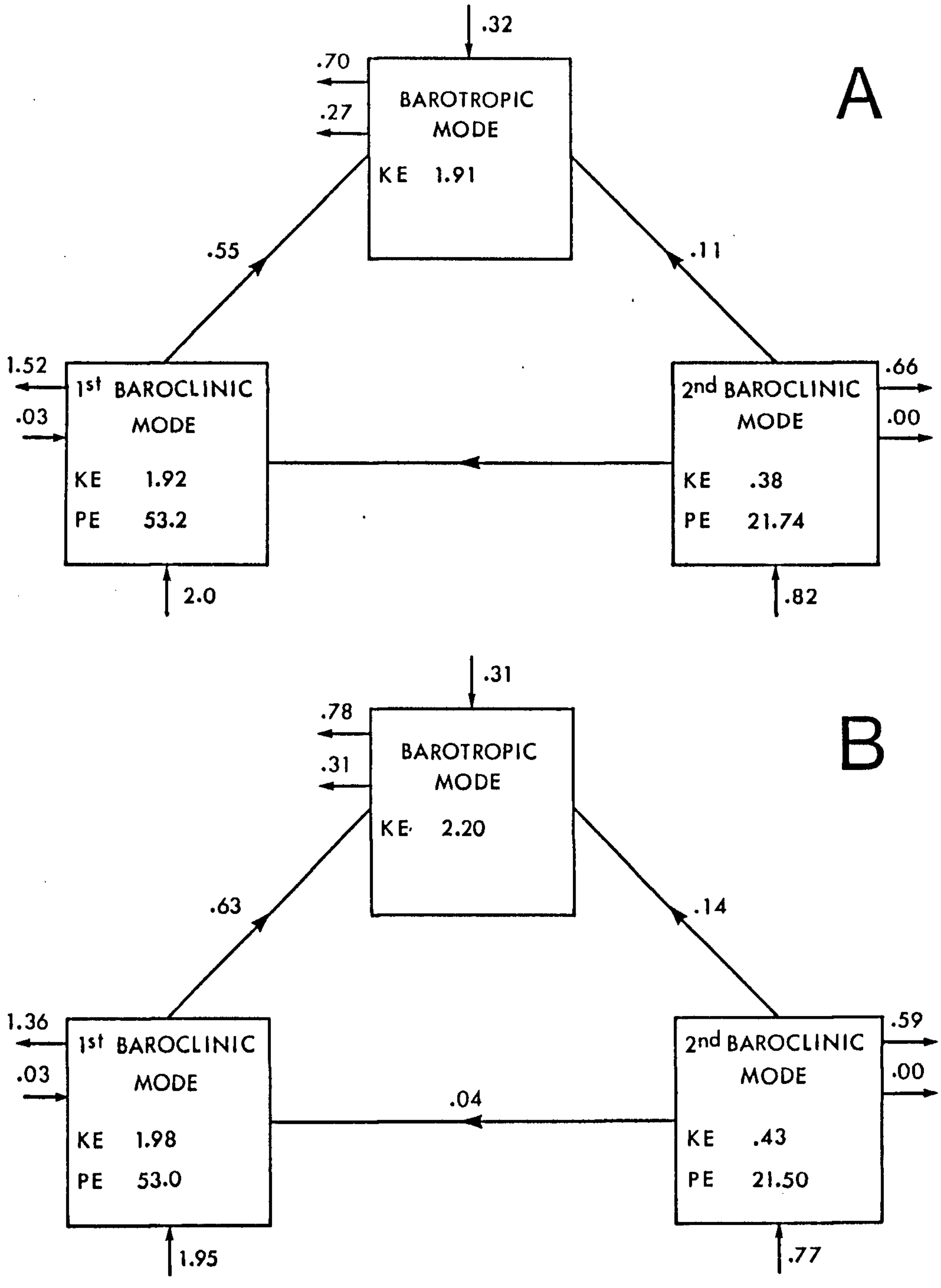

Figure 49. Modal energy budgets for (a) QGBOX1 and (b) QGBOX2. The kinetic (KE) and potential (PE) energies of each mode are in 1×10^3 J m^{-2}. The energy transfer terms are in 1×10^{-3} J m^{-2} s^{-1}. Refer to Fig. 9 for the meaning of the various transfer terms in this figure.